Doctoral Dissertation

On the Origin and Evolution of the Angular Momentum of Star Forming Cores in Filamentary Molecular Clouds

フィラメント状分子雲における分子雲コアの角運動量についての理論的研究

Yoshiaki Misugi

Graduate School of Science,
Nagoya University

Supervisor: Shu-ichiro Inutsuka

May 25, 2022

Abstract

The angular momentum of a molecular cloud core plays a key role in star formation, since it is directly related to the outflow and the jet emanating from the new-born star and it eventually results in the formation of the protoplanetary disk. However, the origin of the core rotation and its time evolution are not well understood. Recent observations reveal that molecular clouds exhibit a ubiquity of filamentary structures and that star forming cores are associated with the densest filaments. Since these results suggest that dense cores form primarily in filaments, the mechanism of core formation from filament fragmentation should explain the distribution of the angular momentum of these cores. In this thesis, I investigate the origin and evolution of the angular momentum of molecular cloud cores formed through filament fragmentation process.

First, I semi-analytically derive the relation between the turbulent velocity field and resultant core angular momentum in filamentary molecular clouds. I show that the sub sonic (or transonic) Kolmogorov turbulent velocity field model can reproduce the observed property of the angular momentum of cores. I conclude that the origin of the angular momentum of cores is sub sonic (or transonic) Kolmogorov turbulent velocity field. Recent theoretical research shows that the filamentary structures are formed when the molecular cloud is swept by the shock wave. I also analyse the results of filament formation simulations and show that the the line mass and velocity power spectrum along the filaments follow Kolmogorov turbulence. Therefore, I conclude that filament formation scenario can explain the origin of the angular momentum of cores.

Finally, I perform the three-dimensional simulations to investigate the time evolution of angular momentum of molecular cloud core formed through filament fragmentation process. As a result, I find that the angular momenta of cores change only by 30% in their formation process. I also find that most of the cores rotate perpendicular to the filament axis. In addition, I analyze the internal angular momentum structure of cores. Although the cores gain various angular momentum from the initial turbulent velocity fluctuations in the filament, the angular momentum profile in a core converges to the self-similar solution. I also show that the degree of complexity of the angular momentum structure in a core decreases over time. Moreover, I perform synthetic observation and show that the angular momentum profile measured from the mean velocity map is compatible with the observations. The present result provides a convenient test for the theory of core formation in the filament with the observed velocity field in the filaments and angular momentum structures in the cores.

Acknowledgments

I would like to thank my supervisor, Shu-ichiro Inutsuka, for giving me interesting theme and fruitful discussion. I also would like to thank Doris Arzoumanian for helpful discussion. I am grateful to T. Inoue and D. Abe for providing me their simulation data. I thank H. Kobayashi, M. Kunitomo, S. Takasao, K. Kurosaki, and J. Shimoda for their advice for my presentation and my research and encouragement. Numerical computations were carried out on Cray XC50 at Center for Computational Astrophysics, National Astronomical Observatory of Japan. The computation was carried out using the supercomputer "Flow" at Information Technology Center, Nagoya University.

List of Figures

1.1 Column density map in Aquira molecular cloud by using Herschel Space Observatory (André et al., 2010). The green and blue dots represent the protostar and prestellar core, respectively. The color also corresponds to the stability parameter which is defined as the ratio of line mass to critical line mass. The line mass is calculated by using universal filament width 0.1 pc. 3

1.2 Velocity structure in the filament. The lower left and lower right panel are line-of-sight velocity and velocity dispersion along the filament axis (black dashed line in the upper panel), respectively. The blue and red dots are results from $C^{18}O$ and N_2H^+, respectively. . 4

1.3 Column density map (left) and power spectrum of column density fluctuations (Right) using dust continuum data from Herschel. The black dots are the resultant power spectrum, and the red solid line is fitting result. The slope index is -2.63 ± 0.1. 5

1.4 Power spectrum analysis shown in Roy et al. (2015). The upper panel is an example of filaments that they studied. The black line is the filament axis that they defined using DisPerSE algorithm (Sousbie, 2011). The lower left panel is an example of observed line mass fluctuations along the filament axis. The lower right panel is the histogram of the slope index of the power spectrum of line mass fluctuations. The black and green histogram are results without and with noise subtraction, respectively. 6

1.5 Dispersion relation of filament derived in Inutsuka & Miyama (1992). The vertical axis is the growth rate normalized by free fall time, and horizontal axis is the wavenumber of the z-direction (longitudinal axis of filament). The upper and lower dashed line are the dispersion relation for isothermal compressible and incompressible case, respectively. The solid lines represent $n = 1, 2, 3, 4, 5$ ($P = K\rho^{1+1/n}$) from bottom to top. 7

1.6 Final outcome of simulations Machida et al. (2008). The vertical axis the initial angular velocity of core normalized by initial free fall time, and it is directly related to the angular momentum of cores. The horizontal axis is the strength of magnetic field normalized by thermal pressure. The color behind the panels shows that the object fragments to multiple system at the first core (blue), at the second core (red), no fragmentation (grey), and no collapse (green). 9

1.7 Separation distribution of multiple system observed in Perseus molecular cloud. The dashed line is the fitting result from Raghavan et al. (2010). 10
1.8 Observed angular momentum of astronomical objects. The vertical axis and horizontal axis are the specific angular momentum and the size of objects. 11

2.1 Observations of angular momentum of molecular cloud cores. The horizontal axis is the core mass and the vertical axis is the core specific angular momentum (see text for details). The up-triangles, down-triangles, and circles are observational data from Tatematsu et al. (2016), Goodman et al. (1993), and Caselli et al. (2002), respectively. The green, blue, and magenta solid lines are the results of the fits by applying the least square method to the data of Tatematsu et al. (2016), Goodman et al. (1993), and Caselli et al. (2002), respectively. The values of the slopes of the fits to the data of Tatematsu et al. (2016), Goodman et al. (1993), and Caselli et al. (2002) are 0.5, 0.5, and 0.9, respectively. 15
2.2 Schematic figure describing the calculation of the angular momentum of a core. We calculate the angular momentum and the mass within model cores defined by their length (see Section 2.4). We vary the position of the cores and their length between $\lambda_{\rm min}$ and $\lambda_{\rm max}$ to generate the model $j - M$ relation. 16
2.3 $j - M$ relation obtained from 3D Kolmogorov turbulence power spectrum model (Section 3.1). The red filled circles and the solid line represent the numerical and the analytical results, respectively. The observational data are the same as in Figure 2.1. 20
2.4 Example of the superposition of different fluctuating modes along the filament. In the region with a length $L_{\rm core}$ the wave represented by the solid line arrows is the most important for the angular momentum (left) and the wave represented by the dashed line arrows mostly cancels and hence does not significantly contribute to the angular momentum of this region (right). 21
2.5 (left) The horizontal axis is the wavenumber and the vertical axis is the energy spectrum. The region between the two black dashed lines represents the range of wavenumber that we used. (right) $j - M$ relation derived from the log-normal power spectrum model with fixed value, $k_{\rm peak} = 2\pi/(0.1{\rm pc})$. The red, blue, and green solid lines correspond to $\sigma_G = 0.35, 0.5$, and 0.65, respectively. The observational data are the same as in Figure 2.1. 22
2.6 (left) Same as Figure 2.5 for fixed $\sigma_G = 0.5$ and varying $\lambda_{\rm peak}$. (right) $j - M$ relation derived from the log-normal power spectrum model with fixed value $\sigma_G = 0.5$. The green, red, blue, and magenta solid lines correspond to $\lambda_{\rm peak} = 1.0, 0.5, 0.1$, and 0.05 pc. $\lambda_{\rm peak}$ is defined as $k_{\rm peak} = 2\pi/\lambda_{\rm peak}$. The observational data are the same as in Figure 2.1. 23

2.7 Dependence of the index of the $j - M$ relation slope on the two parameters, σ_G and $k_{\rm peak}$. The horizontal axis is $k_{\rm peak}$ and the vertical axis is σ_G. The indices are derived by applying the least square fitting method to the $j - M$ relation in the mass range $1 - 10$ $M_\odot$. 24
2.8 $j - M$ relation for a compressible velocity field. The red solid line is the result obtained from the expression for the potential field shown in Equation 2.12, and the log-normal power spectrum Equation 2.18 with $\sigma_G = 0.5$ and $\lambda_{\rm peak} = 0.1$ pc. The observational data are the same as in Figure 2.1. 25
2.9 Color contour of power spectrum. Isotropic 3D Kolmogorov power spectrum (left) and anisotropic model derived from Equation 2.19 with $A_r = 0.01$ (right). 26
2.10 $j - M$ relation for anisotropic power spectrum. The red dashed line and blue solid line are isotropic 3D Kolmogorov power spectrum (same as Figure 2.3) and anisotropic power spectrum model derived using Equation 2.19, $A_r = 0.01$ respectively. The observational data are the same as in Figure 2.1. 27
2.11 $j - M$ relation for 1D Kolmogorov power spectrum. The red dashed line and blue solid line are 3D Kolmogorov power spectrum (same as Figure 2.3) and 1D Kolmogorov power spectrum model derived using Equation 2.20, respectively. The observational data are the same as in Figure 2.1. 28

3.1 Schematic figure of simulation of Abe et al. (2021) (their Figure 1). The color represents the number density of hydrogen molecule. The black line is magnetic field, and their direction along the y direction at the initial state. 32
3.2 Schematic figure of setup of Inoue et al. (2018) (their Figure 1). The color represents the column density. The small cloud with turbulence is swept by plain parallel shock wave. 33
3.3 Column density map on $x - y$ plane. The color is the column density 34
3.4 Same as Figure 3.3, but the white lines represent the filament axis. 35
3.5 Examples of power spectrum of velocity and line mass fluctuations. The blue dots result from analysis explained in previous section, and the red lines are fitting results. 36
3.6 Histograms of slope index of line mass fluctuations, respectively. The top left, top right, bottom left, and bottom right panels are the results at 0.3, 0.4, 0.5, and 0.6 Myr, respectively. 37
3.7 Histograms of slope index of velocity fluctuations, respectively. The top left, top right, bottom left, and bottom right panels are the results at 0.3, 0.4, 0.5, and 0.6 Myr, respectively. 38
3.8 Column density map (left panel) and the power spectrum of column density (right panel). The black line in the left panel is the filament axis identified by using FilFinder. The red dots in right panel are resultant power spectrum derived from Equation 3.10, and the blue solid line is the fitting line whose slope index is -2.4 ± 0.6. 38

4.1 Time sequence of the fragmentation of a filament (from panel (a) to (d)). The color scale is the column density derived by integrating the density along the y-axis. The elapsed time and maximum density are denoted in each panel, where $t_{\rm ff}$ is the free fall time defined by $t_{\rm ff} = (4\pi G\rho_{\rm c})^{-1/2}$. 40
4.2 Time sequence of morphology and specific angular momentum of a core from left to right. The first, second, and third row are on the x-y, x-z plane, and y-z plane, respectively. The color scale is the specific angular momentum of SPH particles. **This core is defined by the density contour enclosing a mass of** 1 $M_\odot$ **at final time step.** The panels from left to right are snapshots at stages of $n = 4.192\times10^4{\rm cm}^{-3}$, $n = 1.675\times10^5{\rm cm}^{-3}$, and $n = 7.574\times10^9{\rm cm}^{-3}$, respectively. The elapsed time and maximum density are denoted in each panel. 42
4.3 (left)The time evolution of the absolute value of the specific angular momentum of the core shown in Figure 4.2. The horizontal axis is the maximum density of the core. The density evolution traces also the time evolution as the core collapses. (right)The time evolution of the component of the specific angular momentum of the core shown in Figure 4.2. **The red dashed line, blue solid line, and green dotted line** are the x, y, and z components of the specific angular momentum. The vertical axis is logarithmic in the left panel but linear in the right panel. 43
4.4 Gravitational torque (left) and pressure torque (right) exerted on the core. The horizontal axis is the maximum density of the core and the vertical axis is the torque. The red, blue, and green curves are the x, y, and z components of the torque. 44
4.5 Total torque exerted on the core. The horizontal axis is the maximum density of the core and the vertical axis is the total torque $\boldsymbol{T} = \boldsymbol{T}_{\rm f} + \boldsymbol{T}_{\rm g}$. The red, blue, and green are the x, y, and z components of the total torque. 45
4.6 The time evolutions of the specific angular momentum of the 38 cores. The horizontal axis is the maximum density of the cores. The different colors of solid lines correspond to the different cores derived from the 38 runs. 46
4.7 The averaged time evolutions of the specific angular momentum of the cores. The red solid line is the averaged specific angular momentum of the 38 cores shown in Figure 4.6. The vertical bars show the dispersion. 48
4.8 The averaged time evolutions of the gravitational torque exerted on the cores. The vertical axis is the gravitational torque. The horizontal axis is the maximum density of the core. 49
4.9 Histograms of the specific angular momentum of the cores at the initial state (left) and at the final state (right) with statistical error bars. The vertical axis is the number of cores per $\log j$ bin. 50

4.10 Histogram of the angle θ between the filament axis and core angular momentum axis at the initial state (left) and at the final state (right) with statistical error bars. The vertical axis is the number of cores per θ bin. 50
4.11 Time evolution of the rotation energy normalized by the thermal energy. The horizontal axis is the maximum density of the core. Each color corresponds to each core. 50
4.12 Distribution of axis ratios of all cores. Each blue circle corresponds to each core. The axis of a core are the eigenvalue of inertia moment, and $a_1 < a_2 < a_3$. The three dashed lines are the boundaries between prolate, triaxial, and oblate shapes from left to right. . . . 51
4.13 Internal angular momentum structure. The vertical axis is the specific angular momentum of a shell. The horizontal axis is **the total mass enclosed by the shell**. The different colors of solid lines coresspond to the different cores. The black dashed line represents $j \propto M$. 52
4.14 Time evolution of j-M profile in a core. The black dashed line is $j \propto M$. The j-M profiles of the core evolve from the blue line to the red line. 53
4.15 Averaged j-M profile for the 38 cores. The red solid line is the averaged j-M profile using all j-M profiles of the cores shown in Figure 4.13. The black dashed line is $j \propto M$. 53
4.16 Angular momentum profile in the cores. The vertical axis is the specific angular momentum of a core, and the horizontal axis is the distance from the density peak of the core. In the left **panel**, each color corresponds to each core. The black dash-dotted line, dashed line, and dotted line are $j \propto r^1$, $j \propto r^{1.5}$, and $j \propto r^2$, respectively. The blue line in the right **panel** is the averaged j-r profile of the cores shown in the **left panel**. 54
4.17 Time evolution of the angle between the core rotation axis and the filament axis. The vertical axis is the maximum density of a core. The horizontal axis is the enclosed mass within the shell. 55
4.18 Rate of angular momentum transfer due to the total torque during the runaway collapse phase. The vertical axis is the maximum density of a core. The horizontal axis is the enclosed mass within the shell. The color shows the efficiency of angular momentum transfer which is defined by the ratio of the torque acting on the shell during the collapse $Tt_{\rm ff}$ to angular momentum of the shell J, where $t_{\rm ff}$ is the free fall time at each time step, and $\langle\ \rangle$ represents the ensemble average for the 38 cores. 56

4.19 Sign of the total (upper panel),pressure (lower left panel), and gravitational (lower right panel) torques with respect to the angular momentum during the runaway collapse phase. The vertical axis is the maximum density of a core. The horizontal axis is the total mass within the shell. The hat symbol means the unit vector. The color shows the inner product between the unit vector of angular momentum and the unit vector of the total (upper panel), pressure (lower left panel), and gravitational (lower right panel) torques. . . 57
4.20 3D plots of the velocity structure in cores formed in our simulations. The upper and lower panels are smooth and complex velocity structure cases, respectively. The isosurfaces represent the isodensity surfaces, $\rho = 3.0 \times 10^{-19}$g cm^{-3} ($n = 7.8 \times 10^4$cm^{-3}) (upper panel) and $\rho = 3.5 \times 10^{-19}$g cm^{-3} ($n = 9.1 \times 10^4$cm^{-3}) (lower panel). The blue arrows are the direction of the rotation velocity. The central densities of the cores are $\rho = 8.0 \times 10^{-19}$g cm^{-3} ($n = 2.0 \times 10^5$cm^{-3}) (upper panel) and $\rho = 1.2 \times 10^{-18}$g cm^{-3} ($n = 3.1 \times 10^5$cm^{-3}) (lower panel) 59
4.21 Angle between the angular momentum vector of the inner region and the outer shell with the same mass as the inner region. **Here, we define the inner region as the region enclosed by the outer shell. The color scale represents the angle between the rotation axis of the inner region and the outer shell averaged over all the cores.** The horizontal axis is the total mass within the shell. The vertical axis is the maximum density of a core. 60
4.22 **Histograms of the angles between the angular momentum of the inner region with mass** 0.02 $M_\odot$ **and the outer shell with the same mass for 38 cores at the initial state (left) and at the final state (right) with statistical error bars.** Note that the scales of the x-axis are not the same on both panels. 60
4.23 Time evolution of the angular velocity derived from Equation 4.23. The vertical axis is the normalized angular velocity of the central region of the cores. The horizontal axis is the maximum density of the cores. The different colors of the solid lines correspond to the different cores. The black dashed line is $\omega \propto \rho_c^{1/6}$ discussed in Hanawa & Nakayama (1997). 62
4.24 Histogram of angular velocity derived from Equation 4.23. The horizontal axis is the normalized angular velocity of the central region of the cores. The error bars refer to the standard deviation. 62
4.25 Column density map (left) and line-of-sight velocity map (right) around the core at the final state of the simulation. **In these plots, the longitudinal axis of the filament is parallel to the plane of sky.** 66
4.26 Same as Figure 4.25 for the case where the filament is inclined by 30° with respect to the plane of the sky. 66

4.27 Relation between the specific angular momentum and the radius from the core center. The red solid line is the relation between specific angular momentum and radius from core center derived from the line-of-sight velocity map. The blue solid line is result from the rigid body rotation fitting using Equation 4.33. The left and right panels are for not-inclined and for inclined model, respectively. The black dots are the observation data. The circles, squares, crosses, pluses, stars, down-triangles, and up-triangles are observational data from Pineda et al. (2019), Chen et al. (2019a), Punanova et al. (2018), Tobin et al. (2011), Caselli et al. (2002), Goodman et al. (1993), and Tatematsu et al. (2016). The green and purple solid lines are $j \propto r^{1.5}$ and $j \propto r^2$ just for comparison. . 67
4.28 j-r relation for all cores. The different colors correspond to the different cores. The others are same as Figure 4.27. 68
4.29 Averaged j-r relation for without the inclination (left) and with inclination(right). The error bars refer to the standard deviation. The others are same as Figure 4.27. 68
4.30 Comparison of j_{2D} to the observational data. The left and right panels are for not-inclined and for inclined models, respectively. The blue and red histograms are distributions of j_{2d} and measured specifinc angular momentum in Punanova et al. (2018). 69
4.31 Effect of accretion onto cores on j-r diagram. The blue solid line is the averaged j-r relation with inclination of the filament. The purple solid line is j-r relation with only z-component of fluctuations. The others are same as Figure 4.27. 70
4.32 Effect of accretion along the filament axis on the apparent measured angular momentum of the core. The vertical axis is the ratio of the core angular momentum measured in the line of sight velocity map with inclination with respect to that without inclination. The horizontal axis is the **minimum** density for the definition of core. **Please note that the core definition adopted here differs from that used in Section 4.2.2.** 71
4.33 Averaged time evolution of specific angular momentum measured in line-of-sight velocity maps such as Figure 4.25 and 4.26. **In this plot, we measure the 2d angular momentum in the line-of-sight velocity map whose area is 0.05pc $\times$ 0.05pc at each time step. Note that, since the size of area of the line-of-sight velocity map is fixed in this measurement, the mass contained in the region increases with time.** The horizontal axis is the maximum density of the core, and the vertical axis is the specific angular momentum measured in line-of-sight velocity maps. The solid line is the specific angular momentum evolution that is averaged over all cores. The red solid line and blue solid line are the results with the inclination and without inclination, respectively. 71

4.34 Comparison of averaged j-M profile. The blue, red, orange, and green solid lines are j-M relations with $\sigma = 0.5c_{\rm s}$, $\sigma = 0.7c_{\rm s}$, $\sigma = c_{\rm s}$, and $\sigma = 2c_{\rm s}$, respectively. The black dashed line is $j \propto M$. 72
4.35 Comparison of the observed j-r relation without inclination of filament (left) and with inclination of filament (right). The orange and green solid lines are observed j-r relations with $\sigma = c_{\rm s}$ and $\sigma = 2c_{\rm s}$, respectively. The black dashed line and dotted line are $j \propto r^{1.5}$ and $j \propto r^2$ just for comparison. 73
4.36 j-M diagram for all cores in our simulations. The vertical axis and horizontal axis are the specific angular momentum and the mass of core, respectively. The red, blue, green, and magenta symbols represent the cores defined at $t = 2, 3, 4$, and 5_tff, respectively. The plus, star, and circle symbols represent the critical density used for definition of core ($1, 2$, and $3\rho_{\rm c}$). The black dots are observational data. The black dashed line is $j \propto M$. The black solid line is fitting result for all cores in simulations. The fitting result is $j \propto M^{0.72\pm0.02}$. 74
4.37 j-R diagram for all cores in our simulations. The vertical axis and horizontal axis are the specific angular momentum and the radius of core, respectively. The black dashed line and dotted line are $j \propto R^{1.5}$ and $j \propto R^2$, respectively. The fitting result is $j \propto R^{2.02\pm0.04}$. . 75
4.38 β-M diagram for all cores in our simulations. The fitting result is $\beta \propto M^{0.18\pm0.02}$. 75
4.39 Histogram of ratio of specific angular momentum derived from line-of-sight velocity map to that measured in 3d. The horizontal axis is logarithmic. 76

List of Tables

2.1 Relative appropriateness of the models. The values in Table 2.1 are the dispersions σ^2_{error} of the observational points relative to the analytical solution in $j - M$ diagram calculated using Equation 2.21 and normalized by σ^2_{error} of the 3D Kolmogorov model (cf., Section 4). 26

Contents

Acknowledgments **i**

List of figures **ii**

List of tables **x**

1 Introduction **1**
1.1 Star Formation in Molecular Clouds 1
1.2 Filamentary Molecular Cloud 1
1.3 Theoretical Understanding of Filamentary Molecular Cloud 3
1.4 Role of Angular Momentum in Star Formation Process 6
1.4.1 Angular Momentum Problem 7
1.4.2 Formation of Multiple System 7
1.4.3 Misaligned Protoplanetary Disks and Planets 8
1.5 Observations of Angular Momentum of Molecular Cloud Cores . . . 9
1.6 Previous Works for Angular Momentum of Molecular Cloud Cores . 10

2 An Origin for the Angular Momentum of Molecular Cloud Cores **13**
2.1 Short Introduction 13
2.2 Analyses 14
2.2.1 Core Angular Momentum Derived from the Observations . . 14
2.2.2 Filament Setup 15
2.2.3 Velocity Field 16
2.2.4 Numerical Calculation of the Angular Momentum 18
2.2.5 Analytical Solution for Isotropic Velocity Field 18
2.3 Results 19
2.3.1 3D Kolmogorov Power Spectrum Model 19
2.3.2 Log-normal Power Spectrum Model 21
2.3.3 Anisotropic Power Spectrum Model 23
2.3.4 1D Kolmogorov Power Spectrum Model 24
2.4 Comparison of the Derived Power Spectrum Models 25
2.5 Discussion 27
2.6 Summary of this Chapter 30

3 Power Spectrum Measured in Filament Formation Simulation 31
3.1 Simulation Setup . . . 31
3.2 Analysis . . . 32
3.3 Results . . . 34
3.4 Summary and Discussion . . . 35

4 Time Evolution of the Angular Momentum of Molecular Cloud Cores 39
4.1 Numerical Setup . . . 39
4.2 Results . . . 41
4.2.1 Overview . . . 41
4.2.2 Core Angular Momentum . . . 41
4.2.3 Statistical Properties of the Total Angular Momentum of the Core . . . 46
4.2.4 Internal Structure of Core Rotation . . . 52
4.2.5 Angular Momentum in the Central Region of the Cores . . . 61
4.3 Discussion . . . 63
4.3.1 An Origin for the Specific Angular Momentum Profile in a Core . . . 63
4.3.2 Effect of Filamentary Structure on the Angular Momentum of Cores . . . 64
4.3.3 Comparison with Observations . . . 66
4.3.4 Dependence on the Turbulence of the Velocity Field . . . 72
4.3.5 Properties of Cores Defined by Density Contours . . . 72
4.4 Summary of this Chapter . . . 77

5 Summary and Future Prospects 78
5.1 Summary of this Thesis . . . 78
5.2 Future Prospects . . . 79
5.2.1 Effect of Magnetic field . . . 79
5.2.2 Formation of Multiple System . . . 80
5.2.3 Application for Massive Star Formation . . . 80

A Derivation of Equations 81
A.1 Derivation of $\boldsymbol{R}(\boldsymbol{k}; L_{\rm core})$ . . . 81
A.2 Derivation of Equation 2.25 . . . 82
A.3 Derivation of Equation 4.11 . . . 82

Chapter 1

Introduction

1.1 Star Formation in Molecular Clouds

The stars are formed in the galaxies, and they evolve with galaxies. For example, the massive stars scatter the heavy element to the interstellar space at the end of their life. Hence how the stars are born in the galaxies is the important question to understand the history of galaxy, that is, fate of the universe. Stars are born in molecular clouds with mean number density around 10^{-3} cm^{-3}, and these molecular clouds are formed by multiple compression of HI gas (Inoue & Inutsuka, 2008, 2009). Molecular cloud cores are dense regions in molecular clouds, and eventually evolve to stars due to gravitational contraction. Therefore, to study properties of molecular cloud cores is significantly important to determine the initial condition of star formation. Recent observations reveals that the filamentary structure is common in the molecular clouds (e.g., André et al., 2014). We introduce recent observational progress in the following section.

1.2 Filamentary Molecular Cloud

In this section, we summarize the observational results about filamentary molecular clouds. Recent Herschel Gould Survey using dust continuum observation reveals that the filamentary structure is ubiquitous in the molecular clouds (André et al., 2010; Arzoumanian et al., 2019; Hacar et al., 2018). Figure 1.1 shows the observational result in Aquira molecular cloud by using Herschel Space Observatory (André et al., 2010). The color corresponds to the column density. As you can see from Figure 1.1, many elongated dense regions can be observed in Aquira molecular cloud. These dense gas structures are called filamentary structure (or filament). These filamentary structures are found in all nearby star forming region (Arzoumanian et al., 2019). In addition, the filamentary structure is also observed even in the no star forming region, for example Polaris molecular cloud (André et al., 2010). The analysis of Herschel Observational data give us the information that the filaments have universal width 0.1 pc (Arzoumanian et al., 2011, 2019). Observations also suggest that the most stars are formed in the filamentary molecular cloud. In Figure 1.1, the green and blue dots represent the protostar and prestellar

core, respectively. Hence Figure 1.1 shows that the protostar and prestellar core are along the filaments. Moreover, the protostar and prestellar core are located only along filaments with line mass larger than critical line mass (See next section). These observations in molecular clouds suggest that thermally supercritical filamentary structure plays a crucial role in the star formation process.

The velocity structure in the filaments is observed using line emission. An example is shown in Figure 1.2. Hacar & Tafalla (2011) measure the velocity fluctuations along the filament axis in Taurus molecular cloud shown in upper panel of Figure 1.2. The lower left and lower right panel are line-of-sight velocity and velocity dispersion along the filament axis, respectively. The blue and red dots are results from $C^{18}O$ and N_2H^+, respectively. Both line-of-sight velocity and velocity dispersion show that the velocity fluctuations in the filament is sub (or tran) sonic. Moreover, Hacar et al. (2016) claims that the velocity structure function deviates from so-called Larson's law Larson (1981), so the velocity field in the site of star formation is more quiet than previously thought.

In addition, the power spectrum in the molecular cloud is also important quantity to predict the distribution of physical properties of cores, that is, stars. For example, the core mass function (CMF) that is initial distribution function of core mass can be theoretically predicted by using Press-Schechter formalism if the initial power spectrum of line mass fluctuations along a filament is given (Inutsuka, 2001). The observed shape of CMF is similar to initial mass function of star (IMF), but the peak position of CMF is about three times larger than that of IMF. Therefore, to investigate the initial density power spectrum is very important to understand the origin of IMF. Roy et al. (2019) presents the power spectrum of column density fluctuations in Polaris molecular cloud as shown in Figure 1.3. They measure the power spectrum of column density fluctuations using dust continuum data from Herschel, and the resultant spectrum is displayed in right panel of Figure 1.3. The black dots are the resultant power spectrum, and the red solid line is fitting result. The slope index is -2.63 ± 0.1. Moreover, Roy et al. (2015) investigate the power spectrum of line mass fluctuations statistically. The upper panel of Figure 1.4 is an example of filaments that they studied. The black line is the filament axis that they defined using DisPerSE algorithm (Sousbie, 2011). The lower left panel is an example of observed line mass fluctuations along the filament axis. They derived the power spectrum of these line mass fluctuations of each filament. The resultant histogram of the slope index of the power spectrum of line mass fluctuations is shown in lower right panel of Figure 1.4. The black and green histogram are results without and with noise subtraction, respectively. The peak position of the green histogram is located around ~ -1.5. This is good agreement with theoretical prediction in Inutsuka (2001) that, if the line mass fluctuations in the filaments follows the power spectrum with slope index -1.5, the origin of CMF slope can be explained.

These observations suggest that the filament is suitable initial condition of star formation in the molecular clouds, and it makes the study of star formation process simplify compared to molecular cloud scale simulation with supersonic turbulence (e.g., Offner et al., 2008).

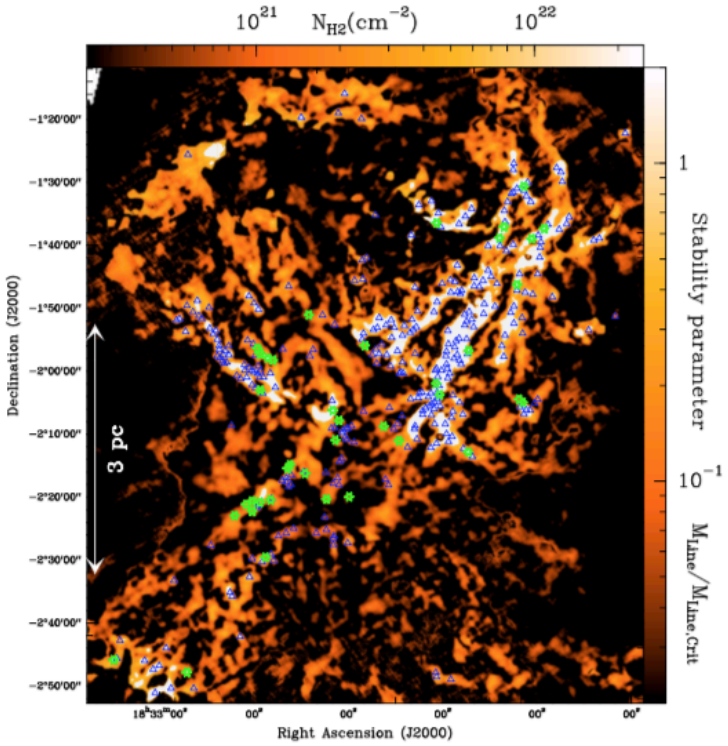

Figure 1.1: Column density map in Aquira molecular cloud by using Herschel Space Observatory (André et al., 2010). The green and blue dots represent the protostar and prestellar core, respectively. The color also corresponds to the stability parameter which is defined as the ratio of line mass to critical line mass. The line mass is calculated by using universal filament width 0.1 pc.

1.3 Theoretical Understanding of Filamentary Molecular Cloud

In this section, we summarize the theoretical works about filamentary molecular clouds. The hydrostatic equilibrium of filament is described as follows (Stodólkiewicz, 1963; Ostriker, 1964):

$$\rho(r) = \rho_{\rm c} \left[1 + \left(\frac{r}{H_0}\right)^2\right]^{-2}, \tag{1.1}$$

where r is the radius in cylindrical coordinate. H_0 is defined as follows:

$$H_0 \equiv \sqrt{\frac{2c_{\rm s}^2}{\pi {\rm G} \rho_{\rm c}}}, \tag{1.2}$$

where $c_{\rm s}$ is the sound speed. The line mass (mass per unit length) is defined as follows:

$$M_{\rm line,\ crit} \equiv \int_0^\infty 2\pi\rho(r) r dr = \pi H_0^2 \rho_{\rm c} = \frac{2c_{\rm s}^2}{\rm G}. \tag{1.3}$$

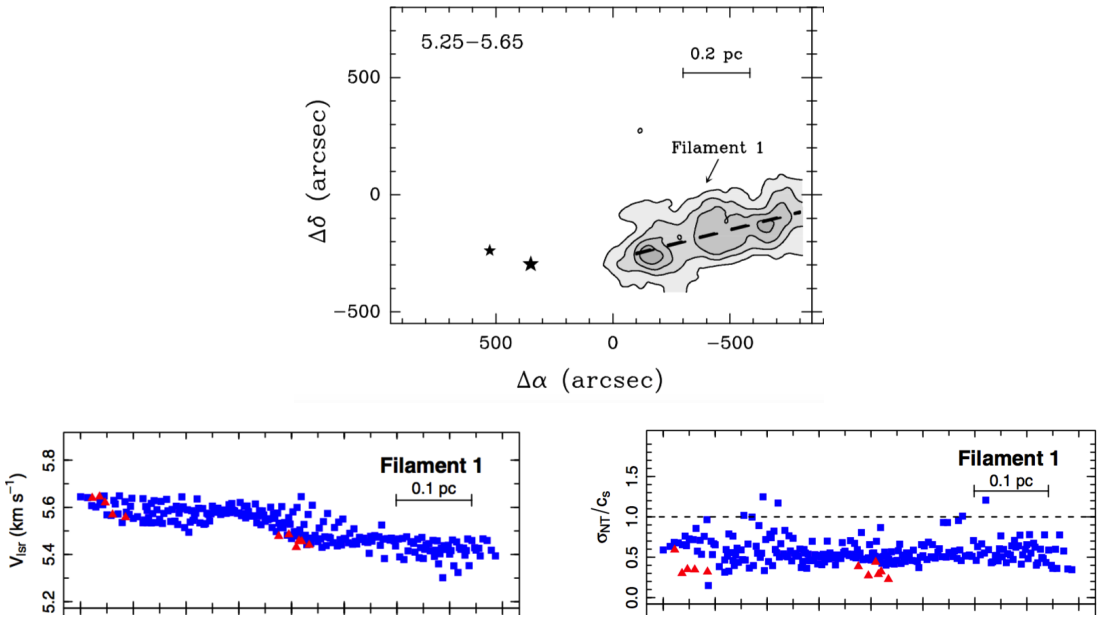

Figure 1.2: Velocity structure in the filament. The lower left and lower right panel are line-of-sight velocity and velocity dispersion along the filament axis (black dashed line in the upper panel), respectively. The blue and red dots are results from $C^{18}O$ and N_2H^+, respectively.

Note that the line mass is determined only by sound speed, that is, temperature. The filament with line mass larger than $M_{\rm line,\ crit}$ cannot be in the hydrostatic equilibrium state, and it collapses radially. Therefore, $M_{\rm line,\ crit}$ is called critical line mass. At $T = 10$K (typical temperature of molecular cloud), the critical line mass is equal to 18 $M_\odot pc^{-1}$. This can be understood as follow. From Poisson equation, the gravity at $r = R$ can be described as follows:

$$F_{\rm g,cyl} = 2\frac{GM_{\rm line}}{R} \propto \frac{1}{R}. \tag{1.4}$$

On the other hand, the pressure term is

$$F_{\rm p} = \frac{1}{\rho}\frac{\partial P}{\partial r} \propto R^{1-2\gamma_{\rm eff}}, \tag{1.5}$$

where $\gamma_{\rm eff}$ is polytropic index. Using Equation 1.4 and eq:Ff, the ration of pressure to gravity is

$$\frac{F_{\rm p}}{F_{\rm g,cy1}} \propto R^{2-2\gamma_{\rm eff}}. \tag{1.6}$$

Equation 1.6 indicate that $F_{\rm p} = F_{\rm g}$ at certain line mass when $\gamma_{\rm eff} = 1$ (isohtermal). This line mass is called critical line mass. When the line mass is larger than critical line mass and $\gamma_{\rm eff} = 1$, the collapse cannot be stopped at any radius.

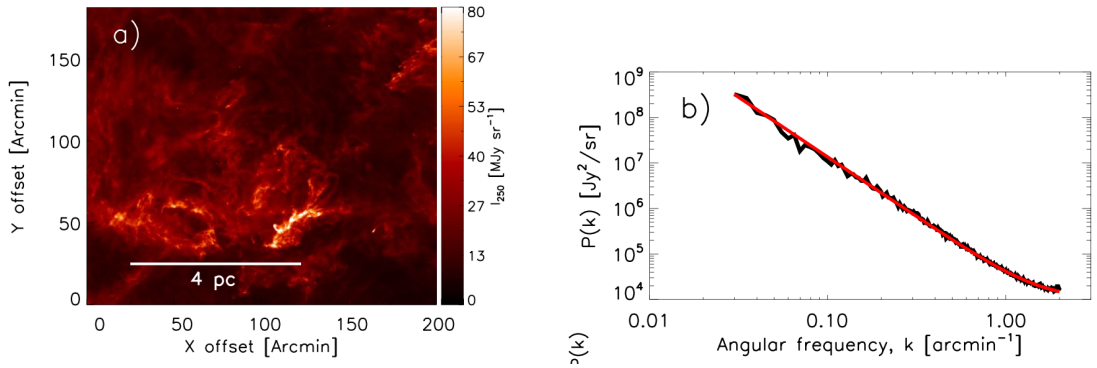

Figure 1.3: Column density map (left) and power spectrum of column density fluctuations (Right) using dust continuum data from Herschel. The black dots are the resultant power spectrum, and the red solid line is fitting result. The slope index is -2.63 ± 0.1.

The linear stability analysis for filamentary structure was done in Inutsuka & Miyama (1992). Figure 1.5 is a dispersion relation of filament derived in Inutsuka & Miyama (1992). The vertical axis is the growth rate normalized by free fall time, and horizontal axis is the wavenumber of the z-direction (longitudinal axis of filament). The upper and lower dashed line are the dispersion relation for isothermal compressible and incompressible case, respectively. The solid lines represent $n = 1, 2, 3, 4, 5$ ($P = K\rho^{1+1/n}$) from bottom to top. Since, in this thesis, we treat the isothermal and compressible filamentary molecular cloud, we focus on the top dashed line in Figure 1.5. As one can see from Figure 1.5, the dispersion has the most unstable wavelength. Therefore, the filament can fragment and form the chain of cores before they globally collapse (i.e. before longer waves grow). While the most unstable wavelength can be derived analytically in the incompressible case (Chandrasekhar, 1961), in the compressible case we have to calculate the most unstable wavelength numerically using shooting method, or finite differential method, so on. The numerical calculation suggests that the filament is unstable against $m = 0$ mode (sausage mode), but stable $m \geq 1$ modes (Nagasawa, 1987). The resultant most unstable wavelength is as follows (Nagasawa, 1987):

$$k_m = 0.284 \left(4\pi G\rho_c\right)^{1/2} / C_s, \tag{1.7}$$

and growth rate is

$$|\omega_m| = 0.339 \left(4\pi G\rho_c\right)^{1/2}. \tag{1.8}$$

Equation 1.7 indicate that the most unstable wavelength is about 8 times larger than H_0. Even if the effect of magnetic field is included, the filaments are unstable for fragmentation (Nagasawa, 1987; Matsumoto et al., 1994; Hanawa et al., 2017).

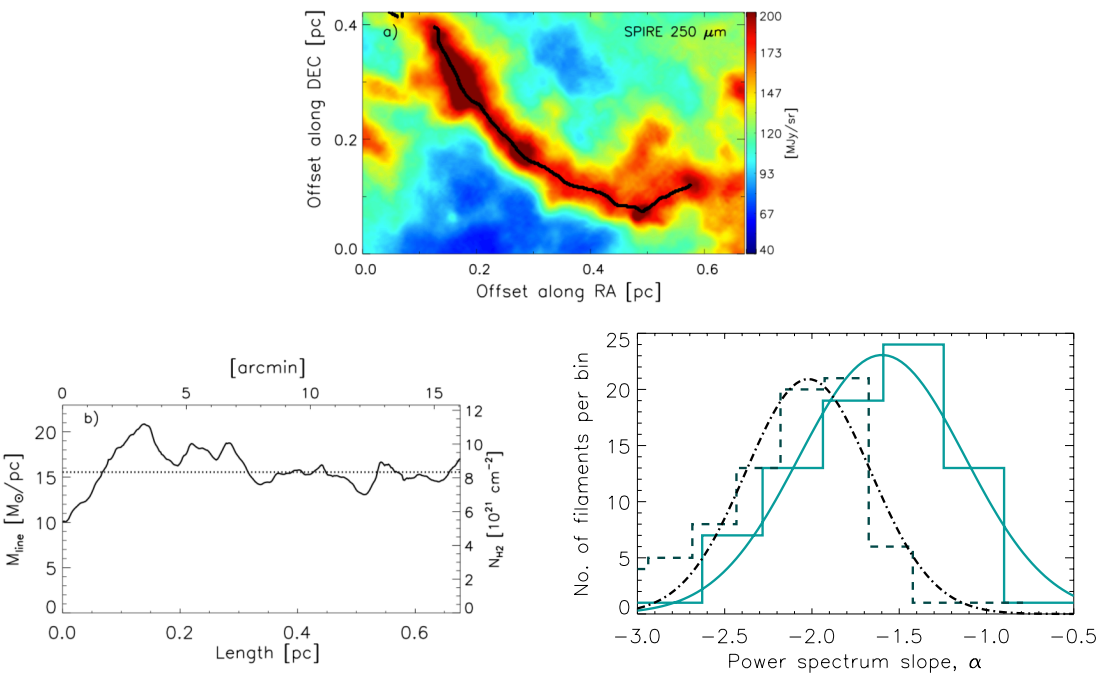

Figure 1.4: Power spectrum analysis shown in Roy et al. (2015). The upper panel is an example of filaments that they studied. The black line is the filament axis that they defined using DisPerSE algorithm (Sousbie, 2011). The lower left panel is an example of observed line mass fluctuations along the filament axis. The lower right panel is the histogram of the slope index of the power spectrum of line mass fluctuations. The black and green histogram are results without and with noise subtraction, respectively.

1.4 Role of Angular Momentum in Star Formation Process

One of the common properties of astronomical objects is rotation. In large scale, the galaxies (halo) have rotation because they acquire the angular momentum from interaction of the initial density fluctuations (Peebles, 1969; Doroshkevich, 1970; White, 1984). The velocity gradient of giant molecular clouds can be observed, and the origin is often attributed to shear motion in the galaxy (Braine et al., 2018, 2020; Imara et al., 2011; Imara & Blitz, 2011). However, galaxy shear is too small to explain the velocity gradient observed in molecular cloud core scale. Hence we have the following question: what is an origin for the angular momentum of molecular cloud cores? Burkert & Bodenheimer (2000) pointed out that the observed angular momentum of cores can be reproduced by turbulence in the cores. This kind of previous works and observational results of angular momentum of cores are discussed in the following sections. In this section, we summarize the role of the angular momentum of molecular cloud cores during the star formation process.

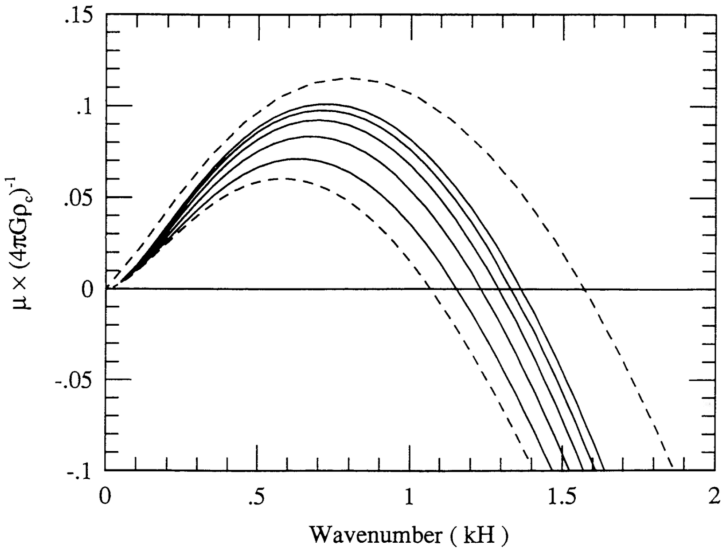

Figure 1.5: Dispersion relation of filament derived in Inutsuka & Miyama (1992). The vertical axis is the growth rate normalized by free fall time, and horizontal axis is the wavenumber of the z-direction (longitudinal axis of filament). The upper and lower dashed line are the dispersion relation for isothermal compressible and incompressible case, respectively. The solid lines represent $n = 1, 2, 3, 4, 5$ ($P = K\rho^{1+1/n}$) from bottom to top.

1.4.1 Angular Momentum Problem

Typical value of the angular momentum of molecular cloud cores is $\sim 10^{21}$cm^2 s^{-1}. On the other hand, the angular momentum of our Sun is $\sim 10^{15}$cm^2 s^{-1}. Therefore, to create our Sun, molecular cloud cores have to lose the angular momentum during their gravitational contraction phase. Otherwise they cannot contract to form the Sun because their centrifugal radius is several hundreds AU. This problem is referred to angular momentum problem (Spitzer, 1978; Bodenheimer, 1995; Belloche, 2013a). The evolution of angular momentum from the molecular cloud core to the protostar has already been well studied using magneto hydrodynamics simulations. Recent theoretical works shows that the outflow and the jet launched from central region and the magnetic braking can sufficiently remove the angular momentum(Machida et al., 2007). However, the evolution of angular momentum from the filamentary molecular cloud to the cores is still unclear.

1.4.2 Formation of Multiple System

Most stars are in the multiple systems (Duquennoy & Mayor, 1991; Raghavan et al., 2010; Sana et al., 2012, 2014; Duchêne & Kraus, 2013; Moe & Di Stefano, 2017; Moe et al., 2019). Moreover, young stars have higher multiplicity compared with field stars (Looney et al., 2000; Chen et al., 2013). Therefore, to understand the star formation process, it is crucial to reveal the formation mechanism of multiple system. The fragmentation process during the evolution from molecular cloud

core to protostar has been investigated by many authors (e.g., Price & Bate, 2007; Hennebelle & Teyssier, 2008; Machida et al., 2008). Machida et al. (2008) perform the magneto hydrodynamics simulations to calculate the collapse of molecular cloud cores and to investigate the how and when the cloud fragments to multiple system. They change the initial condition and study the dependence of property of resultant multiple system on initial condition of molecular cloud core. Figure 1.6 displays final outcome of simulations Machida et al. (2008). The vertical axis the initial angular velocity of core normalized by initial free fall time, and it is directly related to the angular momentum of cores. The horizontal axis is the strength of magnetic field normalized by thermal pressure. The color behind the panels shows that the object fragments to multiple system at the first core (blue), at the second core (red), no fragmentation (grey), and no collapse (green). Figure 1.6 shows that resultant properties of multiple system depend on the initial angular momentum and magnetic field of initial molecular cloud core. Therefore, deriving the distribution of angular momentum of cores is important to understand the formation of multiple system.

One of the interesting observational results is shown in Tobin et al. (2016). Figure 1.7 is the separation distribution of multiple system observed in Perseus molecular cloud. As one can see from Figure 1.7, the separation distribution of multiple system shows the bi-modal distribution. This can be interpreted as the result from the disk fragmentation and turbulent fragmentation. The short period binary can be formed by the same mechanism as shown in Machida et al. (2008). On the other hand, the mechanism of the long period binary is proposed in Offner et al. (2010), which is called turbulent fragmentation. In this process, the long period binaries are formed by local compression due to turbulence and fragmentation in resultant asymmetric structure. This process has been also studied in other paper (Offner et al., 2016; Lee et al., 2019; Kuffmeier et al., 2019), but theoretical explanation of statistical properties of multiple system is not enough. In addition, The relation between the mechanism of formation of wide binary and filament fragmentation process is not well understood. Therefore, more theoretical explanation for statistical properties of multiple system, especially for wide binary system, is needed.

1.4.3 Misaligned Protoplanetary Disks and Planets

Protoplanetary disk is a birth place of the planets. The properties of protoplanetary disk (e.g., size, mass) inherit from the properties of parental molecular cloud core. Therefore, studying the angular momentum distribution in cores is important to understand the diversity of protoplanetary disk. Recent observations find the diversity of protoplanetary disk. For example, the disk whose rotation axis depends on the distance from the central star is frequently observed, and it is called warp disk (Marino et al., 2015; Stolker et al., 2017; Benisty et al., 2017; Casassus et al., 2018; Muro-Arena et al., 2020; Loomis et al., 2017; Mayama et al., 2018; Sakai et al., 2019). Moreover, the misalignment between spin axis of star and direction of orbital angular momentum is also observed in exoplanet system using Rossiter-McLaughlin effect (Winn & Fabrycky, 2015). While the formation

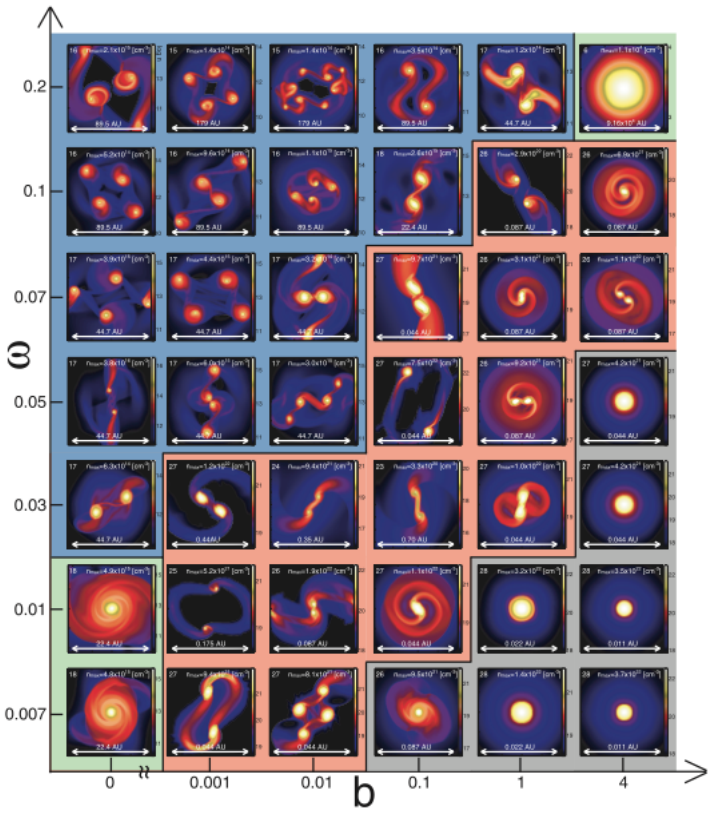

Figure 1.6: Final outcome of simulations Machida et al. (2008). The vertical axis the initial angular velocity of core normalized by initial free fall time, and it is directly related to the angular momentum of cores. The horizontal axis is the strength of magnetic field normalized by thermal pressure. The color behind the panels shows that the object fragments to multiple system at the first core (blue), at the second core (red), no fragmentation (grey), and no collapse (green).

mechanism of these complex structures is still under debate, it should be related to the angular momentum structure in the parental molecular cloud core. In fact, numerical simulations show that warp and complex structure of disk can be created in the turbulent molecular cloud core (Matsumoto et al., 2017; Takaishi et al., 2021). Hence, to determine the frequency of these complex structures is important to predict the diversity of protoplanetary disk and exoplanet system and to understand whether our solar system is general or not.

1.5 Observations of Angular Momentum of Molecular Cloud Cores

In this section, I summarize the observational results of angular momentum of molecular cloud cores. In observations, the angular momentum of objects is estimated using line-of-sight velocity (or moment 1) map (e.g., Fleck & Clark, 1981; Goldsmith & Arquilla, 1985). They interpret the velocity gradient in the line-of-

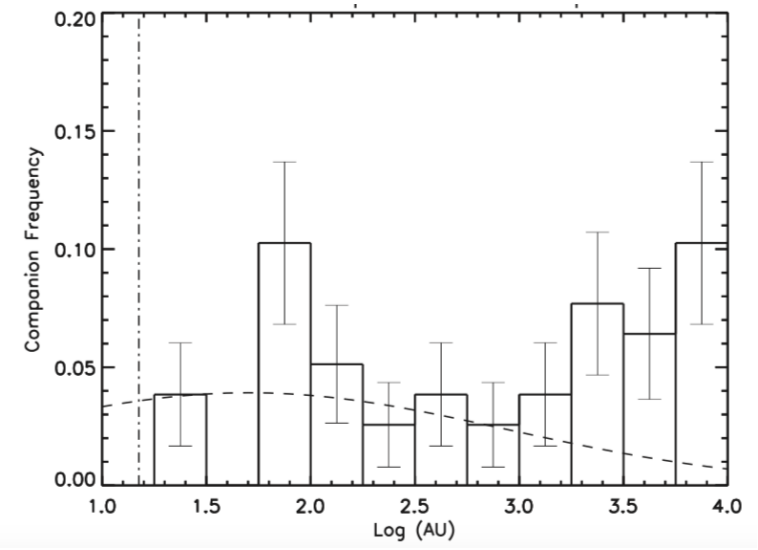

Figure 1.7: Separation distribution of multiple system observed in Perseus molecular cloud. The dashed line is the fitting result from Raghavan et al. (2010).

sight velocity map as rotation. Observed angular momenta among various scales are summarized in Figure 1.8. The vertical axis and horizontal axis are the specific angular momentum and the size of objects. The figure is divided by vertical dashed lines. In the left region, It is expected that the rotation profile follows $j \propto r^{0.5}$ due to the formation of rotational support disk, that is, Keplerian disk. In the middle region, flat profile is observed. This is because the inner region collapses faster than inner region, so the initial angular momentum profile is stretched (Takahashi et al., 2016). In the right region, the objects correspond to the molecular cloud cores and molecular cloud. Many authors carried out observations (Goodman et al., 1993; Caselli et al., 2002; Pirogov et al., 2003; Chen et al., 2007; Tatematsu et al., 2016; Chen et al., 2019b). The relation between anuglar momnetum and radius $j \propto R^{1.6}$ has been observed. More recently, Punanova et al. (2018) measured j-R relation in Taurus molecular cloud, and their resultant relation is $j \propto R^{1.6-2.4}$, consistent with result of Goodman et al. (1993). This relation is often attributed to the turbulence(e.g., Dib et al., 2010), so called Larson's law (Larson, 1981), but the origin of this relation is still unclear. Internal angular momentum profile of envelope of protostar has also been observed (Pineda et al., 2019; Gaudel et al., 2020). Their results also show that the internal profile seems to be compatible with $j \propto r^{1.6}$ in outer region of envelope. However, the origin of this internal structure is also well not understood.

1.6 Previous Works for Angular Momentum of Molecular Cloud Cores

The time evolution and origin of core angular momentum have been investigated using numerical simulations which start from molecular cloud scale.(Offner et al.,

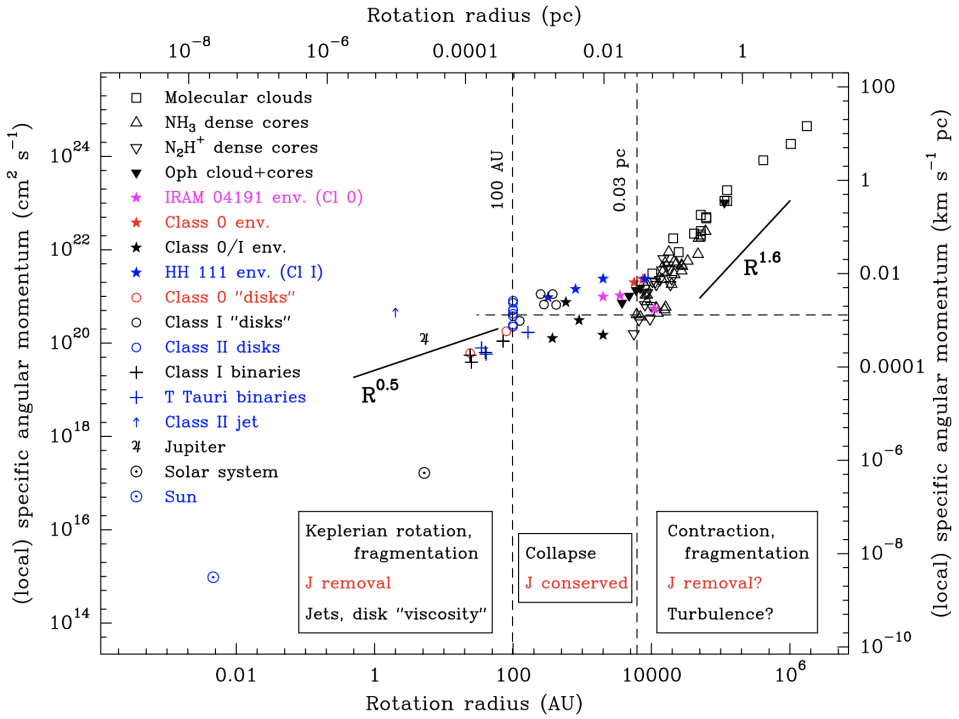

Figure 1.8: Observed angular momentum of astronomical objects. The vertical axis and horizontal axis are the specific angular momentum and the size of objects.

2008; Dib et al., 2010; Chen & Ostriker, 2018; Ntormousi & Hennebelle, 2019; Kuznetsova et al., 2019, 2020; Arroyo-Chávez & Vázquez-Semadeni, 2021). However, they do not focus on the filament fragmentation process. They put the supersonic turbelence in the molecular cloud and perform the three-dimensional simulations. The simulations of Chen & Ostriker (2018) includes the large scale converging flow. Dib et al. (2010), Chen & Ostriker (2018), and Ntormousi & Hennebelle (2019) also include the effect of magnetic field. In Offner et al. (2008) and Dib et al. (2010), their resultant angular momentum of cores is smaller than the observed angular momentum. Dib et al. (2010) claimed that the observation of angular momentum of core tends to overestimate the angular momentum measured in three-dimensional space by an order of magnitude. However, Zhang et al. (2018) showed that the observation underestimates the angular momentum of core within a factor of two or three. On the other hand, Chen & Ostriker (2018) showed the j-R relation measured in their simulations, and their results seem to be consistent with observations. Ntormousi & Hennebelle (2019) also showed the j-R relation, but their resultant angular momentum seems to be larger than observations. Kuznetsova et al. (2019) claimed that the median of AM is consistent with observations, but they did not show the j-r relation. Arroyo-Chávez & Vázquez-Semadeni (2021) investigate the time evolution of angular momentum of core using smoothed particle hydrodynamics (SPH) method. They showed that the core evolves to the observed j-R relation on j-R diagram as time progresses. They also suggest that the angular momentum is transferred by the Reynolds

stress and the pressure gradient terms in the momentum equation. While Offner et al. (2008), Dib et al. (2010), Chen & Ostriker (2018), Ntormousi & Hennebelle (2019) consider that the origin of angular momentum of cores is the turbulence, Kuznetsova et al. (2019) claimed that the cores acquire the angular momentum through the gravitational torque between the high density regions. As described above, the time evolution and origin of angular momentum of core are still unclear, especially the relation between the core angular momentum and filamentary structure in the molecular cloud is not well understood because in previous works, their initial condition is molecular cloud and do not focus on the core formation through the filament fragmentation. In addition, they did not investigate the internal structure of angular momentum of cores in detail. Therefore, the evolution of angular momentum profile in the cores formed through the filament fragmentation process is also still unclear.

Chapter 2

An Origin for the Angular Momentum of Molecular Cloud Cores

This chapter is based on a published paper, Misugi, Inutsuka, & Arzoumanian 2019, Astrophysical Journal, Volume 881, pp. 11-20 (Misugi et al., 2019).

2.1 Short Introduction

The angular momentum of molecular cloud cores plays an essential role in the star formation process, since it is at the origin of the outflow and the jet, results in the formation of the protoplanetary disk, and defines the multiplicity of a stellar system (single star, binary, multiple stars). The angular momentum of a core is defined at the initial conditions of the core formation (e.g., Machida et al., 2008) and understanding how molecular cloud cores obtain their angular momentum is a key question in the star and planet formation studies. The angular momentum of cores has been derived from molecular line observations using the NH_3 transition (Goodman et al., 1993) and N_2H^+ line (Caselli et al., 2002). More recently, Tatematsu et al. (2016) studied a sample of cores in the Orion A cloud and derived their rotation velocity using $N_2H^+ J = 1 - 0$. These observational results have mainly shown two properties of the specific angular momentum of cores j (angular momentum per unit of mass). 1) The range of the specific angular momentum of the cores is $j = 10^{20-22}\mathrm{cm^2 s^{-1}}$, and 2) it is a weakly increasing function of the core mass M, $j \propto M^{0.5-0.9}$. These results are shown in Figure 2.1 (see also Punanova et al. 2018 for other correlations derived from new observations).

Recent results derived from the analysis of Herschel data revealed that stars mainly form in filamentary structures (André et al., 2010; Arzoumanian et al., 2011; Könyves et al., 2015) and the characteristic width of filaments is ~ 0.1 pc (Arzoumanian et al., 2011, 2019; Koch & Rosolowsky, 2015). Moreover, observations show that prestellar cores and protostars form primarily in the thermally critical and supercritical filaments ($\mathrm{M_{line}} \gtrsim \mathrm{M_{line,crit}}$) (André et al., 2010; Tafalla & Hacar, 2015). The line mass $\mathrm{M_{line}}$ of filaments is important for the star formation

process. Theoretically, a thermally supercritical filament is expected to be the site of self-gravitational fragmentation and the birth place of star forming cores (Inutsuka & Miyama, 1997). Therefore, if most of the star forming cores are formed along critical/supercritical filaments, the theory of core formation out of filament fragmentation is expected to explain the origin of angular momentum of the cores.

The three-dimensional velocity structure along the filaments is needed to infer the distribution of the angular momentum of cores. However, the line of sight component of the velocity is solely accessible from molecular line observations. Notse that the line of sight velocity may be dominated by the velocity perpendicular to the axis of filament when the line of sight is nearly perpendicular to the filament axis. The fluctuations of the centroid velocity of filaments close to equilibrium ($M_{line} \sim M_{line,crit}$) is observed to be sub (tran) sonic (Hacar & Tafalla, 2011; Arzoumanian et al., 2013; Hacar et al., 2016). While deriving the velocity power spectrum from molecular line data is observationally difficult, the power spectrum of the column density fluctuation has been already measured in the interstellar medium (ISM) (Miville-Deschênes et al., 2010; Roy et al., 2019) and along a sample of filaments observed by Herschel (Roy et al., 2015). These observations reveal that the power spectrum of the column density fluctuation is consistent with the power spectrum generated by subsonic Kolmogorov turbulence down to the scales of ~ 0.02 pc in the nearest regions (distance ~ 140 pc).

In this paper, we try to establish the relation between velocity fluctuations along the filament and the angular momentum of the cores that result from the fragmentation of the parent filament. Using the available observational data we examine whether we can explain the origin of the angular momentum of cores as a result of the filament fragmentation process.

The structure of the paper is as follows: The method of our calculation is given in Section 2, in Section 3 we show our results. The comparison of the derived models is given in Section 4. Section 5 presents a discussion and suggests implications of our results in the context of star formation. We summarize this paper in Section 6.

2.2 Analyses

In this section, we first mention the observational data used in this paper. Then, we explain the method for calculating the angular momentum of molecular cloud cores formed by filament fragmentation.

2.2.1 Core Angular Momentum Derived from the Observations

Observationally, the specific angular momentum, $j = pRv_{\rm rot}$ (angular momentum per unit of mass) of a molecular cloud core may be derived from the observed radius R of the core, the rotational velocity $v_{\rm rot}$, and p, which is related to the density profile of the core. For a uniform density sphere, $p = 2/5$, while for a singular isothermal sphere $p = 2/9$. Figure 2.1 shows the relation between the specific

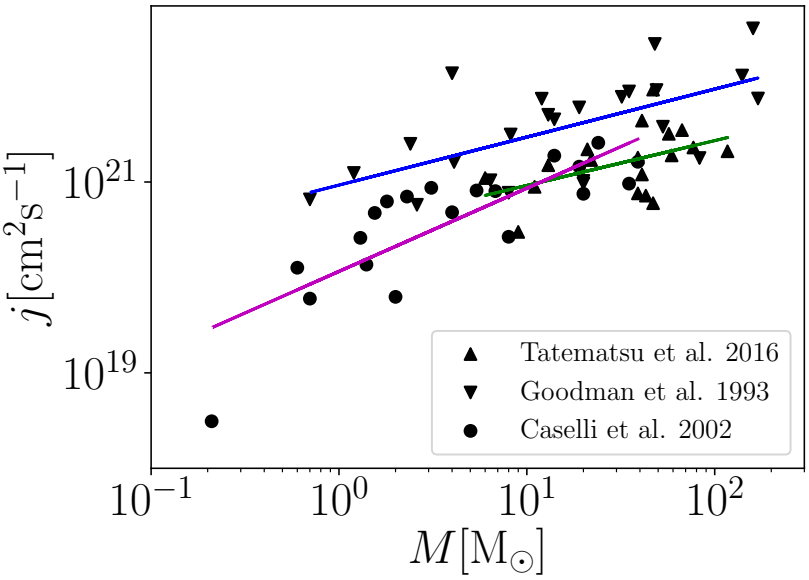

Figure 2.1: Observations of angular momentum of molecular cloud cores. The horizontal axis is the core mass and the vertical axis is the core specific angular momentum (see text for details). The up-triangles, down-triangles, and circles are observational data from Tatematsu et al. (2016), Goodman et al. (1993), and Caselli et al. (2002), respectively. The green, blue, and magenta solid lines are the results of the fits by applying the least square method to the data of Tatematsu et al. (2016), Goodman et al. (1993), and Caselli et al. (2002), respectively. The values of the slopes of the fits to the data of Tatematsu et al. (2016), Goodman et al. (1993), and Caselli et al. (2002) are 0.5, 0.5, and 0.9, respectively.

angular momentum and their mass for a sample of cores studied by Goodman et al. (1993), Caselli et al. (2002), and Tatematsu et al. (2016). Since the specific angular momentum of the cores is not given in Caselli et al. (2002), we derived them using $j = pRv_{\rm rot}$, with the values of $v_{\rm rot}$ from Table 5 in Caselli et al. (2002), R from their Table 3, and $p = 2/5$, which is the same value used in Goodman et al. (1993). For the core masses, we used the $M_{\rm ex}$ values given in Table 4 of Caselli et al. (2002). Note that Figure 2.1 includes very large objects with sizes up to 0.6 pc, which may be clumps instead of real cores (Goodman et al., 1993). While the sample of Goodman et al. (1993) includes very large objects, Caselli et al. (2002) and Tatematsu et al. (2016) do not include such clumps. Our conclusion do not depend on whether these large objects are included or not.

2.2.2 Filament Setup

We consider an unmagnetized isothermal model of filament with a width of 0.1 pc (Arzoumanian et al., 2011, 2019), a uniform density, and a line mass equal to the critical line mass, $\mathrm{M_{line,crit}} = 16\ \mathrm{M_\odot pc^{-1}}$ for $T = 10$ K. An isothermal

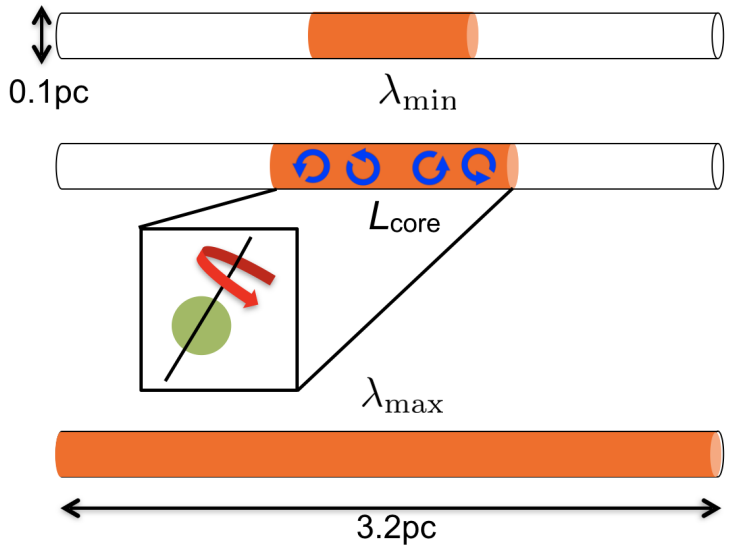

Figure 2.2: Schematic figure describing the calculation of the angular momentum of a core. We calculate the angular momentum and the mass within model cores defined by their length (see Section 2.4). We vary the position of the cores and their length between $\lambda_{\rm min}$ and $\lambda_{\rm max}$ to generate the model $j - M$ relation.

gas filament with line-mass larger than the above value cannot be in equilibrium, without non-thermal support such as magnetic field or internal turbulence.

We define the z-axis along the main axis of the filament and the x- and y-axis the transverse directions (see Figure 2.2). We use 32 grid cells in x and y-axis, and 1024 grid cells in z-axis. We use the periodic boundary condition in this domain. The length of the filament is $L_z = 3.2$ pc, and the total mass of the filament is $\mathrm{M}_{\rm max} = \mathrm{M}_{\rm line,crit} L_z$. $M = \mathrm{M}_{\rm line,crit} L_{\rm core}$ is a mass of a section of the filament where $L_{\rm core}$ is an arbitrary length $\lambda_{\rm min} < L_{\rm core} < \lambda_{\rm max}$, where $\lambda_{\rm min} = 0.03$ pc and $\lambda_{\rm max} = 3.2$ pc. This length range corresponds to the core mass range $0.48\ \mathrm{M}_\odot < M < 51.2\ \mathrm{M}_\odot$. In our model we consider a uniform density filament, while density fluctuations are observed along filaments (Roy et al., 2015). Taking into account such density fluctuations would require a more detailed analysis, which are beyond the scope of this paper presenting first-order calculations toward understanding the angular momentum in the context of filament fragmentation.

2.2.3 Velocity Field

First we numerically generate the velocity field $\boldsymbol{v}$ in the filament following the method described in, e.g., Dubinski et al. (1995)

$$\boldsymbol{v}(\boldsymbol{x}) = \sum_{\boldsymbol{k}} \boldsymbol{V}(\boldsymbol{k}) \exp(\mathrm{i}\boldsymbol{k} \cdot \boldsymbol{x}), \tag{2.1}$$

where $\boldsymbol{V}(\boldsymbol{k})$ is the Fourier transform, $\boldsymbol{k}$ is the wave vector. Since we consider only the periodic function for the velocity fluctuation, we include only the modes that

satisfy the following condition:

$$\boldsymbol{v}(x,y,z) = \boldsymbol{v}(x+L_x,y,z) = \boldsymbol{v}(x,y+L_y,z) = \boldsymbol{v}(x,y,z+L_z), \tag{2.2}$$

where we choose $L_x = L_y = 2R_{\rm fil}$ for simplicity. $R_{\rm fil}$ is the radius of the filament, 0.05 pc in this paper. We define the power spectrum as

$$P(\boldsymbol{k}) = \left\langle |\boldsymbol{V}(\boldsymbol{k})|^2 \right\rangle, \tag{2.3}$$

where $\langle\ \rangle$ represents the ensemble average. We describe in the following how we generate the Fourier component of $\boldsymbol{V}(\boldsymbol{k})$ for a given power spectrum $P(\boldsymbol{k})$ for both incompressible and compressible velocity fields.

Incompressible Velocity Field

For an incompressible fluid, $\boldsymbol{v} = \boldsymbol{\nabla} \times \boldsymbol{A}$, where $\boldsymbol{A}$ is the vector potential,

$$\boldsymbol{A}(\boldsymbol{x}) = \sum_{\boldsymbol{k}} \boldsymbol{A}_{\boldsymbol{k}} \exp(\mathrm{i}\boldsymbol{k}\cdot\boldsymbol{x}), \tag{2.4}$$

where $\boldsymbol{A}_{\boldsymbol{k}}$ is its Fourier transform. The Fourier component of the velocity field is

$$\boldsymbol{V}(\boldsymbol{k}) = \mathrm{i}\boldsymbol{k} \times \boldsymbol{A}_{\boldsymbol{k}}. \tag{2.5}$$

We generate the Fourier component of the vector potential $\boldsymbol{A}_{\boldsymbol{k}}$ as a random Gaussian number with a prescribed power spectrum, $P(\boldsymbol{k}) = (2/3)k^2 \left\langle |\boldsymbol{A}_{\boldsymbol{k}}|^2 \right\rangle$. Finally, we derive the velocity field in real space by performing the inverse transform of $\boldsymbol{V}(\boldsymbol{k})$.

Compressible Velocity Field

We can also setup a compressible velocity field as, $\boldsymbol{v} = \boldsymbol{\nabla}\phi$, where ϕ is the scalar potential,

$$\phi(\boldsymbol{x}) = \sum_{\boldsymbol{k}} \phi_{\boldsymbol{k}} \exp(\mathrm{i}\boldsymbol{k}\cdot\boldsymbol{x}), \tag{2.6}$$

and $\phi_{\boldsymbol{k}}$ is the Fourier transform. The Fourier component of the velocity field is

$$\boldsymbol{V}(\boldsymbol{k}) = \mathrm{i}\boldsymbol{k}\phi_{\boldsymbol{k}}. \tag{2.7}$$

We generate the Fourier component of the scalar potential $\phi_{\boldsymbol{k}}$ as a random Gaussian number with a prescribed power spectrum, $P(\boldsymbol{k}) = k^2 \left\langle |\phi_{\boldsymbol{k}}|^2 \right\rangle$. Finally, we derive the velocity field in real space by performing the inverse transform of $\boldsymbol{V}(\boldsymbol{k})$.

2.2.4 Numerical Calculation of the Angular Momentum

Since Inutsuka (2001) has shown that the core mass function can be described by Press-Schechter formalism (Press & Schechter, 1974), we use the Press-Schechter formalism to derive the core mass and angular momentum of cores. In the Press-Schechter formalism, the length scale is defined as the collapsed region which would form a core in the future and the mass scale is defined as the mass in that collapsed region. Therefore, for a uniform filament, the mass is determined by the length (Figure 2.2). By assuming conservation of the angular momentum in that region, we adopt the angular momentum in that region as the angular momentum of the future core.

Following this concept, first, we choose an arbitrary length, $L_{\rm core}$, at a random position along the longitudinal direction of the filament. Next, we calculate the angular momentum in that region as follows:

$$\boldsymbol{J}(M) = \rho \int \boldsymbol{x} \times \boldsymbol{v}\ d^3x, \tag{2.8}$$

where ρ is the density, $\boldsymbol{x}$ is the position vector. We repeat this procedure for 99 values of $L_{\rm core}$ between $\lambda_{\rm min}$ and $\lambda_{\rm max}$ to obtain $j - M$ relation. By using this method, we can study how the $j - M$ relation depends on the power spectrum of the velocity field.

In this work we examine four power spectrum models: a three-dimensional (3D) Kolmogorov power spectrum (Section 3.1), a log-normal power spectrum (Section 3.2), an anisotropic power spectrum (Section 3.3), and a one-dimensional (1D) Kolmogorov power spectrum (Section 3.4).

2.2.5 Analytical Solution for Isotropic Velocity Field

For an isotropic velocity field, we can analytically derive the angular momentum as follows.

Incompressible Velocity Field

The angular momentum in the region with a length scale $L_{\rm core} = M/{\rm M}_{\rm line,crit}$ is given by

$$\begin{aligned}\boldsymbol{J}(M) &= \rho \int \boldsymbol{x} \times \boldsymbol{v} d^3x \\ &= -\rho \sum_{\boldsymbol{k}} \boldsymbol{V}(\boldsymbol{k}) \times \int \boldsymbol{x} \exp(\mathrm{i}\boldsymbol{k}\cdot\boldsymbol{x}) \mathrm{d}^3\mathrm{x} \\ &= 2\mathrm{i}M \sum_{\boldsymbol{k}} \boldsymbol{V}(\boldsymbol{k}) \times \boldsymbol{R}(\boldsymbol{k}; L_{\rm core}).\end{aligned} \tag{2.9}$$

$\boldsymbol{R}(\boldsymbol{k}; L_{\rm core})$ is defined as

$$\boldsymbol{R}(\boldsymbol{k}; L_{\rm core}) \equiv \frac{\mathrm{i}}{2\pi R_{\rm fil}^2 L_{\rm core}} \int \boldsymbol{x} \exp(\mathrm{i}\boldsymbol{k}\cdot\boldsymbol{x}) \mathrm{d}^3\mathrm{x}. \tag{2.10}$$

$\boldsymbol{R}(\boldsymbol{k}; L_{\rm core})$ corresponds to the Fourier transform of the position vector $\boldsymbol{x}$. The detailed derivation of $\boldsymbol{R}(\boldsymbol{k}; L_{\rm core})$ is shown in Appendix A. Using Equation 2.9, we can derive the specific angular momentum

$$\begin{aligned} j(M) &= \frac{\sqrt{\langle J(M)^2 \rangle}}{M} \\ &= \sqrt{2 \sum_{\boldsymbol{k}} P(k) \left[\{\boldsymbol{R}(\boldsymbol{k})\}^2 + \frac{\{\boldsymbol{k} \cdot \boldsymbol{R}(\boldsymbol{k})\}^2}{k^2} \right]}, \end{aligned} \tag{2.11}$$

where $P(k)$ is the power spectrum as introduced in Section 2.3. j^2 is the sum of the product of the square of the Fourier components of the velocity ($P(k) = \langle |\boldsymbol{V}(\boldsymbol{k})|^2 \rangle$) and the position ($\boldsymbol{R}(\boldsymbol{k}; L_{\rm core})^2$).

Compressible Velocity Field

In the case of the potential velocity field, we can also derive an analytical expression for the specific angular momentum similar to Equation 2.11. The specific angular momentum is

$$\begin{aligned} j(M) &= \frac{\sqrt{\langle J(M)^2 \rangle}}{M} \\ &= 2 \sqrt{\sum_{\boldsymbol{k}} P_\phi(k) [\boldsymbol{k}^2 \{\boldsymbol{R}(\boldsymbol{k})\}^2 - \{\boldsymbol{k} \cdot \boldsymbol{R}(\boldsymbol{k})\}^2]}, \end{aligned} \tag{2.12}$$

where P_ϕ is defined as

$$P_\phi(k) = \left\langle |\phi_{\boldsymbol{k}}|^2 \right\rangle . \tag{2.13}$$

2.3 Results

In this section, we examine four power spectrum models: three isotropic models (3D Kolmogorov power spectrum model in Section 3.1, log-normal power spectrum model in Section 3.2, and 1D Kolmogorov power spectrum model in Section 3.4) and one anisotropic power spectrum model in Section 3.3. We compare the $j - M$ relations derived from our four models over the mass range 0.48 $\mathrm{M}_\odot$ $< M <$ 51.2 $\mathrm{M}_\odot$ (cf., Section 2.1) with the observational results to discuss the origin of the observed angular momentum of cores.

2.3.1 3D Kolmogorov Power Spectrum Model

In this subsection, we adopt a 3D Kolmogorov power spectrum compatible with the observed Kolmogorov turbulent power spectrum of the ISM (Armstrong et al., 1995),

$$P(k) dk_x dk_y dk_z = A k^{-11/3} dk_x dk_y dk_z, \tag{2.14}$$

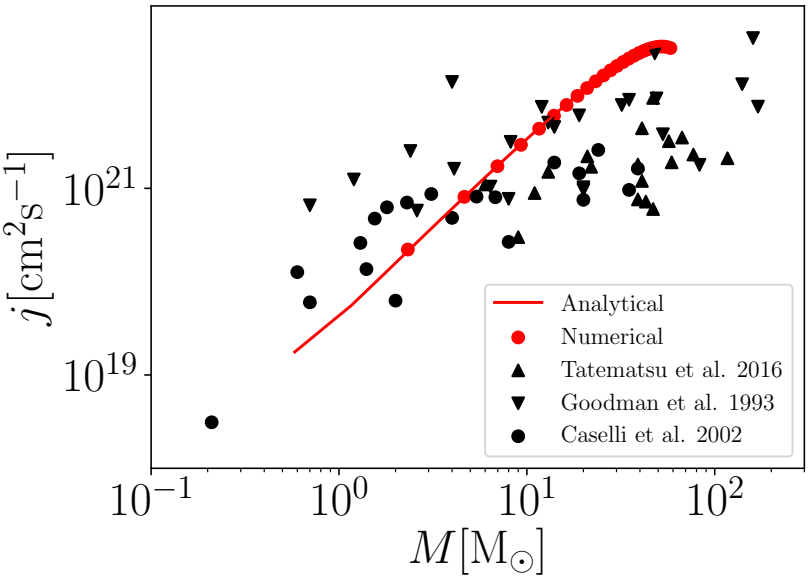

Figure 2.3: $j - M$ relation obtained from 3D Kolmogorov turbulence power spectrum model (Section 3.1). The red filled circles and the solid line represent the numerical and the analytical results, respectively. The observational data are the same as in Figure 2.1.

where $k = \sqrt{k_x^2 + k_y^2 + k_z^2}$. Note, however, that hereafter we consider only the discrete modes that are periodic in the domain $(-L_x/2 < x < L_x/2, -L_y/2 < y < L_y/2, -L_z/2 < z < L_z/2)$ as in Equation 2.2. If we define the major axis of the filament as the z-axis ($x = y = 0$), we can define the velocity along the filament as follows,

$$\boldsymbol{v}_{\rm 1D}(z) = \frac{1}{M_{\rm line}} \int \int^{\sqrt{x^2+y^2}<R_{\rm fil}} \rho \boldsymbol{v}\ dxdy, \tag{2.15}$$

where $R_{\rm fil}$ is the radius of the filament. If we use $\boldsymbol{v}$ following to the power spectrum Equation 2.14, the slope of the power spectrum of $\boldsymbol{v}_{\rm 1D}(z)$ is $-11/3$ (cf., Section 5). The coefficient A reflects the 3D velocity dispersion, $\sigma_{\rm 3D}$, along the filament crest. The observed velocity dispersion towards filaments with $\mathrm{M_{line}} \sim \mathrm{M_{line,crit}}$ is $c_s \lesssim \sigma_{\rm 1D} \lesssim 2c_s$ (Hacar & Tafalla, 2011; Arzoumanian et al., 2013; Hacar et al., 2016) with $\sigma_{\rm 1D} = \sigma_{\rm 3D}/\sqrt{3}$. Since $\sigma_{\rm 3D}$ and j are proportional to $\sqrt{A}$, setting $\sigma_{\rm 3D}$ between c_s and $2c_s$ will change the result by a factor of only 2. We therefore choose $\sigma_{\rm 3D} = c_s$ as our fiducial value for the models and for the figures shown in this paper. In Section 4 we compare the results obtained with $\sigma_{\rm 3D} = c_{\rm s}$ and $\sigma_{\rm 3D} = 2c_{\rm s}$.

Figure 2.3 shows the $j - M$ relation obtained from the 3D Kolmogorov power spectrum model. The red filled circles and the solid line represent the numerical and the analytical results, respectively. The analytical result is calculated using Equation 2.11. Since, as can be seen in Figure 2.3, the analytical result (Equation

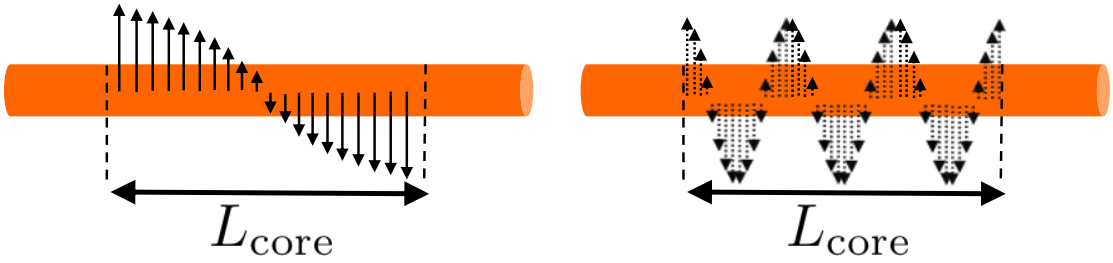

Figure 2.4: Example of the superposition of different fluctuating modes along the filament. In the region with a length $L_{\rm core}$ the wave represented by the solid line arrows is the most important for the angular momentum (left) and the wave represented by the dashed line arrows mostly cancels and hence does not significantly contribute to the angular momentum of this region (right).

2.11) agrees with the numerical result, in the following Section 3.2 and Section 3.4 we will continue the discussion using the analytical calculation.

Figure 2.3 suggests that for the 3D Kolmogorov power spectrum, the observed $j - M$ relation is not reproduced. This result can be understood as follows. The velocity fluctuations along a filament correspond to a superposition of different modes with different wavenumbers. The wavenumber which is the most important for the angular momentum in the region with a length $L_{\rm core}$ is $k = 2\pi/(2L_{\rm core})$. The modes with large wavenumbers do not contribute to the integration of the right hand side of Equation 2.8 since these modes cancel out (Figure 2.4). Hence the small angular momentum derived with this model for low mass regions is due to the small amount of energy in small wavelength (large wavenumber) regions. The large angular momentum derived for the high mass region is also inconsistent with the observations (Figure 2.3). In the following section we address this problem.

2.3.2 Log-normal Power Spectrum Model

To analyze the problem mentioned in the previous subsection, one may increase the power in large wavenumber region compared to the 3D Kolmogorov power spectrum. To do so, in this subsection, we adopt a log-normal energy spectrum,

$$E(k) = A_G \exp\left[-\frac{\{\log(k) - \log(k_{\rm peak})\}^2}{2\sigma_G^2}\right], \tag{2.16}$$

where A_G, σ_G, and $k_{\rm peak}$ are the amplitude, the dispersion, and the peak of the log-normal function, respectively. The energy spectrum is defined as follows,

$$\frac{\langle|\boldsymbol{v}|^2\rangle}{2} = \sum_{\boldsymbol{k}} E(k). \tag{2.17}$$

The power spectrum is described as

$$P(k)dk_x dk_y dk_z = \frac{A_G}{2\pi k^2} \exp\left[-\frac{\{\log(k) - \log(k_{\rm peak})\}^2}{2\sigma_G^2}\right] dk_x dk_y dk_z. \tag{2.18}$$

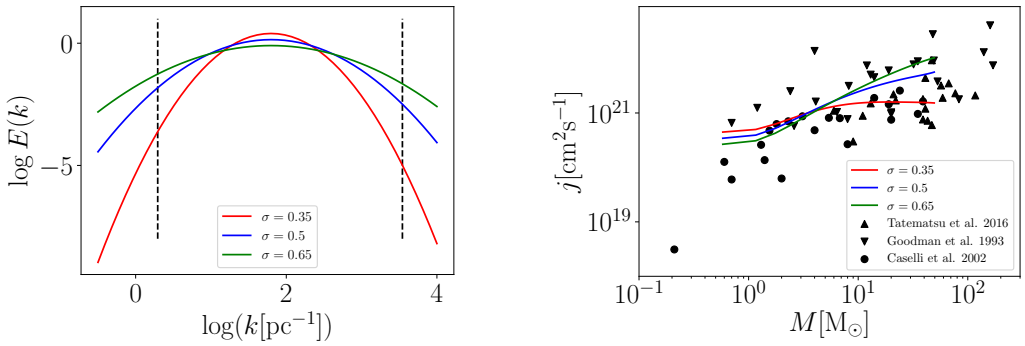

Figure 2.5: (left) The horizontal axis is the wavenumber and the vertical axis is the energy spectrum. The region between the two black dashed lines represents the range of wavenumber that we used. (right) $j - M$ relation derived from the log-normal power spectrum model with fixed value, $k_{\rm peak} = 2\pi/(0.1{\rm pc})$. The red, blue, and green solid lines correspond to $\sigma_G = 0.35, 0.5$, and 0.65, respectively. The observational data are the same as in Figure 2.1.

As in Section 3.1, we consider only the discrete modes that are periodic in the domain.

Log-normal Power Spectrum Model for Incompressible Velocity Field

We regard $k_{\rm peak}$ and σ_G in Equation 2.18 as parameters to study how $j - M$ relation depends on the shape of the energy spectrum, and choose A_G to satisfy the constraint $\sigma_{\rm 3D} = c_s$. Figure 2.5 shows the $j-M$ relation derived from Equation 2.11 and Equation 2.18. Here we use $k_{\rm peak} = 2\pi/(0.1$ pc) for a filament width of 0.1 pc, and regard only σ_G as a variable parameter ($\sigma_G = 0.35$, 0.5, and 0.65). Figure 2.6 shows the $j - M$ relation for fixed $\sigma_G = 0.5$ and varying $\lambda_{\rm peak} = 1.0$, 0.5, 0.1, and 0.05 pc, respectively with $\lambda_{\rm peak}$ defined as $k_{\rm peak} = 2\pi/\lambda_{\rm peak}$. In this model the power of the wave with wavelength $\lambda_{\rm peak}$ is the largest. Since, in our calculation, the waves along x- or y-axis with wavelength larger than 0.1 pc are truncated, their component along the z-axis has the largest power in the models with $\lambda_{\rm peak} > 0.1$ pc. The results shown in Figure 2.5 and Figure 2.6 indicate that the power spectrum described by Equation 2.18 reproduces the observed trend of the angular momentum of cores. Figure 2.7 shows how the index depends on the two parameters $k_{\rm peak}$ and σ_G. Since the $j - M$ relations derived from the log-normal model are not straight lines, we apply the least square fitting method to the derived $j - M$ curves in the mass range, $1 - 10$ M$_\odot$ to derive the power law index of each model curve. While the comparison with observations suggests that the index is approximately $0.5 - 0.9$, future observations are needed to better constrain this index value. Once the $j - M$ relation for the angular momentum distribution is accurately determined by observations, we would be able to give, using our model, a more accurate description of the velocity fluctuations along the parent filament.

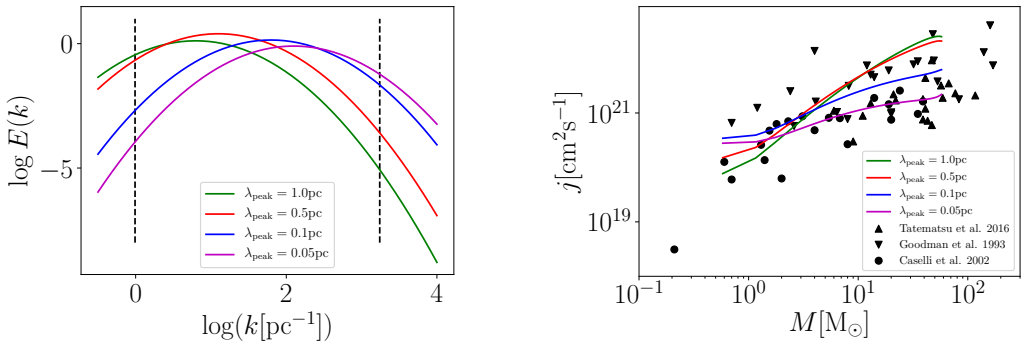

Figure 2.6: (left) Same as Figure 2.5 for fixed $\sigma_G = 0.5$ and varying $\lambda_{\rm peak}$. (right) $j - M$ relation derived from the log-normal power spectrum model with fixed value $\sigma_G = 0.5$. The green, red, blue, and magenta solid lines correspond to $\lambda_{\rm peak} = 1.0, 0.5, 0.1$, and 0.05 pc. $\lambda_{\rm peak}$ is defined as $k_{\rm peak} = 2\pi/\lambda_{\rm peak}$. The observational data are the same as in Figure 2.1.

Log-normal Power Spectrum Model for Compressible Velocity Field

We also calculate the angular momentum in the case of compressible velocity field using Equation 2.12 for $\sigma_{\rm 3D} = c_s$. Figure 2.8 shows the $j-M$ relation for a potential velocity field using the log-normal power spectrum model described by Equation 2.18, for $\sigma_G = 0.5$ and $\lambda_{\rm peak} = 0.1$ pc. As shown in Figure 2.8, the compressible velocity field hardly contributes to the angular momentum of cores. This result suggests that the solenoidal component of the velocity field in filaments mainly accounts for the origin of the angular momentum of the molecular cloud cores. Therefore, hereafter we consider only the incompressible velocity component.

2.3.3 Anisotropic Power Spectrum Model

As mentioned in Section 3.2.1, with an isotropic power spectrum (Equation 2.16), we can reproduce the properties of the angular momentum of cores with the available observed data points. However, such an increase in the power of velocity or density fluctuations in larger wavenumber (small scales) has not been observationally reported, possibly because of the limited spatial resolution (Roy et al., 2015). In contrast, for the density distribution in the larger wavelength range (>0.02 pc), relatively simple Kolmogorov-like power laws are observed along filaments and in the diffuse ISM (Roy et al., 2015; Miville-Deschênes et al., 2010; Roy et al., 2019). According to the recently proposed scenario of filamentary structure formation where filaments may be formed by large scale compressions (e.g., Inoue & Inutsuka, 2012; Inutsuka et al., 2015; Inoue et al., 2018; Arzoumanian et al., 2018), it is expected that the waves along the x- and y-axis (transverse direction) have more energy than those along z-axis (longitudinal direction) as a result of energy shift from large to small scales due to the compression. In addition, transverse velocity gradients are reported by recent observations in several molecular filaments

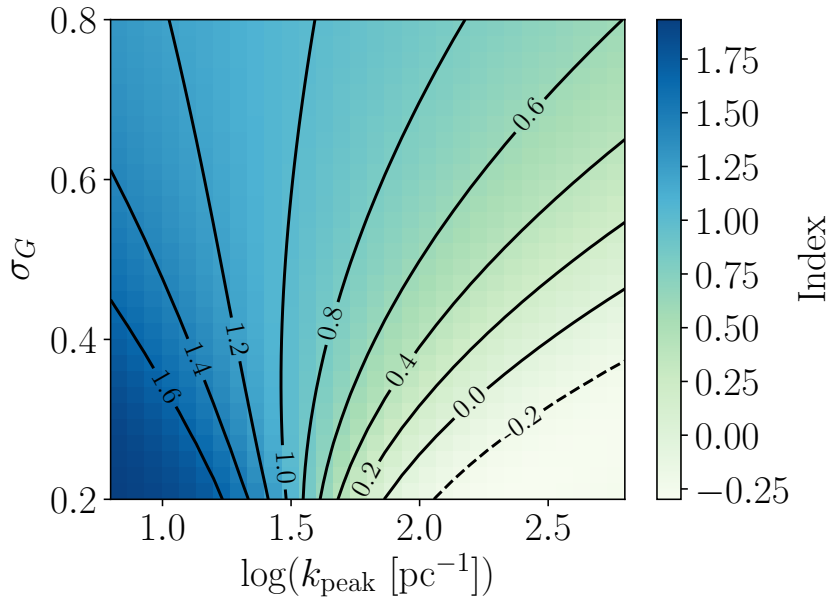

Figure 2.7: Dependence of the index of the $j - M$ relation slope on the two parameters, σ_G and $k_{\rm peak}$. The horizontal axis is $k_{\rm peak}$ and the vertical axis is σ_G. The indices are derived by applying the least square fitting method to the $j - M$ relation in the mass range $1 - 10$ $M_\odot$.

(e.g., Fernández-López et al., 2014; Dhabal et al., 2018). Hence it is interesting to examine whether anisotropic power spectrum reproduces the observed $j - M$ relation. In this paper, for simplicity, we adopt the following simple Kolmogorov-like anisotropic power spectrum

$$P(\boldsymbol{k})dk_x dk_y dk_z = A(A_r k_r^2 + k_z^2)^{-11/6} dk_x dk_y dk_z, \tag{2.19}$$

where $k_r = \sqrt{k_x^2 + k_y^2}$, and A_r corresponds to the degree of anisotropy. As in Section 3.1 and 3.2, we consider only the discrete modes that are periodic in the domain. Figure 2.9 shows the color contour for isotropic and anisotropic power spectra. Figure 2.10 shows the result from the anisotropic power spectrum with $A_r = 0.01$ as shown in Figure 2.9 (right) with more energy in the transverse direction than in the longitudinal direction. We find that such an anisotropic power spectrum reproduces the observed properties of angular momentum of cores.

2.3.4 1D Kolmogorov Power Spectrum Model

In this subsection, we examine the 1D Kolmogorov power spectrum model. The power spectrum is described as

$$P(k)dk_x dk_y dk_z = Ak^{-5/3} dk_x dk_y dk_z, \tag{2.20}$$

where $k = \sqrt{k_x^2 + k_y^2 + k_z^2}$. We consider only the discrete modes that are periodic in the domain again. We can calculate the velocity along the filament using Equation

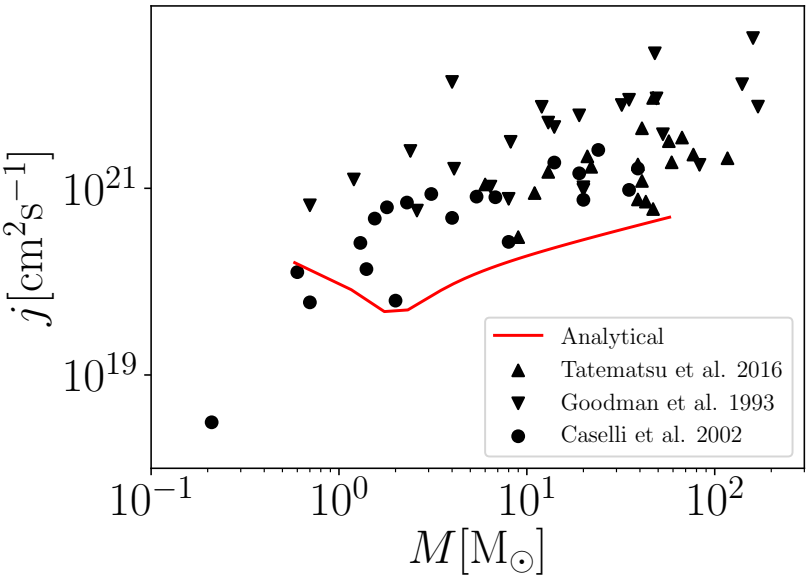

Figure 2.8: $j-M$ relation for a compressible velocity field. The red solid line is the result obtained from the expression for the potential field shown in Equation 2.12, and the log-normal power spectrum Equation 2.18 with $\sigma_G = 0.5$ and $\lambda_{\rm peak} = 0.1$ pc. The observational data are the same as in Figure 2.1.

2.15. If we use $\boldsymbol{v}$ following the power spectrum Equation 2.20, the slope of the power spectrum of $\boldsymbol{v}_{\rm 1D}(z)$ is $-5/3$ (cf., Section 5). The coefficient A is chosen to satisfy the constraint $\sigma_{\rm 3D} = c_s$. Since the slope of the 1D Kolmogorov power spectrum is shallower than that of the 3D Kolmogorov power spectrum, the power in large wavenumber region is larger than for the 3D Kolmogorov power spectrum. Figure 2.11 shows the $j - M$ relation derived from the 1D Kolmogorov power spectrum. We find that such a 1D Kolmogorov power spectrum also reproduces the observed properties of angular momentum of cores.

We think that the power spectrum of the filament should be determined in the formation process of the filament and the resultant power spectrum should be related to the 3D power spectrum in the parent molecular cloud. We discuss possible implications from our results in the formation of filamentary molecular clouds in Section 5.

2.4 Comparison of the Derived Power Spectrum Models

In this section, we attempt to evaluate the appropriateness of the different models presented above. To do so, we calculate $\sigma^2_{\rm error}$, the dispersion of the observational data points relative to the analytical $j-M$ relations for the different models. The

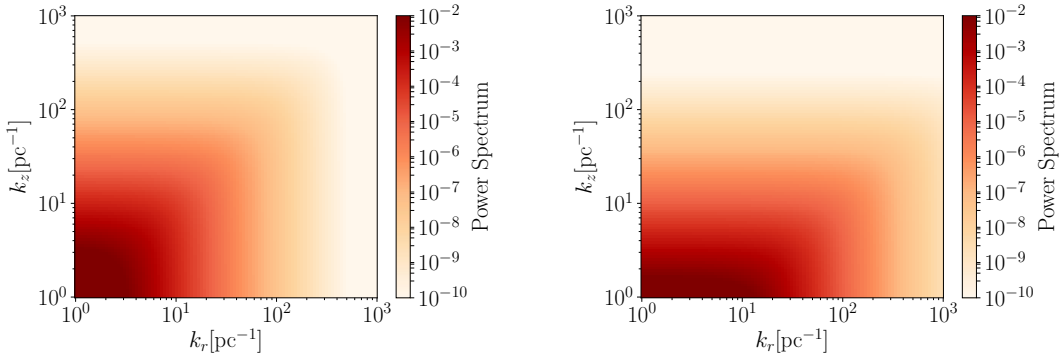

Figure 2.9: Color contour of power spectrum. Isotropic 3D Kolmogorov power spectrum (left) and anisotropic model derived from Equation 2.19 with $A_r = 0.01$ (right).

Table 2.1: Relative appropriateness of the models. The values in Table 2.1 are the dispersions $\sigma^2_{\rm error}$ of the observational points relative to the analytical solution in $j - M$ diagram calculated using Equation 2.21 and normalized by $\sigma^2_{\rm error}$ of the 3D Kolmogorov model (cf., Section 4).

	3D Kolmogorov	1D Kolmogorov	Anisotropy	Log-normal ($\sigma_{\rm G} = 0.65$, $\lambda_{\rm peak} = 0.1$)	Compressible
$\sigma_{\rm 3D} = c_{\rm s}$	1	0.40	0.39	0.43	1.32
$\sigma_{\rm 3D} = 2c_{\rm s}$	1	0.39	0.48	0.57	0.53

dispersion of a model is defined as follows,

$$\sigma^2_{\rm error} = \frac{1}{N_{\rm data}} \sum_{i=1}^{N_{\rm data}} (\log(j(M_i)) - \log(j_{{\rm obs},i}))^2, \tag{2.21}$$

where i, $N_{\rm data}$, $j(M_i)$, and $j_{{\rm obs},i}$ are each data point, the total number of data points, the analytical solution described by Equation 2.11, and the observational points, respectively. Table 2.1 shows the accuracy of the models normalized by that of the 3D Kolmogorov model. We give values of $\sigma^2_{\rm error}$ for the different models calculated with a velocity dispersion $\sigma_{\rm 3D}$ equal to $c_{\rm s}$ and $2c_{\rm s}$ corresponding to the observed range (cf. Section 3.1). Table 2.1 shows that our conclusions are not affected by the choice of $\sigma_{\rm 3D}$ within the observed range. Note that the evaluation of appropriateness is tentative and future observations may give us more information to better constrain the models.

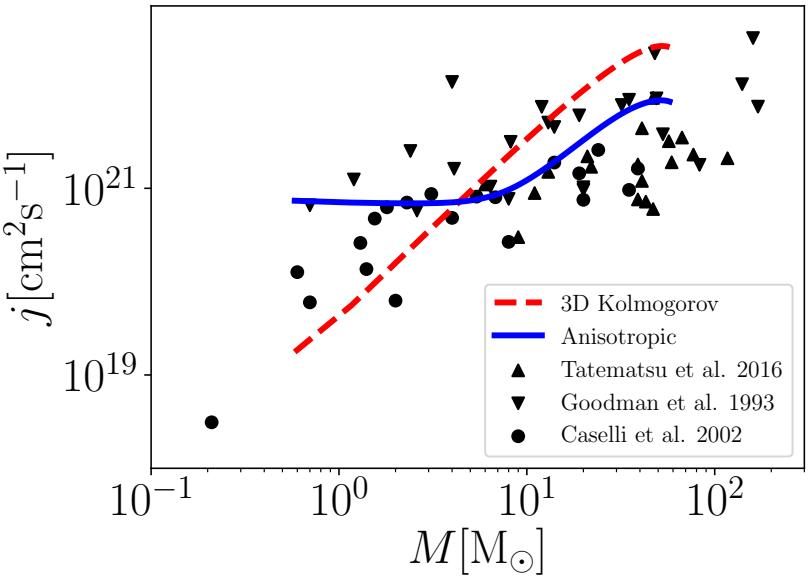

Figure 2.10: $j - M$ relation for anisotropic power spectrum. The red dashed line and blue solid line are isotropic 3D Kolmogorov power spectrum (same as Figure 2.3) and anisotropic power spectrum model derived using Equation 2.19, $A_r = 0.01$ respectively. The observational data are the same as in Figure 2.1.

2.5 Discussion

In the following, we attempt to provide a link between the velocity fluctuations along a star-forming filament and that of its surrounding molecular cloud. In particular we suggest that the 1D Kolmogorov velocity power spectrum along the filament described in Section 3.4 is linked to the 3D Kolmogorov velocity power spectrum of the parent cloud.

Recent observational results show that a small fraction of the total mass of molecular clouds ($< 20\%$) is in the form of dense gas, for column densities $\gtrsim 7 \times 10^{21}$ cm^{-2}, and that a large fraction of this dense gas is in the form of critical/supercritical filaments ($\sim 80\%$ on average, André et al., 2014; Arzoumanian et al., 2019, see also Torii et al. 2018). This column density value has been observationally identified as the threshold above which the star formation activity is significantly enhanced (e.g., Heiderman et al., 2010; Lada et al., 2010, 2012; Könyves et al., 2015). This star formation threshold is now understood as being equivalent to the line mass of 0.1 pc-wide filaments that is of the order of the critical value ($\mathrm{M_{line,crit}}$) for gravitational fragmentation (e.g., Arzoumanian et al., 2013; André et al., 2014).

If we define the major axis of the filament as the z-axis ($x = y = 0$), we can

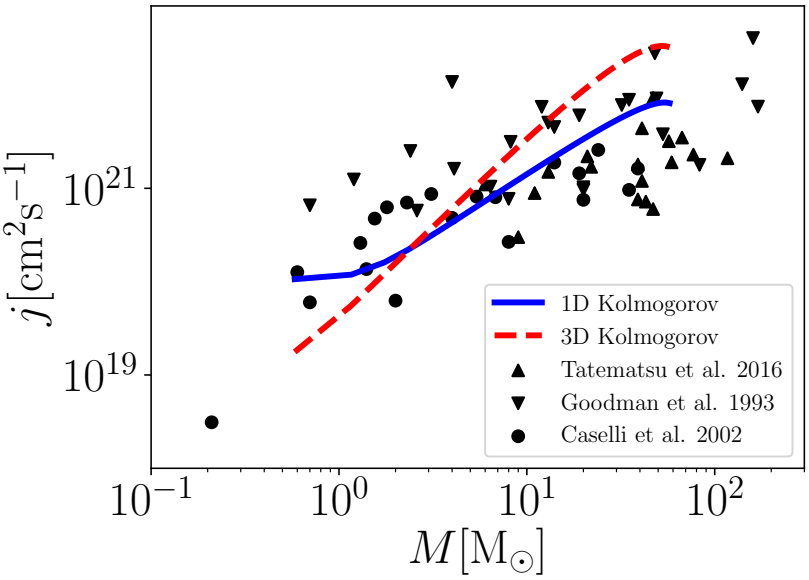

Figure 2.11: $j - M$ relation for 1D Kolmogorov power spectrum. The red dashed line and blue solid line are 3D Kolmogorov power spectrum (same as Figure 2.3) and 1D Kolmogorov power spectrum model derived using Equation 2.20, respectively. The observational data are the same as in Figure 2.1.

calculate the line mass of the filament as follows,

$$M_{\rm line}(z) = \int\int^{\sqrt{x^2+y^2}<R_{\rm fil}} \rho \; dxdy. \tag{2.22}$$

Likewise the velocity $\boldsymbol{v}_{\rm fil}$ along the filament is defined as follows,

$$\boldsymbol{v}_{\rm fil}(z) = \frac{1}{M_{\rm line}} \int\int^{\sqrt{x^2+y^2}<R_{\rm fil}} \rho \boldsymbol{v} \; dxdy. \tag{2.23}$$

The 1D Fourier component of the velocity field along the filament z-axis is

$$\begin{aligned} \widetilde{\boldsymbol{v}}(k_z) &= \frac{1}{L_z} \int_{-L_z/2}^{L_z/2} \boldsymbol{v}_{\rm fil}(z) \exp(-{\rm ik_z z}){\rm dz} \\ &\sim \frac{1}{L_z} \int_{-L_z/2}^{L_z/2} \boldsymbol{v}(0,0,z) \exp(-{\rm ik_z z}){\rm dz}, \end{aligned} \tag{2.24}$$

where, L_z is the length of the z direction of the molecular cloud and $\widetilde{\boldsymbol{v}}$ is the 1D Fourier component of the velocity field. In the second step of Equation 2.24, we take the limit $R_{\rm fil} \to 0$, because the mass of a critical/supercritical filament (i.e., the mass of dense gas) is much smaller than the total mass of the parental molecular cloud as suggested by observations (see above). The limit of $\boldsymbol{v}_{\rm fil}(z)$ as $R_{\rm fil}$ approaches to 0 is $\boldsymbol{v}(0,0,z)$. Note that while the velocity field is integrated

with x and y in Equation 2.15, in Equation 2.24 the velocity field is not integrated because of the approximation $\boldsymbol{v}_{\rm fil}(z) \sim \boldsymbol{v}(0,0,z)$. The 1D power spectrum $P_{\widetilde{\boldsymbol{v}}}$ of $\widetilde{\boldsymbol{v}}$ is defined as

$$P_{\widetilde{\boldsymbol{v}}}(k_z) \;\; = \langle |\widetilde{\boldsymbol{v}}(k_z)|^2 \rangle \, . \tag{2.25}$$

Using Equation 4.4, Equation 2.24, and Equation 2.25, the 1D velocity power spectrum can be rewritten as

$$P_{\widetilde{\boldsymbol{v}}}(k_z) = \sum_{k'_x} \sum_{k'_y} P(k'_x, k'_y, k_z). \tag{2.26}$$

The derivation of Equation 2.26 is given in Appendix B. The left hand side of Equation 2.26 is the 1D power spectrum $P_{\widetilde{\boldsymbol{v}}}(k_z)$ of the velocity along the filament, which is equal to the integration of the 3D Kolmogorov-like power spectrum $P(k'_x, k'_y, k_z)$ with respect to k'_x and k'_y. This integration can be done as follows,

$$\begin{aligned}
P_{\widetilde{\boldsymbol{v}}}(k_z) &= \sum_{k'_x} \sum_{k'_y} P(k'_x, k'_y, k_z) \\
&\sim \frac{L_x L_y}{(2\pi)^2} A \int_0^{k_{\rm max}} \int_0^{k_{\rm max}} (k_x'^2 + k_y'^2 + k_z^2)^{-11/6} \, dk'_x dk'_y \\
&\sim \frac{L_x L_y}{(2\pi)^2} A \int_0^{\infty} \int_0^{\infty} (k_x'^2 + k_y'^2 + k_z^2)^{-11/6} \, dk'_x dk'_y \\
&= \frac{L_x L_y}{(2\pi)^2} A \int_0^{\infty} (k_r'^2 + k_z^2)^{-11/6} \, \frac{\pi}{2} k'_r dk'_r \\
&\propto k_z^{-5/3},
\end{aligned} \tag{2.27}$$

where L_x and L_y are the length of x and y directions of the molecular cloud. $k_{\rm max}$ is the maximum wavenumber, which might correspond to an energy dissipation scale. The approximation that the summation can be replaced by an integral up to $+\infty$ is valid only for $k_z < k_{\rm max}$. Here we assume that the largest wavenumber is the same along all the three (x, y, and z) directions, i.e., isotropic at small scales. Therefore, we can use the approximation that the summation can be replaced by an integral up to $+\infty$. This result shows that the 1D approximation in Equation 2.24 leads to the 1D Kolmogorov power spectrum along the filament. While the width of the filament considered in Section 3.1 is also small (0.1 pc) compared to the size of the cloud ($\sim$ 10 pc), the resulting slope of the power spectrum of $\boldsymbol{v}_{\rm 1D}(z)$ is $-11/3$, very different from the slope $-5/3$ found here. This is mainly due to the periodic boundary condition for the functional dependence of the modes in the x- and y-directions in Section 3.1: i.e., the modes in the x- and y-directions cancels in Equation 2.15, these modes are not contributing to the power spectrum of $\boldsymbol{v}_{\rm 1D}(k_z)$, unlike in Equation 2.26. In this section, since we consider the velocity field that is extended in the parent cloud outside the filament, here the modes are not anymore periodic within the filament.

We can thus link the observed 3D power spectrum of the parent cloud to the 1D velocity power spectrum along the filament. A filament with $\rm M_{line} \sim M_{line,crit}$

and velocity fluctuations along its crest characterized by the 1D Kolmogorov power spectrum with a slope of $-5/3$ would fragment into a series of cores presenting the observed distribution of angular momentum as shown in Section 3.4.

In addition to providing an origin to the observed angular momentum of cores, we also emphasize that these velocity fluctuations along star-forming filaments with a power spectrum of $P(k) \propto k^{-5/3}$ may also be key in understanding the origin of the shape of the core mass function (cf., Inutsuka, 2001; Roy et al., 2015; Lee et al., 2017). Note also that the 1D approximation of star-forming filaments might be justified by the observed small mass fraction of the dense gas in the form of critical/supercritical filaments with respect to the total mass of the cloud. We suggest that this small mass fraction of dense gas may also provide a hint to the origin of the observed low star formation efficiency in molecular clouds.

2.6 Summary of this Chapter

In this chapter we provide a causal link between properties of filaments and cores. We suggest that the observed angular momentum distribution of cores as a function of core mass can be understood by the fragmentation of filaments having velocity fluctuations close to the sonic speed and anisotropic, log-normal, and 1D Kolmogorov power spectra. We demonstrate that the 3D Kolmogorov velocity and density power spectra observed at the scale of the cloud implies a 1D Kolmogorov velocity spectrum along a filament when the mass of this latter is a small fraction of the total mass in the cloud, consistent with recent observational results (André et al., 2014; Arzoumanian et al., 2019; Torii et al., 2019). The results presented in this paper reinforces the key role of filament fragmentation in our understanding of the star formation process and the observed properties of cores. Future systematic observations tracing the velocity structure of cores are needed to derive the kinematic properties of cores to better constrain our models and examine the relation between the properties of filaments and cores, to understand the origin of the angular momentum of molecular cloud cores, multiple systems, and protoplanetary disks.

Chapter 3

Power Spectrum Measured in Filament Formation Simulation

As shown in previous chapter, the sub (tran) sonic Kolmogorov turbulence in the filaments is large enough to give the angular momentum to the molecular cloud cores. Recent theoretical researches reveal that the filaments are created when a shock wave interacts with a molecular clouds with density fluctuations (Inoue & Fukui, 2013; Inoue et al., 2018; Abe et al., 2021). If this filament formation mechanism is correct, the velocity fluctuations in the filaments should follow Kolmogorov power spectrum. To study this scenario, in this chapter, we analyse the data obtained by using three-dimensional magnetohydrodynamic (MHD) simulation done by Inoue et al. (2018) and Abe et al. (2021).

3.1 Simulation Setup

The Setup of simulation is shown in Figure 3.1. The color represents the number density of hydrogen molecule. The black line is magnetic field, and their direction along the y direction at the initial state. The strength of magnetic field is 10μG. The mean density at the initial state is $n = 10^3 \mathrm{cm}^{-3}$. They put the density fluctuations in the molecular cloud at the initial state. They set the initial converging flow along the z-axis. The box size is 6 pc, and the number of cell is 512^3. They solve the MHD equations including self-gravity by using the SFUMATO code (Matsumoto, 2007). The equation of state is isothermal, and sound speed is $c_\mathrm{s} = 0.2\mathrm{km\ s}^{-1}$. The parameter used in this analysis is the velocity of converging flow. They adopt the periodic boundary condition along the x and y directions.

Since we also analyse the data from Inoue et al. (2018), we explain the setup of Inoue et al. (2018) below. Figure 3.2 displays the schematic figure of setup of Inoue et al. (2018) (their Figure 1). The color represents the column density. The small cloud with turbulence is swept by plain parallel shock wave. The domain size is 0.6 pc, and the initial density is $n = 10^4 \mathrm{cm}^{-3}$. The finest resolution of the simulation is 1.5×10^{-3} pc. The magnetic field is perpendicular to the collision direction, and the strength of magnetic field is 20μG. They also solve the MHD

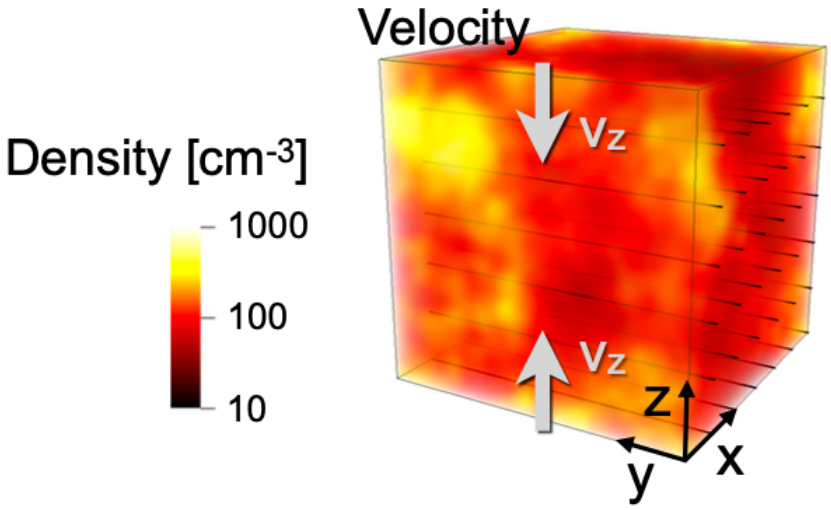

Figure 3.1: Schematic figure of simulation of Abe et al. (2021) (their Figure 1). The color represents the number density of hydrogen molecule. The black line is magnetic field, and their direction along the y direction at the initial state.

equations including self-gravity by using the SFUMATO code (Matsumoto, 2007). The equation of state is isothermal, and sound speed is $c_{\rm s} = 0.3{\rm km\ s^{-1}}$. They use the periodic boundary condition for the x and y directions, and free boundary condition for the z direction. The speed of converging flow is $5{\rm km\ s^{-1}}$ If the reader wants to know the setup of their calculations in more detail, please refer to their papers.

3.2 Analysis

Figure 3.3 displays the column density map at each time step using data from Abe et al. (2021). We use FilFinder algorithm (Koch & Rosolowsky, 2015) to identify the filament axis on the column density maps. The resultant filament axes are shown in Figure 3.4 as white lines. We calculate the power spectrum along these filament axes as follows.

The line mass of filament is defined as follows:

$$M_{\rm line}(z) = \int \rho dx dy. \tag{3.1}$$

The line mass fluctuations of filament is defined as follows:

$$\delta_{\rm line}(z) = \frac{M_{\rm line}(z) - {\rm M_{line,ave}}}{\rm M_{line,ave}}, \tag{3.2}$$

where

$${\rm M_{line,ave}} = \frac{\int_0^L M_{\rm line}(z) dz}{L}, \tag{3.3}$$

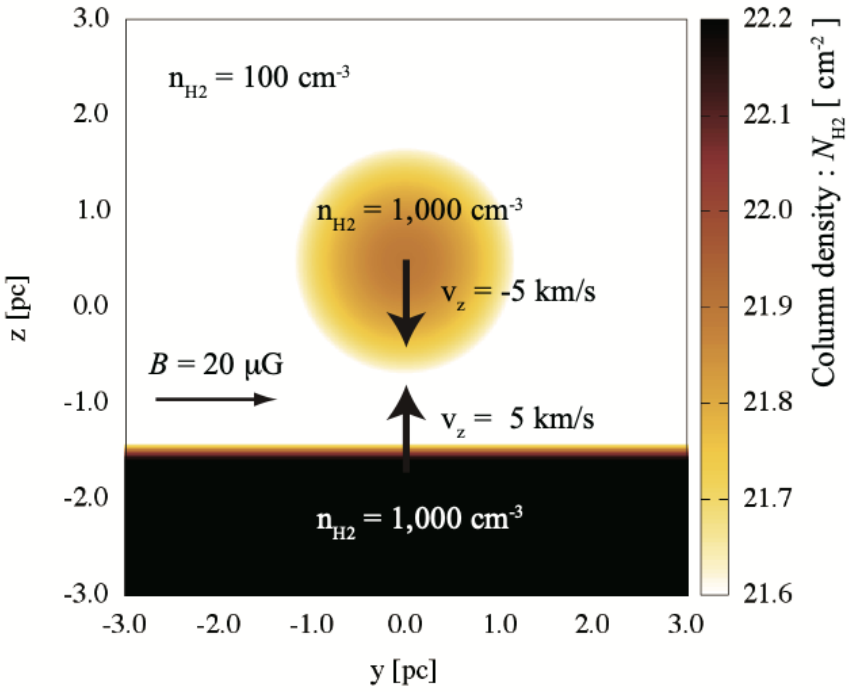

Figure 3.2: Schematic figure of setup of Inoue et al. (2018) (their Figure 1). The color represents the column density. The small cloud with turbulence is swept by plain parallel shock wave.

L is the filament axis. The Fourier transform is defined as follows:

$$\widetilde{\delta}_{\text{line}}(k_z) = \frac{1}{L}\int \delta_{\text{line}}(z)\exp^{-\mathrm{i}k_z z}\,dz. \tag{3.4}$$

The power spectrum is calculated as follows:

$$P_{\text{line}}(k_z) = \left\langle \left|\widetilde{\delta}_{\text{line}}(k_z)\right|^2 \right\rangle, \tag{3.5}$$

where $\langle\ \rangle$ represents the ensemble average. The velocity properties along the filaments are derived using the same way

$$V_{\text{line}}(z) = \int \rho v dx dy / M_{\text{line}} \tag{3.6}$$

$$\widetilde{V}_{\text{line}}(k_z) = \frac{1}{L}\int V_{\text{line}}(z)\exp^{-\mathrm{i}k_z z}\,dz \tag{3.7}$$

$$P_{\text{Vline}}(k_z) = \left\langle \left|\widetilde{V}_{\text{line}}(k_z)\right|^2 \right\rangle \tag{3.8}$$

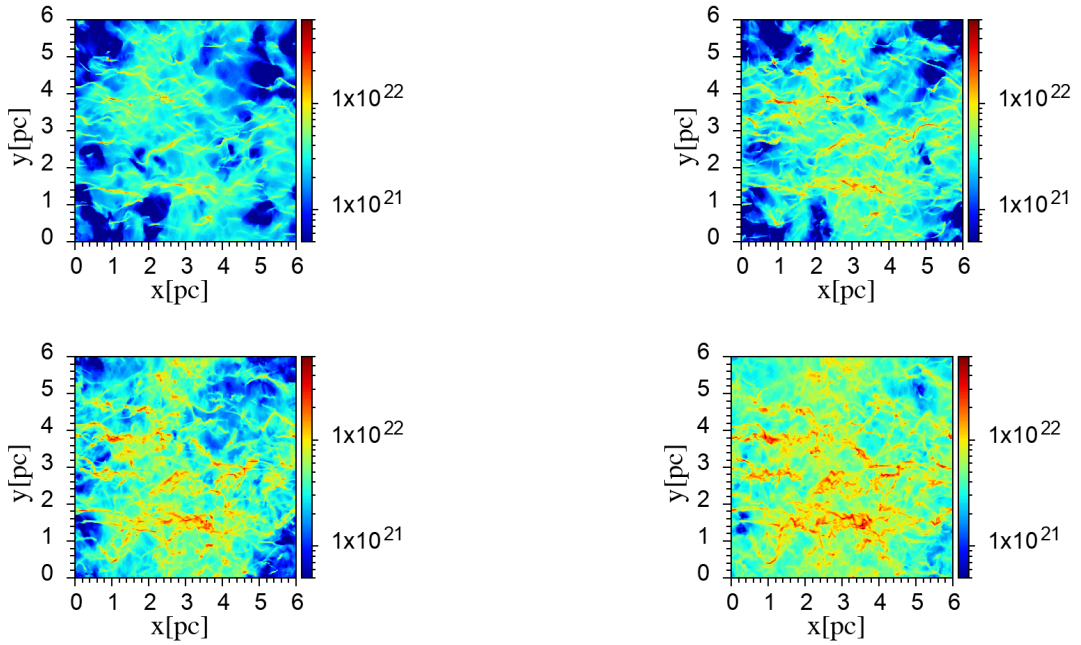

Figure 3.3: Column density map on $x-y$ plane. The color is the column density

The power spectrum of column density is derived as follows.

$$\widetilde{\Sigma}\left(k_x, k_y\right) = \frac{1}{L^2}\int \Sigma(x,y)\exp^{-\mathrm{i}(k_x x + k_y y)}\, dxdy, \tag{3.9}$$

$$P_\Sigma\left(k_x, k_y\right) = \left\langle \left|\widetilde{\Sigma}\left(k_x, k_y\right)\right|^2 \right\rangle. \tag{3.10}$$

3.3 Results

The left and right panel of Figure 3.5 are the examples of power spectrum of velocity and line mass fluctuations. The blue dots result from analysis explained in previous section, and the red lines are fitting results. We did this analysis all filament found in simulation of Abe et al. (2021), and the statistical results shown in Figure 3.6 and Figure 3.7. Figure 3.6 and Figure 3.7 are histograms of slope index of line mass and velocity fluctuations, respectively. The top left, top right, bottom left, and bottom right panels are the results at 0.3, 0.4, 0.5, and 0.6 Myr, respectively. In Figure 3.6 and Figure 3.7, the peaks of histogram are located around $-2 \lesssim \alpha \lesssim -1.5$. This result indicate that the measured power spectrum slope in Abe et al. (2021) is compatible to Kolmogorov turbulence ($\alpha = -5/3$).

We also show the results from Inoue et al. (2018). In Inoue et al. (2018), the filament formed in their simulation is more massive and longer than that of Abe et al. (2021). The line mass reaches $\sim$ 200 $\mathrm{M_\odot pc^{-1}}$ at the final state of their simulation. The column density is shown in the left panel of Figure 3.8. The

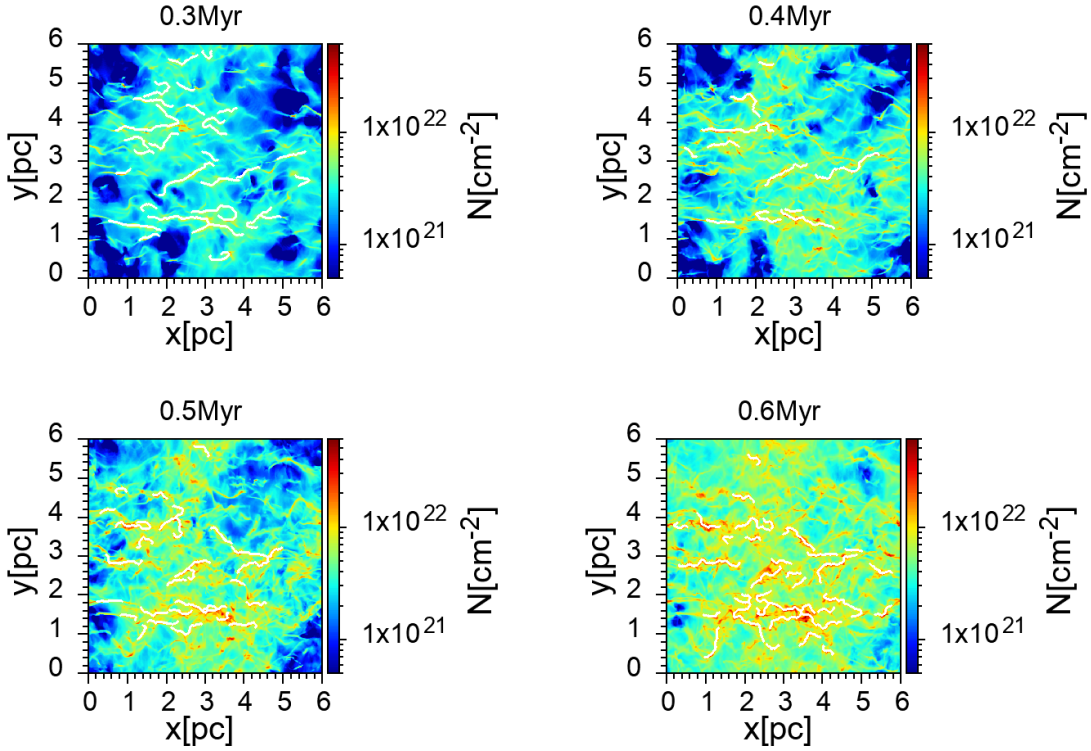

Figure 3.4: Same as Figure 3.3, but the white lines represent the filament axis.

black line is the filament axis identified by using FilFinder. The right panel of Figure 3.8 is the power spectrum of column density. The red dots are resultant power spectrum derived from Equation 3.10, and the blue solid line is the fitting line whose slope index is -2.4 ± 0.6. This slope index is also compatible with Kolmogorov slope ($-8/3$). Moreover, the power spectrum of line mass fluctuations has slope index -1.9 ± 0.5, and this is also compatible with Kolmogorov slope ($-5/3$). This result suggest that the Kolmogorov turbulence is realized even in the massive filamentary molecular cloud.

3.4 Summary and Discussion

In previous section, we analysed the power spectrum along the filaments formed in the filament formation simulation. As a result, the derived power spectra are compatible with Kolmogorov turbulence. This result indicates that the model presented in Chapter 2 is consistent with the results in filament formation scenario. Therefore, we conclude that the filament formation mechanism proposed in Inoue et al. (2018) can explain the origin of the angular momentum of molecular cloud cores.

The histograms shown in previous section have peaks around Kolmogorov-like slope, but they have dispersion of distribution in some degree. The origin of some filaments with shallower slope might be attributed to the growth of the shorter wavelength due to the gravitational instability. When the filament become mas-

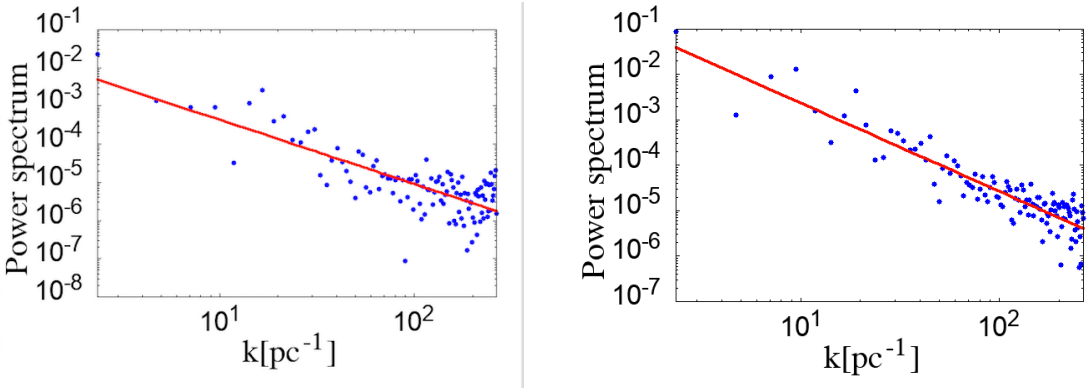

Figure 3.5: Examples of power spectrum of velocity and line mass fluctuations. The blue dots result from analysis explained in previous section, and the red lines are fitting results.

sive enough, the gravity dominates the pressure force, and the filaments begin to fragment to cores. If the collapse (fragmentation) continues infinitely, the central density is divergent, and this is described by delta condition. While, in reality, the collapse is halted when the equation of state becomes stiff and the isothermal approximation is violated, the power spectrum become shallow due to the gravitational instability. On the other hand, the filament with steep slope might be due to the cancellation of waves with short wavelength.

In this analysis we studied the power spectra only along the filament axis. An anisotropy of velocity field in filaments affects the properties of angular momentum (Chapter 2), especially the direction of rotation axis. Therefore, to investigate the anisotropy of velocity field is very important work to reveal the properties of angular momentum of cores in more detail, but at present the resolution of simulation is limited, for example, the resolution of Abe et al. (2021) is ~ 0.02 pc (c.f. filament width ~ 0.1 pc). Hence, we reach the conclusion that the isotropic Kolmogorov turbulence is the simplest and most reliable model at present to explain the origin for the angular momentum of molecular cloud cores.

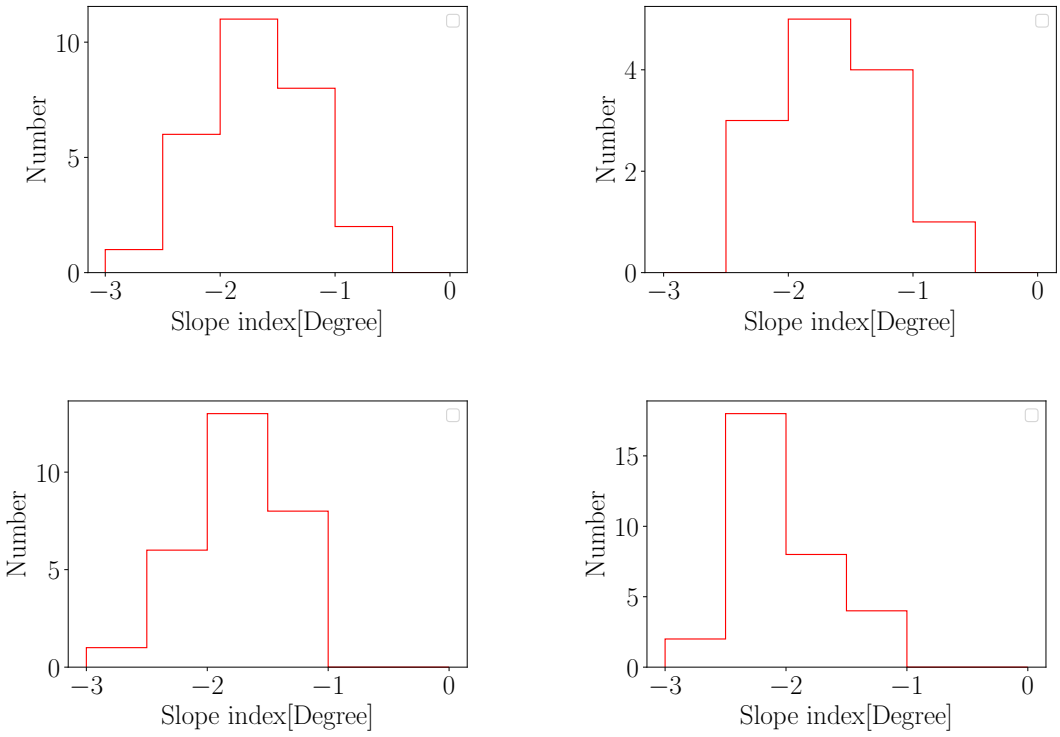

Figure 3.6: Histograms of slope index of line mass fluctuations, respectively. The top left, top right, bottom left, and bottom right panels are the results at 0.3, 0.4, 0.5, and 0.6 Myr, respectively.

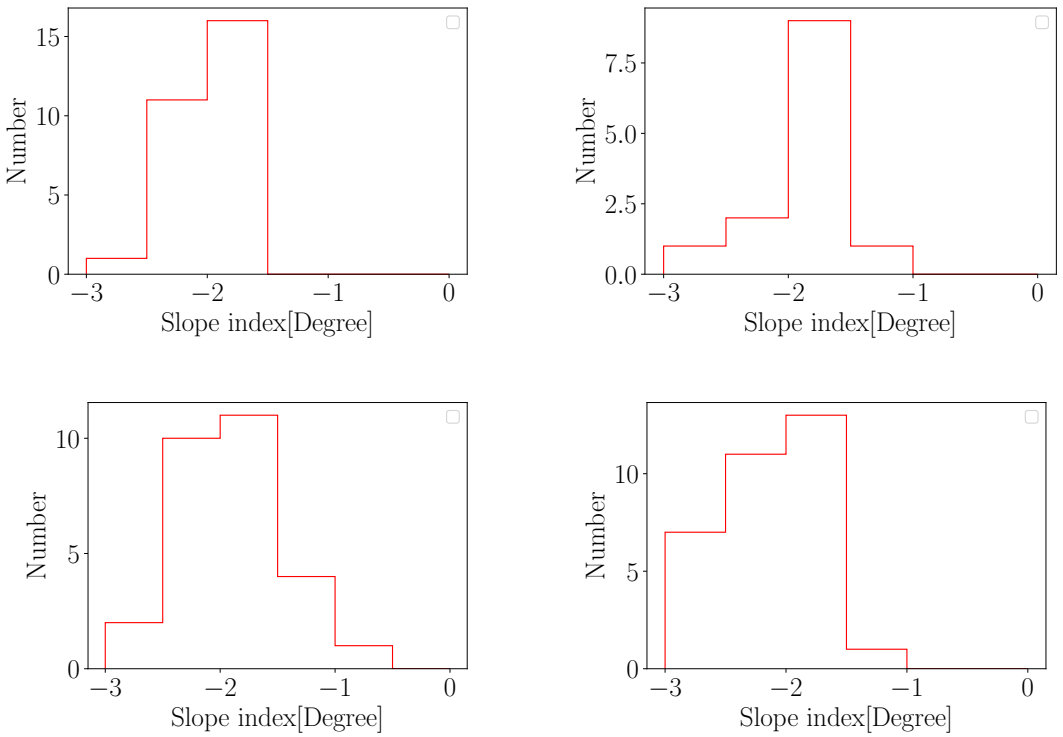

Figure 3.7: Histograms of slope index of velocity fluctuations, respectively. The top left, top right, bottom left, and bottom right panels are the results at 0.3, 0.4, 0.5, and 0.6 Myr, respectively.

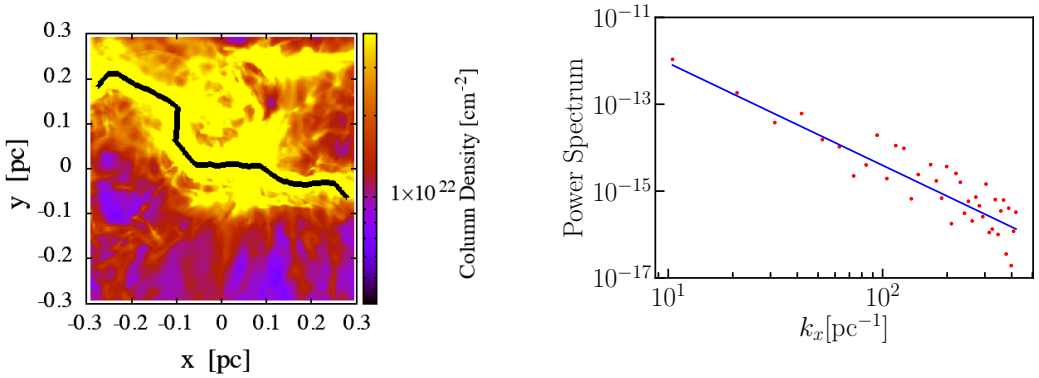

Figure 3.8: Column density map (left panel) and the power spectrum of column density (right panel). The black line in the left panel is the filament axis identified by using FilFinder. The red dots in right panel are resultant power spectrum derived from Equation 3.10, and the blue solid line is the fitting line whose slope index is -2.4 ± 0.6.

Chapter 4

Time Evolution of the Angular Momentum of Molecular Cloud Cores

4.1 Numerical Setup

We use the Godunov-type smoothed particle hydrodynamical (SPH) method (Inutsuka, 2002) to solve the following equation of motion:

$$\frac{d\boldsymbol{v}}{dt} = -\frac{1}{\rho}\nabla P + \nabla \int dx'^3 \frac{G\rho\left(x'\right)}{|x - x'|}, \tag{4.1}$$

where ∇ is the derivative with respect to x. We have used FDPS (Iwasawa et al., 2016) in our SPH code to accelerate the calculation. We have applied a periodic boundary condition in the z-direction which is parallel to the filament axis. We adopt an isothermal equation of state. We use the Barnes-Hut tree algorithm (Barnes & Hut, 1986) with opening angle of 0.4 to solve the gravity. We adopt the hydrostatic equilibrium density profile of a filament as initial condition:

$$\rho(r) = \rho_{\rm c0}\left[1 + \left(\frac{r}{H_0}\right)^2\right]^{-2}, \tag{4.2}$$

where $\rho_{\rm c0}$ is the density along the axis, r is the radius of the cylindrical coordinate, and H_0 is the scale height defined by

$$H_0 \equiv \sqrt{\frac{2c_{\rm s}^2}{\pi G\rho_{\rm c0}}}, \tag{4.3}$$

where $c_{\rm s} = 0.2$ km s^{-1} is sound speed. We consider an unmagnetized isothermal model filament with a width of 0.1 pc (Arzoumanian et al., 2011, 2019) and a line mass equal to the critical line mass, $\mathrm{M_{line,crit}} = 18\ \mathrm{M_\odot pc^{-1}}$ for $T = 10$ K. In this paper we choose $H_0 = 0.05$ pc. To mimic the periodic boundary condition in the z-direction, we put N copies of the filament on both sides. In this paper, we use $N = 4$.

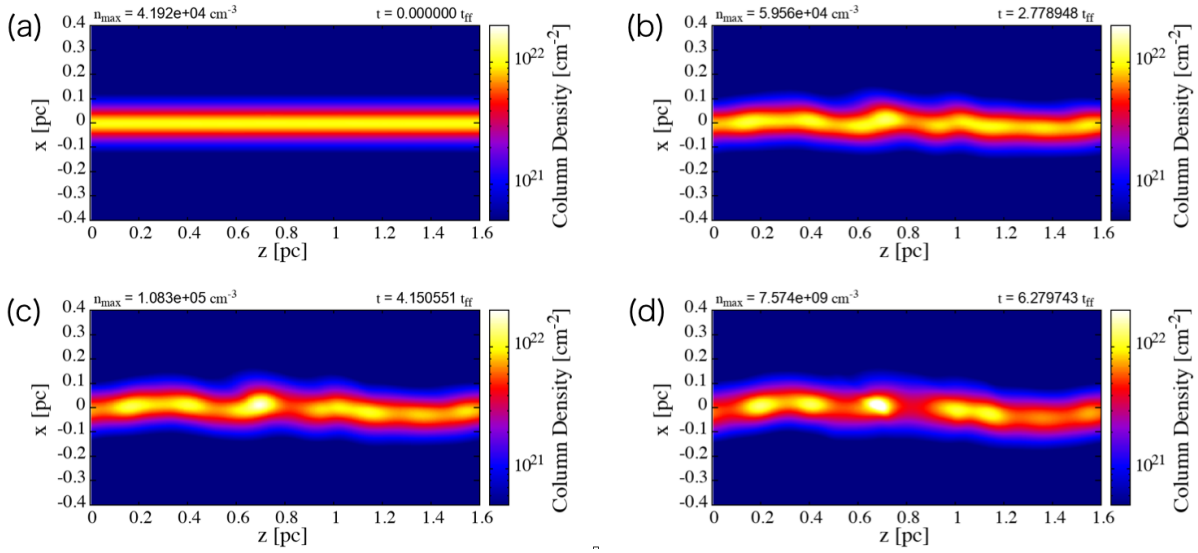

Figure 4.1: Time sequence of the fragmentation of a filament (from panel (a) to (d)). The color scale is the column density derived by integrating the density along the y-axis. The elapsed time and maximum density are denoted in each panel, where $t_{\rm ff}$ is the free fall time defined by $t_{\rm ff} = (4\pi G\rho_{\rm c})^{-1/2}$.

First we numerically generate the velocity field $\boldsymbol{v}$ in the filament following the method described in, e.g., Dubinski et al. (1995)

$$\boldsymbol{v}(\boldsymbol{x}) = \sum_{\boldsymbol{k}} \boldsymbol{V}(\boldsymbol{k}) \exp(\mathrm{i}\boldsymbol{k}\cdot\boldsymbol{x}), \tag{4.4}$$

where $\boldsymbol{V}(\boldsymbol{k})$ is the Fourier transform, $\boldsymbol{k}$ is the wave vector. The detail description is shown in Misugi et al. (2019). We use $\sigma = c_{\rm s}$ for our fiducial model, where σ is the three-dimensional velocity dispersion. Note that this transonic velocity turbulence is consistent with the recent measurement of fluctuations of line-of-sight velocity along critical filaments in nearby molecular clouds (Hacar & Tafalla, 2011; Arzoumanian et al., 2013; Hacar et al., 2016). **Misugi et al (2019) concluded that, if the filament is embedded in the molecular cloud with Kolmogorov turbulence, the resultant core AM is consistent with observations and the velocity power spectrum along the filament axis follows 1D Kolmogorov power spectrum. Hence, we adopt Kolmogorov turbulence as the initial velocity field in this paper. Although Misugi et al. (2019) found that Kolmogorov-like, anisotropic power spectrum model was also compatible with the observed angular momentum of the cores, in this paper we focus on the isotropic Kolmogorov turbulence.**

4.2 Results

4.2.1 Overview

We run a filament fragmentation simulation until the maximum density reaches $\rho_{\rm crit} = 2.8 \times 10^{-14}$g cm^{-3} ($n_{\rm crit} = 7.3 \times 10^{9}$cm^{-3}), which corresponds to $\rho_{\rm crit} = 2 \times 10^{5}\rho_{\rm c0}$, where $\rho_{\rm c0} = 1.4 \times 10^{-19}$g cm^{-3} ($n_{\rm crit} = 3.4 \times 10^{4}$cm^{-3}) is the initial peak density of the filament. Therefore, our simulation is stopped before the first core forms in the central high density region ($n \simeq 5 \times 10^{10}$cm^{-3}) (Masunaga & Inutsuka, 2000). First, we describe the filament fragmentation due to the growth of initial perturbations. Figure 4.1 displays the time sequence of fragmentation of a filament. The color scale is the column density derived by integrating the density along the y-axis. **The z-axis is parallel to the filament axis, and the x and y-axis are perpendicular to the filament axis.** The elapsed time and maximum density are denoted in each panel, where $t_{\rm ff}$ is the free fall time defined by $t_{\rm ff} = (4\pi G\rho_{\rm c0})^{-1/2}$.

4.2.2 Core Angular Momentum

In this subsection, we measure the core angular momentum and investigate its time evolution. **As we mentioned in the previous subsection, we stop the simulations before the first core forms in the central high density region ($n \simeq 5 \times 10^{10}$cm^{-3}). Then, we find and analyze the core with the highest density in the filament (the fastest collapsing core). We define the core using a density contour threshold and we measure the enclosed mass in the contour.** We repeat this procedure changing the density threshold until the enclosed mass reaches 1 M$_\odot$. Thus, in this section, all cores have the same mass, 1 M$_\odot$. The core finding algorithm takes into account the periodic boundary conditions. Then, we trace the trajectories of the SPH particles from the final state to the initial state of the simulation. Figure 4.2 shows the time sequence of the morphology and the specific angular momentum of a core from our simulations. The first, second, and third rows show the column density on the x-y, x-z, and y-z planes, respectively. The color scale is the specific angular momentum of the SPH particles around the barycenter of the core. The panels from left to right are snapshots at the stages of $n = 4.192 \times 10^{4}$cm^{-3}, $n = 1.675 \times 10^{5}$cm^{-3}, and $n = 7.574 \times 10^{9}$cm^{-3}, respectively. The elapsed time and maximum density are denoted in each panel. Next, we derive the specific angular momentum of the core with respect to the center of mass using the definition of the core explained above:

$$\boldsymbol{J} = \sum_i m_i(\boldsymbol{x}_i - \boldsymbol{x}_{\rm c}) \times (\boldsymbol{v}_i - \boldsymbol{v}_{\rm c}), \tag{4.5}$$

where $\boldsymbol{x}_i$ and $\boldsymbol{v}_i$ are the position and velocity vectors of the SPH particles, $\boldsymbol{x}_{\rm c}$ and $\boldsymbol{v}_{\rm c}$ are the position and velocity of the center of mass of the core. The specific angular momentum of a core is defined as follows:

$$\boldsymbol{j} = \frac{|\boldsymbol{J}|}{M}, \tag{4.6}$$

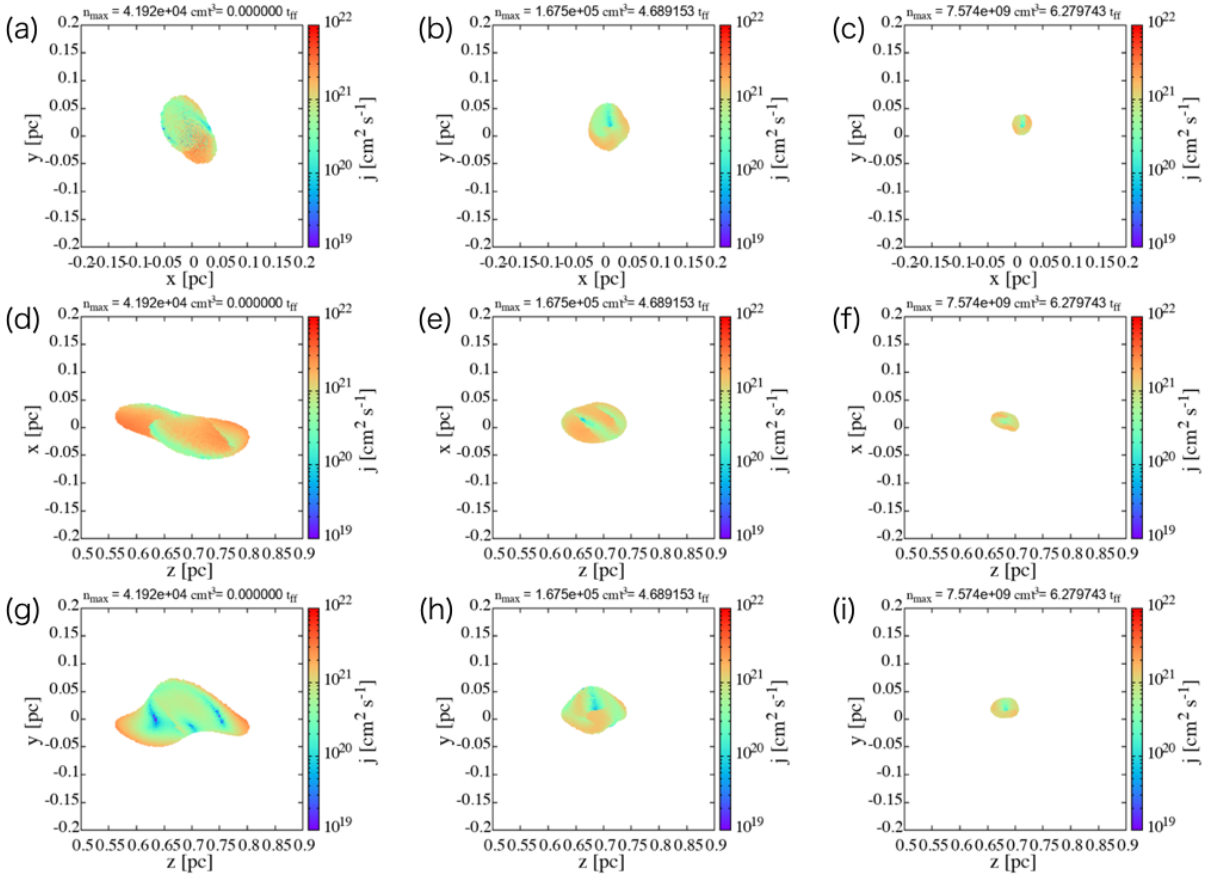

Figure 4.2: Time sequence of morphology and specific angular momentum of a core from left to right. The first, second, and third row are on the x-y, x-z plane, and y-z plane, respectively. The color scale is the specific angular momentum of SPH particles. **This core is defined by the density contour enclosing a mass of** 1 $M_\odot$ **at final time step.** The panels from left to right are snapshots at stages of $n = 4.192 \times 10^4 \mathrm{cm}^{-3}$, $n = 1.675 \times 10^5 \mathrm{cm}^{-3}$, and $n = 7.574 \times 10^9 \mathrm{cm}^{-3}$, respectively. The elapsed time and maximum density are denoted in each panel.

where M is the total mass of the core (**here** $M = 1$ $M_\odot$). Figure 4.3 displays the time evolution of j of the core shown in Figure 4.2. The horizontal axis is the elapsed time. The left panel is for the absolute value of the specific angular momentum, and **the** right panel shows **each** component of the specific angular momentum. **The red dashed line, blue solid line, and green dotted line** in the right panel are the x, y, and z components of the specific angular momentum. Note that the angular momentum should be conserved in the absence of interaction with surrounding matter. As one can see from Figure 4.3, the core angular momentum changes by around 30%. **In the right panel of Figure 4.3,** j_x **and** j_z **are smaller than** j_y**. The reason why** j_x **is smaller than** j_y **is due to a phase of initial turbulence in the filament studied in this subsection. Statistically, the** j_x **and** j_y **follow the same distribution because the ve-**

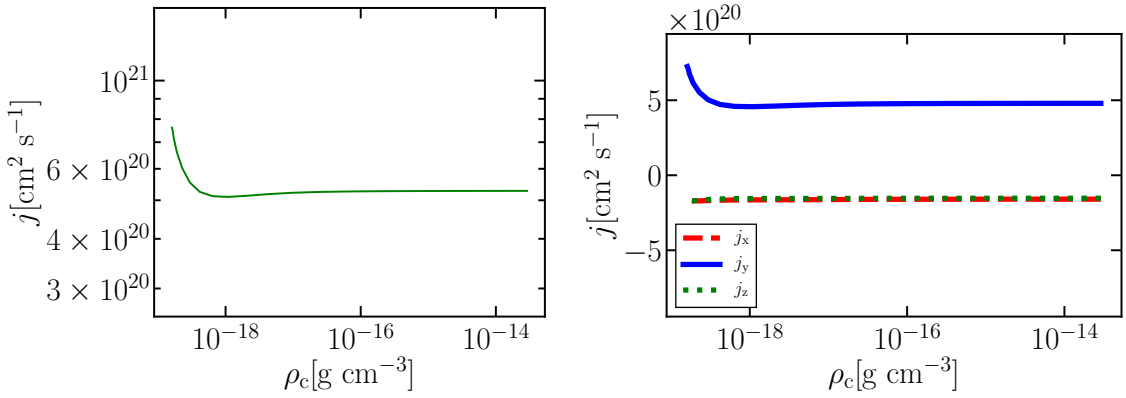

Figure 4.3: (left)The time evolution of the absolute value of the specific angular momentum of the core shown in Figure 4.2. The horizontal axis is the maximum density of the core. The density evolution traces also the time evolution as the core collapses. (right)The time evolution of the component of the specific angular momentum of the core shown in Figure 4.2. **The red dashed line, blue solid line, and green dotted line** are the x, y, and z components of the specific angular momentum. The vertical axis is logarithmic in the left panel but linear in the right panel.

locity field is isotropic and the filament is axis symmetric. The reason why j_z is smaller than j_y will be explained in Section 4.2.3.

To analyze this evolution in more detail, we calculate the torque exerted on the core. The gravitational torque ($\boldsymbol{T}_{\rm g}$) and pressure torque ($\boldsymbol{T}_{\rm f}$) are derived separately as follows:

$$\boldsymbol{T}_{\rm g} = \sum_i (\boldsymbol{x}_i - \boldsymbol{x}_{\rm c}) \times \boldsymbol{F}_{{\rm g},i}, \tag{4.7}$$

$$\boldsymbol{T}_{\rm f} = \sum_i (\boldsymbol{x}_i - \boldsymbol{x}_{\rm c}) \times \boldsymbol{F}_{{\rm f},i}, \tag{4.8}$$

where $\boldsymbol{F}_{{\rm f},i}$ and $\boldsymbol{F}_{{\rm g},i}$ are the pressure **(the first term of the right hand side of Equation 4.1)** and the gravity force **(the second term of the right hand side of Equation 4.1)** of ith particle, respectively. The gravitational torque and the pressure torque are shown in Figure 4.4. The total torque $\boldsymbol{T} = \boldsymbol{T}_{\rm f} + \boldsymbol{T}_{\rm g}$ is plotted in Figure 4.5. The horizontal axis is the maximum density of the core, that is, time evolution. Since our initial filament is in hydrostatic equilibrium, the total torque exerted on the core is zero at $t = 0$. As time progresses, both the gravitational and the pressure torques decrease as shown in Figure 4.4. This is because the core evolves to the sphere-like shape as shown in Figure 4.2. The specific angular momentum of the core changes by 30% due to the fluctuations of gravity and pressure generated by the initial Kolmogorov velocity fluctuations.

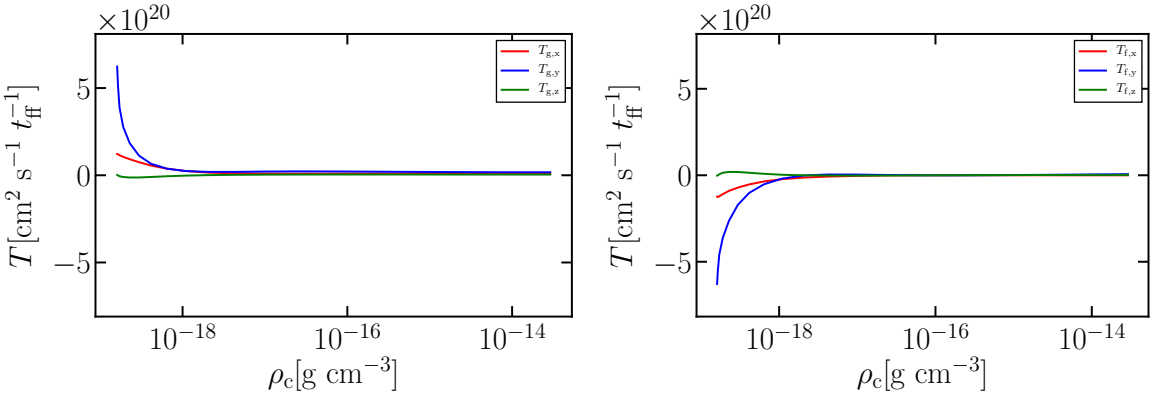

Figure 4.4: Gravitational torque (left) and pressure torque (right) exerted on the core. The horizontal axis is the maximum density of the core and the vertical axis is the torque. The red, blue, and green curves are the x, y, and z components of the torque.

Note that the angular momentum decreases by around 30% at the early stage and is almost constant at the later stage. The reason why the angular momentum of the cores does not change at the later stage will be explained **in the next subsection** (see Equation 4.9).

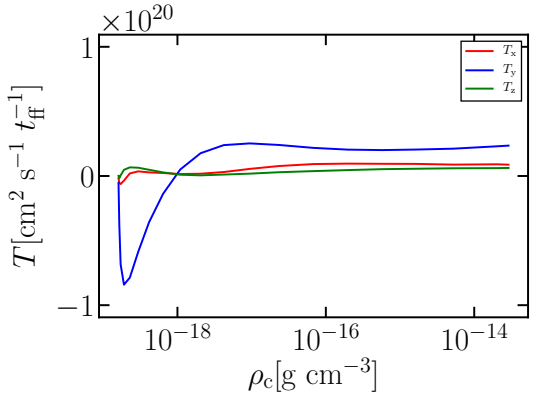

Figure 4.5: Total torque exerted on the core. The horizontal axis is the maximum density of the core and the vertical axis is the total torque $\boldsymbol{T} = \boldsymbol{T}_{\mathrm{f}} + \boldsymbol{T}_{\mathrm{g}}$. The red, blue, and green are the x, y, and z components of the total torque.

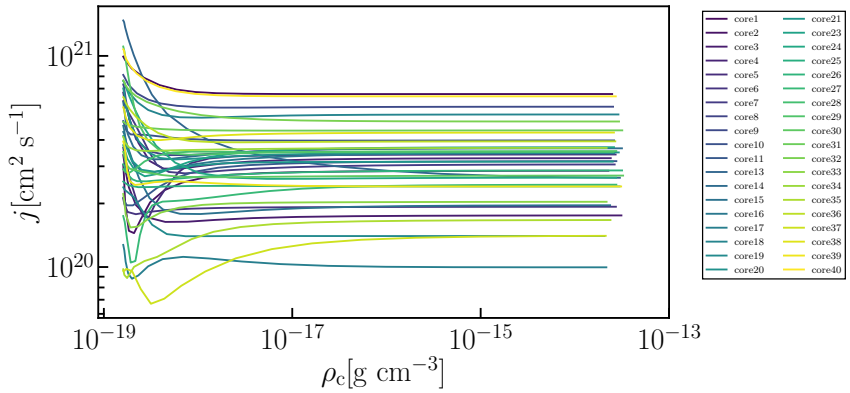

Figure 4.6: The time evolutions of the specific angular momentum of the 38 cores. The horizontal axis is the maximum density of the cores. The different colors of solid lines correspond to the different cores derived from the 38 runs.

4.2.3 Statistical Properties of the Total Angular Momentum of the Core

We run 40 sets of simulations using different turbulence seeds and statistically analyze the properties of the core angular momentum. The analysis described in the previous subsections is applied to all the resultant filaments in these simulations. We build a sample of 40 cores selecting the fastest growing core of each simulation. The time evolutions of 38 cores are shown in Figure 4.6. Because two cores have two peaks within their 1 $M_\odot$ contour, we exclude these two cores from the analysis in this section. The horizontal axis of Figure 4.6 is the maximum density of the cores. The different colors of the solid lines correspond to different cores. Figure 4.7 is the averaged time evolutions of specific angular momentum of all cores. The red solid line is the averaged specific angular momentum of the cores shown in Figure 4.6.

As we can see from Figures 4.6 and 4.7, the core angular momentum is almost constant during the runaway collapse phase. This result can be understood as follows. First, the change of the angular momentum can be estimated by integrating the gravitational torque with respect to time. Figure 4.8 displays the averaged time evolutions of the gravitational torque exerted on the cores. The vertical axis is the gravitational torque. The horizontal axis is the maximum density of the core. Figure 4.8 shows that the averaged gravitational torque during the runaway collapse phase is $T_g \sim 2.5 \times 10^{19}$ cm^2 s^{-1} t_{ff}^{-1}. Using this value, the change of the angular momentum during the runaway collapse phase is estimated as follows:

$$\begin{aligned}\Delta j &= \int T_g dt \\ &= T_g[t_{ff}(\rho_r) - t_{ff}(\infty)] \\ &\sim 2.5 \times 10^{19} \sqrt{\frac{\rho_{c0}}{\rho_r}} \text{ cm}^2 \text{ s}^{-1}, \end{aligned} \tag{4.9}$$

where ρ_{c0} is the initial peak density of the filament, and ρ_r is the lower limit of the integration. In this analysis, we use $\rho_r = 10^{-17}$g cm^{-3} because we conform that the collapse follows the runaway collapse when $\rho_r \gtrsim 10^{-17}$g cm^{-3}. If we substitute $\rho_r = 10^{-17}$g cm^{-3} into Equation 4.9, the resultant change of the angular momentum is $\Delta j \simeq 2.5 \times 10^{18}$ cm^2 s^{-1}. Since this is smaller than the averaged specific angular momentum at the later stages ($j \simeq 3 \times 10^{20}$ cm^2 s^{-1}) shown in Figure 4.6 by two orders of magnitude, we can conclude that the total angular momentum of the core is almost constant during the runaway collapse phase.

Figure 4.6 also shows that the specific angular momentum of the cores decreases **initially** by around 30% as shown in the previous subsection. To investigate the time evolution of the specific angular momentum of the cores statistically, we show the histograms for the specific angular momentum of the cores at both the initial stage (left panel of Figure 4.9) and at the final stage (right panel of Figure 4.9). Figure 4.9 shows that the initial specific angular momentum decreases by 30% as shown in Figure 4.3 and Figure 4.6.

The typical value of the core angular momentum can be estimated by using the method shown in Peebles (1969). The shape of cores tend to be elliptical rather than spherical at the initial stage (Figure 4.2). The angular momentum of the initial elliptical core can be written formally as follows:

$$\boldsymbol{J} = \int \rho \boldsymbol{r} \times \boldsymbol{v} d^3x. \tag{4.10}$$

This integration is calculated as follows (See Appendix A for more details):

$$\boldsymbol{J} = -\frac{M}{5} \sum_{\boldsymbol{k}} \boldsymbol{V}(\boldsymbol{k}) \times \boldsymbol{k}'' f(y) \cos\phi_{\boldsymbol{k}} \tag{4.11}$$

where $\boldsymbol{k}'' = (k_x a_1^2, k_y a_2^2, k_z a_3^2)$, $y = |\boldsymbol{k}'|$, $\boldsymbol{k}' = (k_x a_1, k_y a_2, k_z a_3)$. $M = 4\pi\rho a_1 a_2 a_3/3$ and a_i $(i = 1, 2, 3)$ are the mass and the principal axes of the ellipsoid, respectively. $\phi_{\boldsymbol{k}}$ is the phase of initial velocity field. For simplicity, we assume the density is constant. $f(y)$ is defined as follows:

$$f(y) = 45 \left(\frac{\sin y}{y^5} - \frac{\cos y}{y^4} - \frac{\sin y}{3y^3} \right). \tag{4.12}$$

Then we can derive the specific angular momentum

$$\begin{aligned} j &\equiv \frac{\sqrt{\langle \boldsymbol{J}^2 \rangle}}{M} \\ &= \sqrt{\frac{1}{75} \sum_{\boldsymbol{k}} P(k) \boldsymbol{k}''^2 f(y)^2}, \end{aligned} \tag{4.13}$$

where $\langle\rangle$ represents the ensemble average. $P(k)$ is the power spectrum of the velocity field. If we substitute the typical value $a_3 = 0.085$pc, $a_1 = a_2 = a_3/2 = 0.0425$pc into Equation 4.13, the specific angular momentum of the core becomes

$$j = 5.6 \times 10^{20} \mathrm{cm}^2 \mathrm{s}^{-1}. \tag{4.14}$$

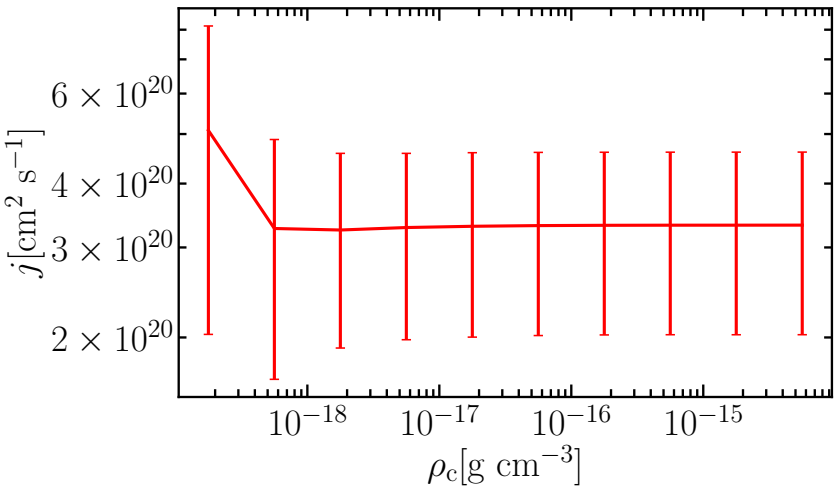

Figure 4.7: The averaged time evolutions of the specific angular momentum of the cores. The red solid line is the averaged specific angular momentum of the 38 cores shown in Figure 4.6. The vertical bars show the dispersion.

This is consistent with the peak position of Figure 4.9.

Additionally, We also derived the time evolution of the angle between the filament axis and the core angular momentum axis. The angle between the filament axis and the core angular momentum axis is defined as $\cos\theta = J_z/J$. The time evolution of θ is plotted in Figure 4.10. The vertical axis is the number of cores per θ bin. Figure 4.10 describes that most of the cores are nearly perpendicular to the filament axis. Since the core is formed through filament fragmentation, the core is elongated along the z-axis (filament longitudinal direction) at the initial state as shown in Figure 4.2. **As shown in Equation 4.5, the angular momentum of the core depends on the distance from the barycenter. Only the x and y components of the angular momnetum is affected by the z component of the distance from the barycenter.** Therefore, most cores rotate nearly perpendicular to the filament axis even though the initial velocity turbulence field is isotropic. We stress that this trend can be observed even at the final state of simulation (right panel of Figure 4.10).

Figure 4.11 shows the time evolution of the rotation energy normalized by thermal energy, $E_{\rm rot}/2E_{\rm th}$. The horizontal axis is the maximum density of the core. Each color corresponds to each core. The rotation energy $E_{\rm rot}$ is calculated as follows:

$$E_{\rm rot} = \sum_i m_i \left[\frac{(\boldsymbol{x}_i - \boldsymbol{x}_{\rm c}) \times (\boldsymbol{v}_i - \boldsymbol{v}_{\rm c})}{|\boldsymbol{x}_i - \boldsymbol{x}_{\rm c}|} \right]^2, \tag{4.15}$$

where i is a subscript of SPH particle.Figure 4.11 shows that the rotation energy decreases during the core formation stage and increases at the later stage. This evolution can be understood as follows. Since the angular momentum of a core decreases during the core formation stage, the rotation energy also decreases

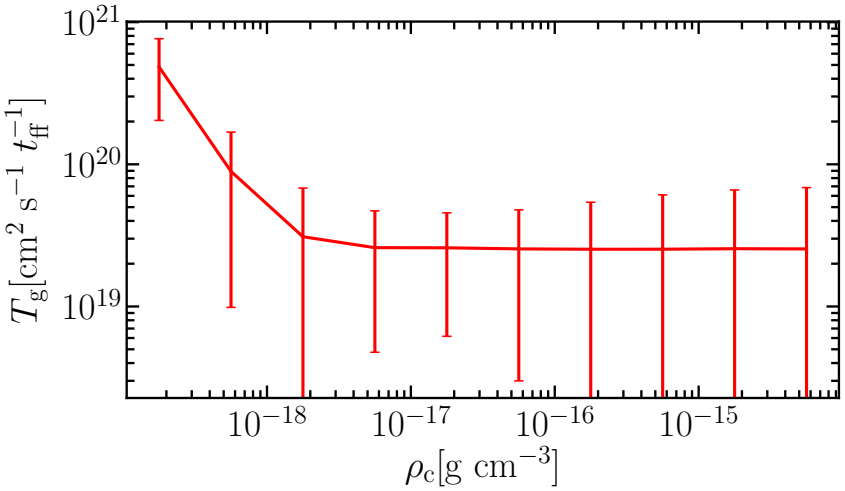

Figure 4.8: The averaged time evolutions of the gravitational torque exerted on the cores. The vertical axis is the gravitational torque. The horizontal axis is the maximum density of the core.

when the central density 10^{-19}g cm$^{-3} \lesssim \rho_{\rm c} \lesssim 10^{-18}$g cm^{-3}. Since we trace the trajectories of particles in this analysis, the mass M defined in Equation 4.15 is constant, the rotation energy $E_{\rm rot} \sim I\omega^2 \sim J^2/MR^2 \propto R^{-2}$. Therefore, the rotation energy increases during the **runaway** collapse phase. As we can see from Figure 4.11, $E_{\rm rot}/2E_{\rm th} \sim 0.01$ at the initial state, then $E_{\rm rot}/2E_{\rm th}$ increases up to $E_{\rm rot}/2E_{\rm th} \sim 0.1$ at the final state, just before the first core formation.

Figure 4.12 displays the distribution of axis ratios of all cores. To estimate the shape of a core, we calculate the moment of coordinates,

$$K_{ln} = \sum_i m_i (x_{l,i} - x_{l,{\rm c}})(x_{n,i} - x_{n,{\rm c}}). \tag{4.16}$$

The shape of the core **is** estimated from the three principal axes ($a_1 < a_2 < a_3$) defined by the square roots of three eigenvalues of K_{ln}. This analysis is essentially the same as that used in Matsumoto & Hanawa (2011).

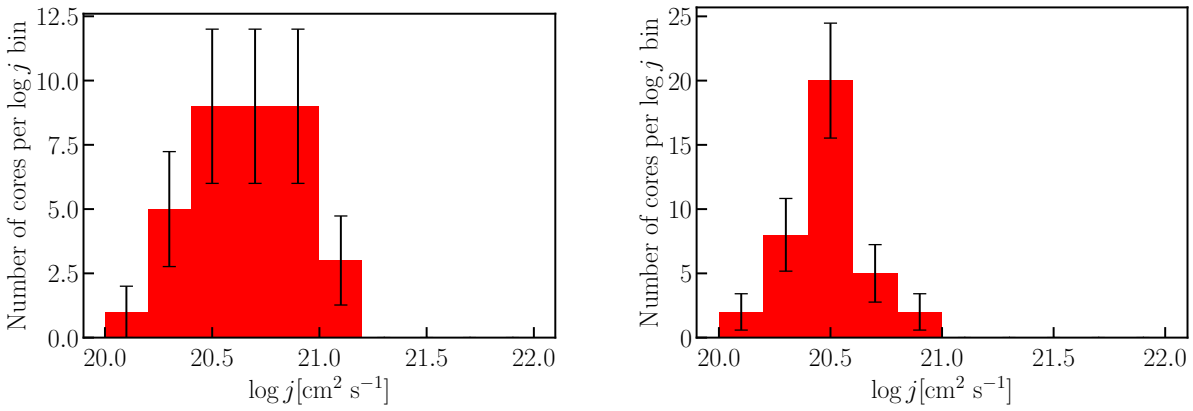

Figure 4.9: Histograms of the specific angular momentum of the cores at the initial state (left) and at the final state (right) with statistical error bars. The vertical axis is the number of cores per $\log j$ bin.

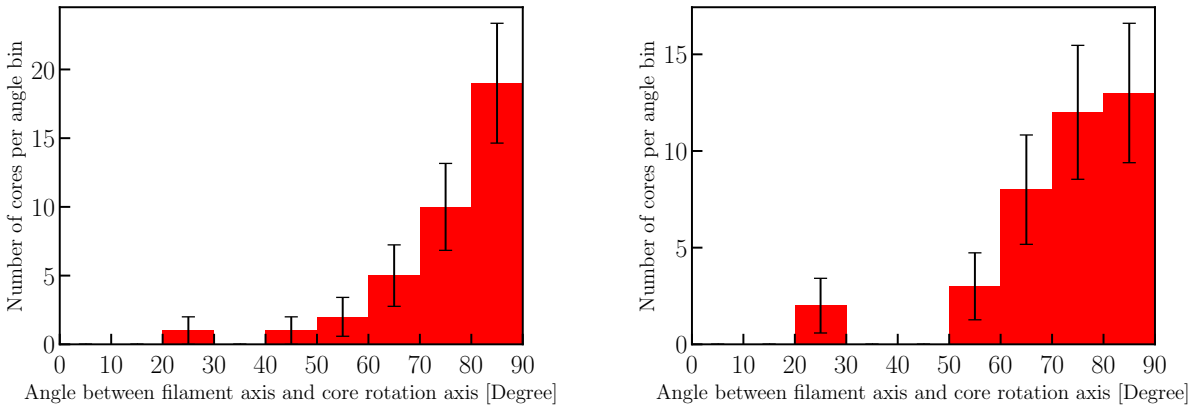

Figure 4.10: Histogram of the angle θ between the filament axis and core angular momentum axis at the initial state (left) and at the final state (right) with statistical error bars. The vertical axis is the number of cores per θ bin.

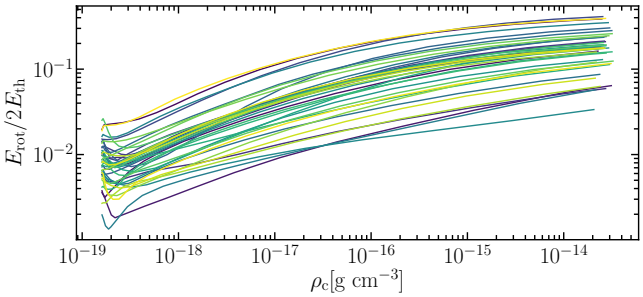

Figure 4.11: Time evolution of the rotation energy normalized by the thermal energy. The horizontal axis is the maximum density of the core. Each color corresponds to each core.

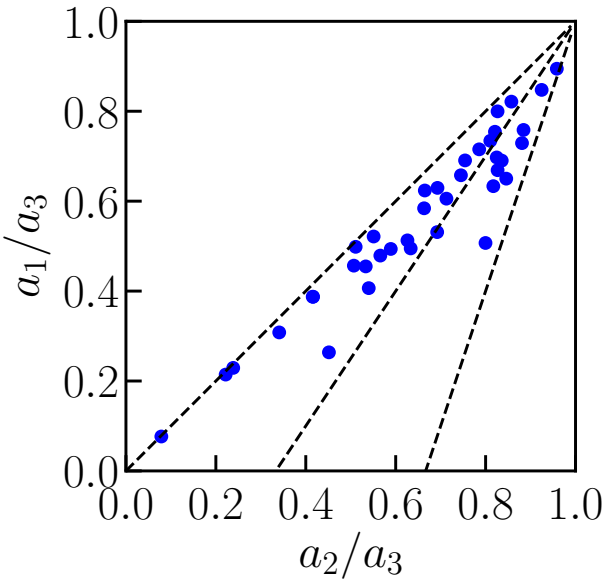

Figure 4.12: Distribution of axis ratios of all cores. Each blue circle corresponds to each core. The axis of a core are the eigenvalue of inertia moment, and $a_1 < a_2 < a_3$. The three dashed lines are the boundaries between prolate, triaxial, and oblate shapes from left to right.

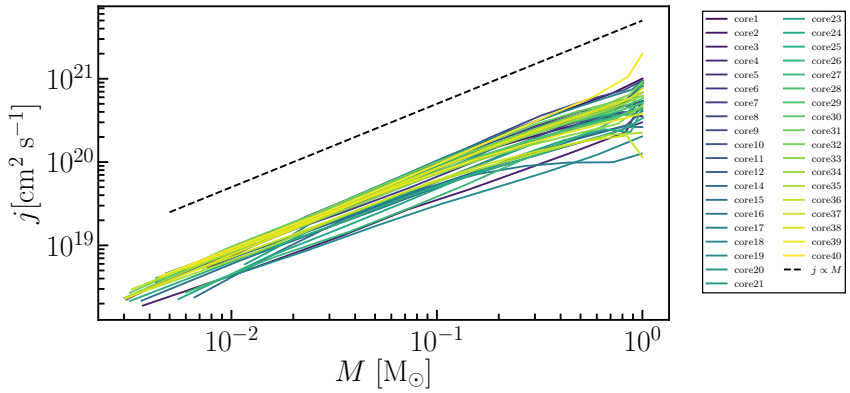

Figure 4.13: Internal angular momentum structure. The vertical axis is the specific angular momentum of a shell. The horizontal axis is **the total mass enclosed by the shell**. The different colors of solid lines coresspond to the different cores. The black dashed line represents $j \propto M$.

4.2.4 Internal Structure of Core Rotation

Observations show that the internal motion of **protostellar cores** is not always coherent (e.g., Gaudel et al., 2020). Moreover, warped disks are discovered in young stellar objects (e.g., Sakai et al., 2019). Some observations even reported that the outflows/jets were driven in multiple directions, which was interpreted as the incoherent angular momentum axis distribution inside a parental dense core (e.g., Okoda et al., 2021). To elucidate the formation mechanism of observed complex structures, studying the internal structure of cores at the core formation stage in the filamentary molecular cloud is very important. In the previous subsection we provide the results for time evolution of the total angular momentum of the cores. In this subsection, we focus on the internal angular momentum structure of a core.

Angular Momentum Profile inside a Core

First, we divide the core in concentric shells using density contours at each time step of the simulations. We measure the angular momenta of the shells around the density maxima as follows:

$$\boldsymbol{J}_{\rm shell} = \sum_{i \in {\rm shell},\ j} m_i (\boldsymbol{x}_i - \boldsymbol{x}_{\rho{\rm max}}) \times (\boldsymbol{v}_i - \boldsymbol{v}_{\rho{\rm max}}), \tag{4.17}$$

where $\boldsymbol{x}_{\rho{\rm max}}$ and $\boldsymbol{v}_{\rho{\rm max}}$ are the position and velocity of the density maxima, respectively. The summation is calculated for SPH particles contained in each shell j. Figure 4.13 displays the specific angular momentum of shells. The vertical axis is the specific angular momentum of a shell. The horizontal axis is **the total mass enclosed by the shell**. The different colors of solid lines correspond to the different cores. The black dashed line represents $j \propto M$. Figure 4.14 displays the time evolution of j-M profile in a core. The j-M profiles evolve from the blue

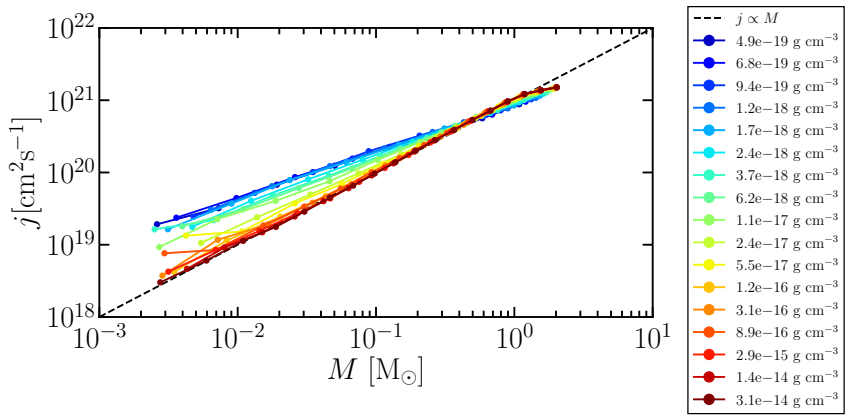

Figure 4.14: Time evolution of j-M profile in a core. The black dashed line is $j \propto M$. The j-M profiles of the core evolve from the blue line to the red line.

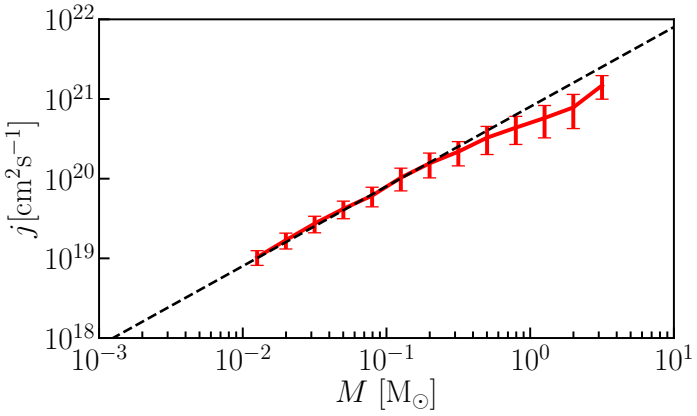

Figure 4.15: Averaged j-M profile for the 38 cores. The red solid line is the averaged j-M profile using all j-M profiles of the cores shown in Figure 4.13. The black dashed line is $j \propto M$.

line to the red line. The density shown in the legend of Figure 4.14 corresponds to the maximum density of the cores at each time step. In addition, Figure 4.15 displays the averaged j-M profile. The red solid line is the averaged j-M profile using all j-M profiles of the cores shown in Figure 4.13. Figure 4.13, 4.14, and 4.15 show that the j-M profile evolves to $j \propto M$ with time during the runaway collapse phase. $j \propto M$ is the self-similar solution discussed in Saigo & Hanawa (1998) and **Basu (1997)**, and we will explain this later. This convergence to $j \propto M$ was reported in Tomisaka (2000) where they investigated the evolution of the angular momentum profile in collapsing magnetized molecular cloud core without turbulence.

Figure 4.16 shows $j \propto r$ profile in the cores, where r is the distance from the density peak. The vertical axis is the specific angular momentum of a core, and the horizontal axis is the distance from the density peak of the core. The black

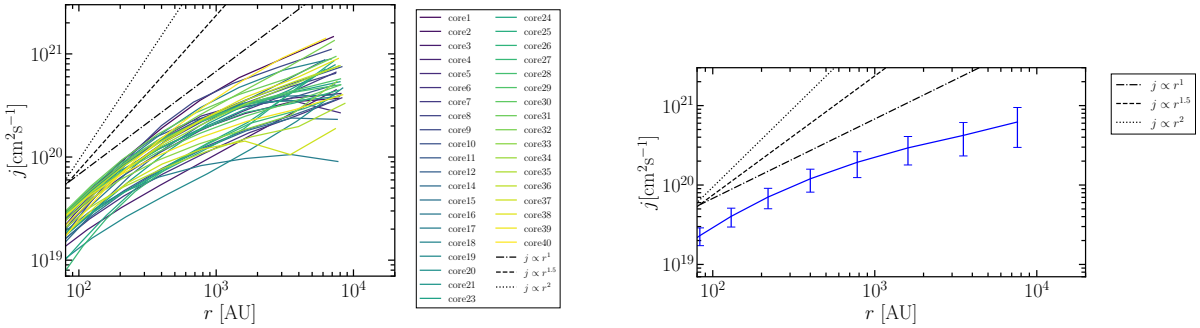

Figure 4.16: Angular momentum profile in the cores. The vertical axis is the specific angular momentum of a core, and the horizontal axis is the distance from the density peak of the core. In the left **panel**, each color corresponds to each core. The black dash-dotted line, dashed line, and dotted line are $j \propto r^1$, $j \propto r^{1.5}$, and $j \propto r^2$, respectively. The blue line in the right **panel** is the averaged j-r profile of the cores shown in the **left panel**.

dash-dotted line, dashed line, and dotted line are $j \propto r$, $j \propto r^{1.5}$, and $j \propto r^2$, respectively. The blue line in the right **panel** is averaged j-r profile of the cores shown in the **left panel**. $j \propto r$ can be seen in the inner region of the cores. This is because Larson-Penston solution (Larson, 1969; Penston, 1969) has density profile $\rho \propto r^{-2}$, this means $M \propto r$. Using this relation and $j \propto M$ (Figure 4.14), we can derive the $j \propto r$ relation. Please note that the slope index j-r relation in the inner region of the core expected from the self-similar solution ($j \propto r$) is different from the slope index expected from Larson's law ($j \propto r^{1.5}$).

Figure 4.17 displays the time evolution of the angle between the rotation axis of the inner region of the core and the filament axis. **The color scale represents the ensemble average of the angle between the rotation axis of the inner region of the core and the filament axis over all the cores.** The vertical axis is the maximum density. The horizontal axis is the enclosed mass within the shell and corresponds to the distance from the center of the core. Figure 4.17 indicates that the angle between the rotation axis and the filament axis is almost constant over time and nearly perpendicular to the filament axis over the whole mass range, even in the inner region of the core. Note that θ of the inner region of the core slightly changes with time, while the outer region is almost constant, as shown in Equation 4.9. The reason why the angular momentum of the inner region of the core continues to evolve in the early stage of runaway collapse is discussed below. At the initial stage, the rotation axis of the inner region of the core tends to be more parallel **to the filament axis** compared to the outer region. This is because the inner region of the core is not significantly affected by the filament geometry.

In the following, we study the mechanism of angular momentum transfer in the cores. First, we evaluate the gravity and pressure torque as follows:

$$\boldsymbol{T}_{\mathrm{f,shell}} = \sum_{i \in \mathrm{shell},\ j} (\boldsymbol{x}_i - \boldsymbol{x}_{\rho\mathrm{max}}) \times \boldsymbol{F}_{\mathrm{f},i}, \tag{4.18}$$

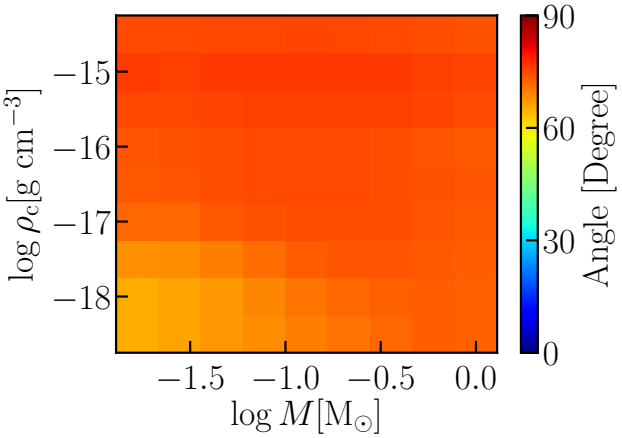

Figure 4.17: Time evolution of the angle between the core rotation axis and the filament axis. The vertical axis is the maximum density of a core. The horizontal axis is the enclosed mass within the shell.

$$\boldsymbol{T}_{\rm g,shell} = \sum_{i\in{\rm shell},\ j} (\boldsymbol{x}_i - \boldsymbol{x}_{\rho{\rm max}}) \times \boldsymbol{F}_{{\rm g},i}. \tag{4.19}$$

In Figure 4.18, we show the efficiency of the angular momentum transfer due to the total torque during the runaway collapse phase. The vertical axis is the maximum density of a core. The horizontal axis is the enclosed mass within the shell. **The color shows the efficiency of the angular momentum transfer which is defined by the ratio of $Tt_{\rm ff}$ to the angular momentum of the shell J, where $t_{\rm ff}$ is the free fall time at each time step, T is the total torque exerted on the shell, and $\langle\ \rangle$ represents the ensemble average for the 38 cores. Since $Tt_{\rm ff}$ corresponds to the amount of the angular momentum transferred in later runaway collapse phase, we can estimate the efficiency of the angular momentum transfer in subsequent runaway collapse.** Figure 4.18 shows that the transfer of the angular momentum due to the total torques is efficient to change their angular momentum only when the central density $\lesssim 10^{-16}$g cm^{-3}. The angular momentum is an increasing function of **enclosed** mass as shown in Figure 4.14. This is the reason why the **total torque acting on a core remains more efficient in the inner region than in the outer region until a later evolutionary stage.** Figure 4.19 displays the sign of the total, pressure, and gravitational torques with respect to the angular momentum during the runaway collapse phase. **The vertical axis and the horizontal axis are the same as Figure 4.18**. The hat symbol means the unit vector. The color shows the inner product between the unit vector of the angular momentum and the unit vector of the total, pressure, and gravitational torques. The upper panel of Figure 4.19 indicates that the total torque exerted on the cores reduces the angular momentum of the cores. This is because the initial shape of the core has a complex structure as shown in Figure 4.2. The reason why the negative pressure torque acts on the core in the initial eevoulutional

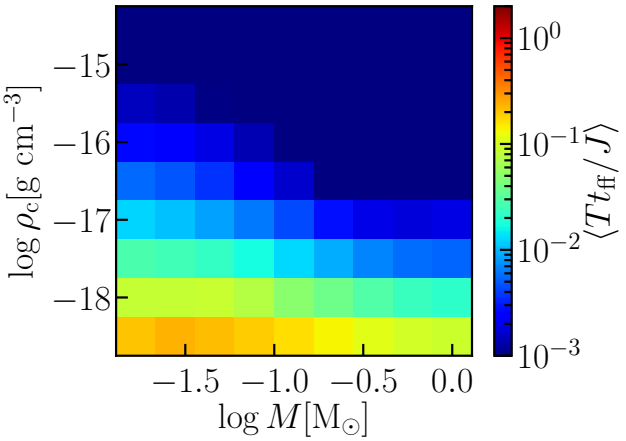

Figure 4.18: Rate of angular momentum transfer due to the total torque during the runaway collapse phase. The vertical axis is the maximum density of a core. The horizontal axis is the enclosed mass within the shell. The color shows the efficiency of angular momentum transfer which is defined by the ratio of the torque acting on the shell during the collapse $Tt_{\rm ff}$ to angular momentum of the shell J, where $t_{\rm ff}$ is the free fall time at each time step, and $\langle\ \rangle$ represents the ensemble average for the 38 cores.

stage is as follows. **At the initial state, the major axis of the core is not aligned to the filament axis as shown in Figure 4.2 (d). However, as time progresses, the core rotates towards the main axis of the filament (Figure 4.2 (e)). For the case of Figure 4.2(d)-(f), the core rotates in the counterclockwise direction, then the major axis of the core passes through the z-axis. This is typical evolution observed in our simulations.** This rotation direction is preferred to gather the mass of a core. Since the initial filament is in hydrostatic equilibrium, the direction of the pressure torque and the gravitational torque are opposite. However, in the later runaway collapse phase, the cores forget the initial filament geometry, and both torques become negative with respect to the rotation direction as shown in Figure 4.19.

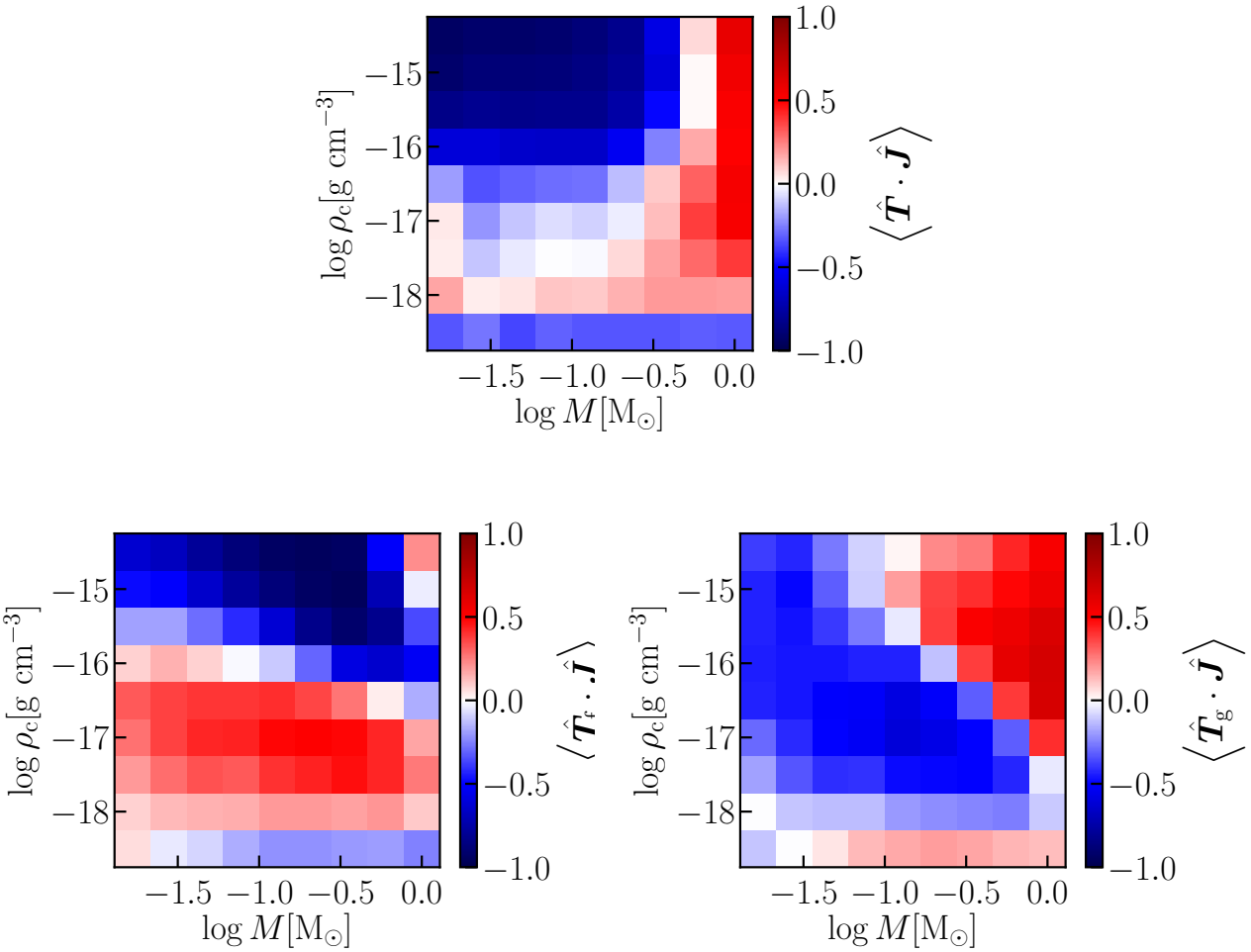

Figure 4.19: Sign of the total (upper panel),pressure (lower left panel), and gravitational (lower right panel) torques with respect to the angular momentum during the runaway collapse phase. The vertical axis is the maximum density of a core. The horizontal axis is the total mass within the shell. The hat symbol means the unit vector. The color shows the inner product between the unit vector of angular momentum and the unit vector of the total (upper panel), pressure (lower left panel), and gravitational (lower right panel) torques.

Complexity of the Internal Angular Momentum Structure

Figure 4.20 is the comparison between the clean rotation (nearly uniform angular momentum distribution in the core) and the complex rotation structure found in our simulations. The upper and lower panels are the smooth and complex velocity structure cases, respectively. The isosurfaces represent the isodensity surfaces, $\rho = 3.0 \times 10^{-19}$g cm^{-3} (upper panel) and $\rho = 3.5 \times 10^{-19}$g cm^{-3} (lower panel). The blue arrows are the direction of the rotation velocity. The rotation velocity $v_{\rm rot}$ is defined as follows:

$$\boldsymbol{v}_{\rm rot} = \boldsymbol{v} - \boldsymbol{v}_{\rho \rm max} - [(\boldsymbol{v} - \boldsymbol{v}_{\rho \rm max}) \cdot \boldsymbol{r}]\boldsymbol{r}/r^2, \tag{4.20}$$

where $\boldsymbol{v}_{\rho \rm max}$ is the velocity of density peak, and $\boldsymbol{r}$ is the distance from the density peak. The central densities of the cores are $\rho = 8.0 \times 10^{-19}$g cm^{-3} (upper panel) and $\rho = 1.2 \times 10^{-18}$g cm^{-3} (lower panel). **Although a smooth rotation pattern can be seen in the upper panel of Figure 4.20, a complex velocity structure can be observed in the lower panel. In the lower panel, the rotation velocity pattern around the central region is different from the rotation velocity pattern of the outer region of the core.** This kind of complex rotation structure appears due to the combination of different phases of the initial turbulent velocity field. Figure 4.21 displays the angle between the rotation axis of the inner region and the outer shell both with the same mass. **Here, we define the inner region as the region enclosed by the outer shell. The color scale represents the angle between the rotation axis of the inner region and the outer shell averaged over all the cores.** Figure 4.21 indicates that the complexity of the angular momentum structure of the cores decrease with time. This trend also can be slightly seen in Figure 4.17. However, the outer shell of the core (~ 1 M$_\odot$) has relatively large inclination even at the final stage of our simulation as shown in Figure 4.21. This is because the outer shell of the core does not have enough time to transfer its large angular momentum during the runaway collapse phase. Figure 4.22 shows **histograms of the angles between the angular momentum of the inner region with mass** 0.02 M$_\odot$ **and that of the outer shell with the same mass for 38 cores at the initial state (left) and at the final state (right) with statistical error bars.** These histograms also show that the complexity of the core angular momentum structure decreases as time progresses.

While the complexity of the rotation of the inner region decreases with time, Figure 4.22 shows that the complexity of the rotation still remains at the final state of our simulation, just before the first core formation. Therefore, this kind of complex angular momentum structure might be related to the observed warped (or misaligned) disk around the protostar (e.g., Sakai et al., 2019). In future, we will perform the long term and high resolution simulations to form such misaligned disks.

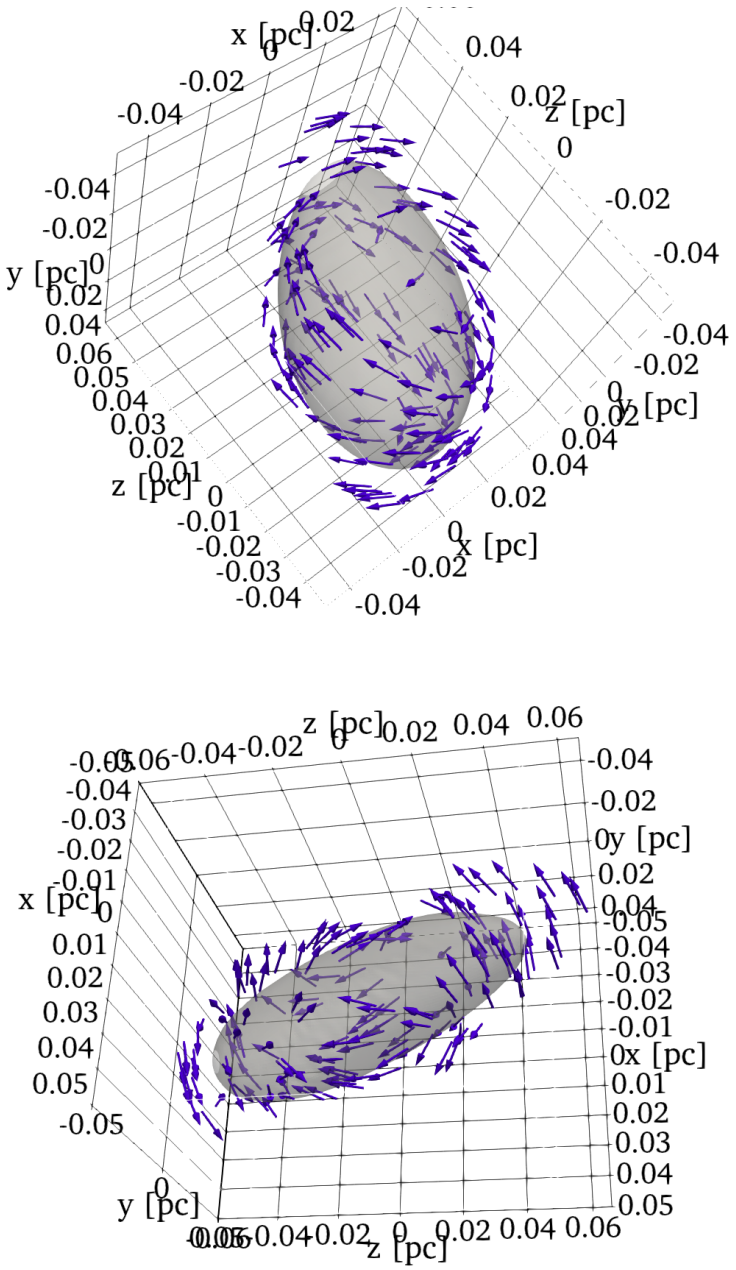

Figure 4.20: 3D plots of the velocity structure in cores formed in our simulations. The upper and lower panels are smooth and complex velocity structure cases, respectively. The isosurfaces represent the isodensity surfaces, $\rho = 3.0 \times 10^{-19}$g cm^{-3} ($n = 7.8 \times 10^4$cm^{-3}) (upper panel) and $\rho = 3.5 \times 10^{-19}$g cm^{-3} ($n = 9.1 \times 10^4$cm^{-3}) (lower panel). The blue arrows are the direction of the rotation velocity. The central densities of the cores are $\rho = 8.0 \times 10^{-19}$g cm^{-3} ($n = 2.0 \times 10^5$cm^{-3}) (upper panel) and $\rho = 1.2 \times 10^{-18}$g cm^{-3} ($n = 3.1 \times 10^5$cm^{-3}) (lower panel)

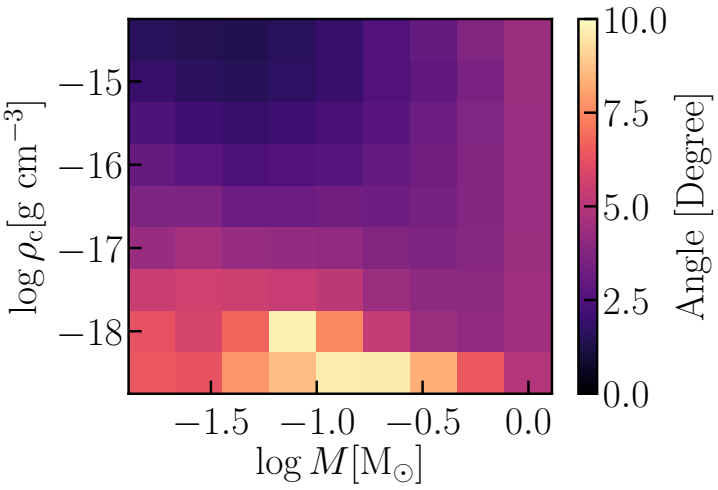

Figure 4.21: Angle between the angular momentum vector of the inner region and the outer shell with the same mass as the inner region. **Here, we define the inner region as the region enclosed by the outer shell. The color scale represents the angle between the rotation axis of the inner region and the outer shell averaged over all the cores.** The horizontal axis is the total mass within the shell. The vertical axis is the maximum density of a core.

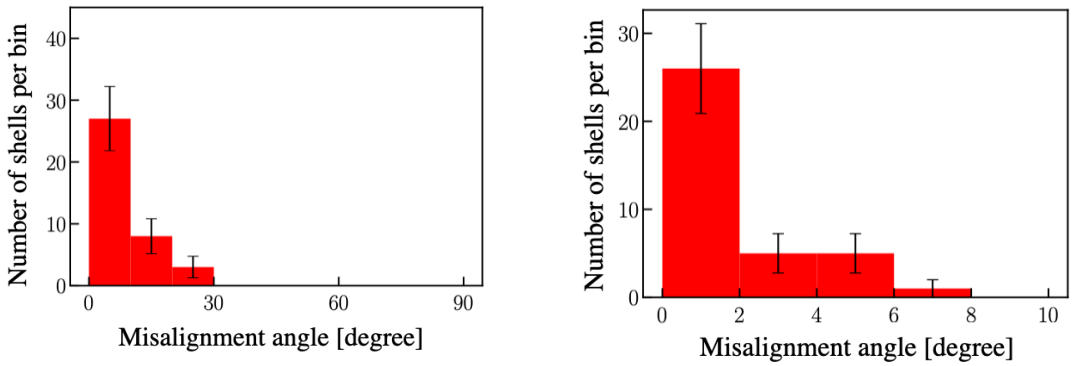

Figure 4.22: **Histograms of the angles between the angular momentum of the inner region with mass** 0.02 M$_\odot$ **and the outer shell with the same mass for 38 cores at the initial state (left) and at the final state (right) with statistical error bars.** Note that the scales of the x-axis are not the same on both panels.

4.2.5 Angular Momentum in the Central Region of the Cores

In this subsection, we analyze the central high density region of the cores. In this analysis, the central high density region is defined as the gas with $\rho > 0.1\rho_{\rm max}$. The rotation and shape of the central high density region of a core are important for the formation of multiple systems (Matsumoto & Hanawa, 2003; Machida et al., 2005) and the subsequent formation of protostar-disk systems. We calculate the angular momentum and moment of inertia of the central region of a core as follows:

$$\boldsymbol{J}_{01} = \sum_{i,\rho_i > 0.1\rho_{\rm max}} m_i(\boldsymbol{x}_i - \boldsymbol{x}_{01,\rm c}) \times (\boldsymbol{v}_i - \boldsymbol{v}_{01,\rm c}), \tag{4.21}$$

and

$$I_{ln,01} = \sum_{i,\rho_i > 0.1\rho_{\rm max}} m_i[(\boldsymbol{x}_i - \boldsymbol{x}_{01,\rm c})^2\delta_{ln} - (x_{l,i} - x_{l,01,\rm c})(x_{n,i} - x_{n,01,\rm c})], \tag{4.22}$$

$\boldsymbol{x}_{01,\rm c}$ and $\boldsymbol{v}_{01,\rm c}$ are the position and velocity of the center of mass of the core central region. We also estimate the angular speed of the core central region as follows:

$$\omega_{01,l} = \sum_n I^{-1}_{01,ln} J_{01,n}, \tag{4.23}$$

where $I^{-1}_{01,ln}$ is the inverse matrix of $I_{01,ln}$. Figure 4.23 displays the time evolution of the normalized angular speed of the central region, $\tilde{\omega}_{01} = \omega_{01} t_{\rm ff}$, where $t_{\rm ff} = 1/\sqrt{4\pi G\rho_{\rm c}}$ is the free fall time of the central region at each time step. The vertical axis is the normalized angular velocity of the central region of a core. The horizontal axis is the maximum density of the core. The different colors of solid lines correspond to the different cores. The black dashed line is $\omega \propto \rho_{\rm c}^{1/6}$, which corresponds to the growth rate of $\tilde{\omega}_{01}$ discussed in Hanawa & Nakayama (1997). **In Hanawa & Nakayama (1997), they did the linear analysis for Larson-Penston solution and found that there is a spin-up mode which can grow slowly in self-similar collapse.** Figure 4.24 is the histogram of $\tilde{\omega}_{01}$ at the final state. Figure 4.24 shows that the peak position of the histogram is $\tilde{\omega}_{01} \sim 0.2$. This result indicates that the central region of the cores converges to the self-similar solution characterized by a rotation consistent with the values discussed in Matsumoto et al. (1997) and Matsumoto & Hanawa (2003).

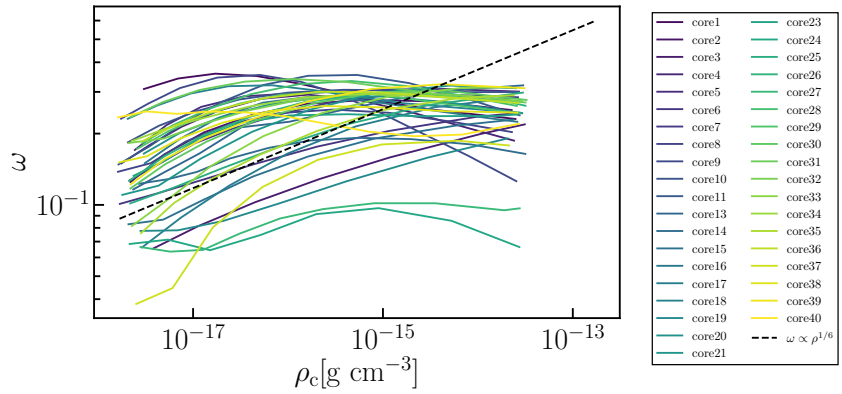

Figure 4.23: Time evolution of the angular velocity derived from Equation 4.23. The vertical axis is the normalized angular velocity of the central region of the cores. The horizontal axis is the maximum density of the cores. The different colors of the solid lines correspond to the different cores. The black dashed line is $\omega \propto \rho_c^{1/6}$ discussed in Hanawa & Nakayama (1997).

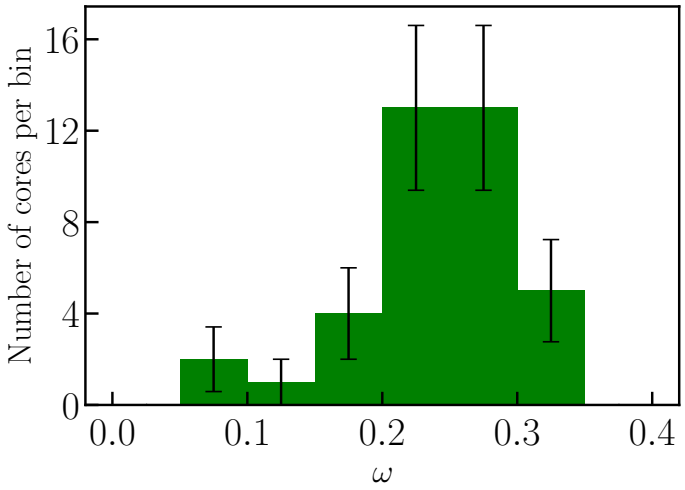

Figure 4.24: Histogram of angular velocity derived from Equation 4.23. The horizontal axis is the normalized angular velocity of the central region of the cores. The error bars refer to the standard deviation.

4.3 Discussion

4.3.1 An Origin for the Specific Angular Momentum Profile in a Core

As shown in Section 4.2.4 and 4.2.5, the rotation profile in the cores converges to the self-similar solution, $j \propto M$. As discussed in Saigo & Hanawa (1998), the self-similar solution with rotation can be derived analytically by assuming the geometrically thin disk and symmetry around the rotation axis (see also **Basu (1997)**). **Saigo & Hanawa (1998) found that if the normalized rotation parameter satisfies the condition $jc_{\rm s}/GM < 0.5$, the self-similar solution with rotation can be exist because the gravity can overcome the centrifugal force.** The origin of the $j \propto M$ relation can be understood as follows. The mass of the central high density region is given by

$$M \sim \rho_{\rm c}\lambda^3 \propto \rho_{\rm c}^{-1/2}, \tag{4.24}$$

where λ is the Jeans length of the central region. The specific angular momentum of the central region can be estimated as follows:

$$j \sim \lambda^2\omega \propto \rho_{\rm c}^{-1/2}, \tag{4.25}$$

where we used $\omega \propto \rho_{\rm c}^{1/2}$. This is because the time scale of the system is only the free-fall time. Using Equation 4.24 and 4.25, we can derive

$$j \propto M. \tag{4.26}$$

The radial extent of the region in which the $j \propto M$ scaling is expected is determined by whether $\tilde{\omega}$ is larger than 0.2 or not. Matsumoto et al. (1997) shows that $\tilde{\omega}$ increases due to the spin up during the collapse and eventually it reaches $\tilde{\omega} = 0.2$. Once it reaches $\tilde{\omega} = 0.2$, $\tilde{\omega}$ remains constant although some oscillations can be observed in Figure 4.24 and in Matsumoto et al. (1997). To estimate the radial extent of $j \propto M$ scaling, it is important to know when $\tilde{\omega}$ is saturated since we used $\omega \propto \rho_{\rm c}^{1/2}$ to derive Equation 4.26. In Figure 4.23, $\tilde{\omega} \sim 0.1$ even at the early stage of the collapse ($\rho_{\rm c} \sim 10^{-18}$ g cm^{-3}). Hence, for simplicity, the radial extent of $j \propto M$ scaling is estimated from the intersection of the self-similar profile ($j \propto M$) and j-M profile at the initial state. At initial state, we can estimate the specific angular momentum as follows. The specific angular momentum of the core gained from the initial Kolmogorov turbulent velocity field at the initial state is written as

$$j = \frac{2}{5}\sigma(R)R, \tag{4.27}$$

where $\sigma(R)$ is velocity dispersion and the factor comes from the inertia moment. In Equation 4.27, we assume the uniform density, $\rho_{\rm c0}$. This

assumption is justified since we focus on the small mass scale ($< 1\mathrm{M}_\odot$). In small mass scale, the equilibrium profile of the filament has flat density region. After some calculations, we can derive the specific angular momentum profile at the initial state as follows:

$$j = 3.5 \times 10^{20}\mathrm{cm}^2\ \mathrm{s}^{-1} \left(\frac{\sigma_0}{0.2\ \mathrm{km\ s}^{-1}}\right) \left(\frac{M}{\mathrm{M}_\odot}\right)^{4/9}, \tag{4.28}$$

where we used $\sigma(R) = \sigma_0(R/1.6\ \mathrm{pc})^{1/3}$ and $M = 4\pi\rho_{c0}R^3/3$. We adopt $\sigma_0 = 0.2\ \mathrm{km\ s}^{-1}$. The self-similar profile can be roughly estimated as follows:

$$j = \frac{2}{5}R^2\omega. \tag{4.29}$$

Using $\omega = 0.2\sqrt{4\pi \mathrm{G}\rho_\mathrm{c}}$ and the surface density $\Sigma = \sqrt{2c_\mathrm{s}^2\rho_c/\pi G}$, we can derive the self-similar profile,

$$j = 6.3 \times 10^{20}\mathrm{cm}^2\ \mathrm{s}^{-1} \left(\frac{M}{\mathrm{M}_\odot}\right). \tag{4.30}$$

The intersection of Equation 4.28 and Equation 4.30 gives us the boundary of self-similar solution (radial extent), $M_\mathrm{ss} = 0.26\ \mathrm{M}_\odot$. This is compatible with the result shown in Figure 4.15.

4.3.2 Effect of Filamentary Structure on the Angular Momentum of Cores

As discussed in Chapter 1, Observations show that the filamentary structure is ubiquitous in molecular clouds, and the molecular cloud cores along the filaments. This indicates that the cores (i.e., stars) are formed in the filamentary structures. This scenario is often called "filament paradigm". In this subsection, we summarize the role of filament paradigm in the evolution of the angular momentum of cores.

In Section 4.2.4 and 4.3.1, we discussed the convergence of internal angular momentum profile to the self-similar solution.This tendency has been already reported in, for example, Matsumoto & Hanawa (2003) in which they adopted the spherical core as the initial condition. Therefore, our results about the internal angular momentum profile agree with the previous works although we adopt the filamentary molecular cloud with subsonic (transonic) turbulent velocity field as the initial condition.

On the other hand, the direction of the angular momentum of cores is affected by filament geometry. As shown in Section 4.2.3, the rotation direction of the cores tend to be perpendicular to the longitudinal axis

of the filament since the initial shape of cores is elongated to the longitudinal axis of the filament. In observations, the relation between the rotation axis of a core and the filament axis is studied by using the angle between the outflow and the filament axis. For example, Kong et al. (2019) reported that the outflow orientation tends to be parpendicular to the filament axis using Atacama Large Millimeter/submillimeter Array (ALMA) CO(2-1) observations in G28.37+0.07 . However, Stephens et al. (2017) and Baug et al. (2020) claimed that the outflow is randomly oriented with respent to the filament axes using CARMA-NRO Orion survey data and ALMA, respectively. In Feddersen et al. (2020), they showed that the distribution of the angle between the outflow and the filament axis is a random distribution in the full sample of outflows using CARMA-NRO Orion survey data. However, they also showed that the outflow direction is moderately perpendicular to the filament axis in the most reliable subsample. Hence, the observations of distribution of the angle between the outflow and the filament axis is still under debate. In addition, Machida et al. (2020) investigated the effect of misalignment of the initial rotation axis of core with respect to the initial magnetic field and showed that the outflow direction changes with time. These theoretical studies indicate that we cannot simply derive the angle between the rotational axis and filament axis using the data of the angle between the outflow direction and the filament axis. Studying the relation between the outflow direction and the filament axis is our future work. Note that the anisotropy of turbulent velocity field in a filament might affect the rotation direction of a core with respect to the filament axis. As discussed in Misugi et al. (2019), the anisotropy of turbulent velocity field in filaments might be created since the filaments are formed by large scale compression perpendicular to the filament axis (e.g., Arzoumanian et al., 2018; Inoue et al., 2018; Abe et al., 2021). It is expected that the waves perpendicular to the filament axis has larger energy than the waves parallel to the filament axis. This anisotropy leads to increase the parallel rotation with respect to the filament axis compared with isotropic velocity field. Therefore, studying the anisotropy of velocity turbulent field in filament formation simulation and observations is important for the distribution of the rotation axis of cores.

Observations show that the radial density profile of the filaments has shallower slope compared with the equilibrium profile (e.g., Arzoumanian et al., 2011). The different density profile might affect the direction of the angular momentum of the cores. If we adopt the shallower density profile, the cores would have slightly larger parallel component of the angular momentum with respect to the filament axis compared with the case of the equilibrium profile. This effect might be small since the mass of filament still concentrate on the main axis of the filament and the cores can accumulate their mass along the filament even if the filament has shallower radial density profile. Although this effect should

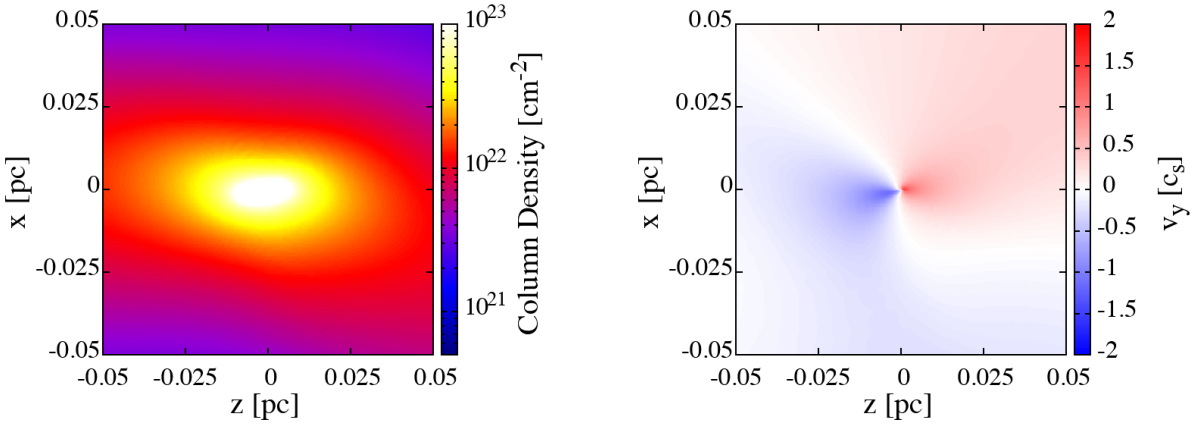

Figure 4.25: Column density map (left) and line-of-sight velocity map (right) around the core at the final state of the simulation. **In these plots, the longitudinal axis of the filament is parallel to the plane of sky.**

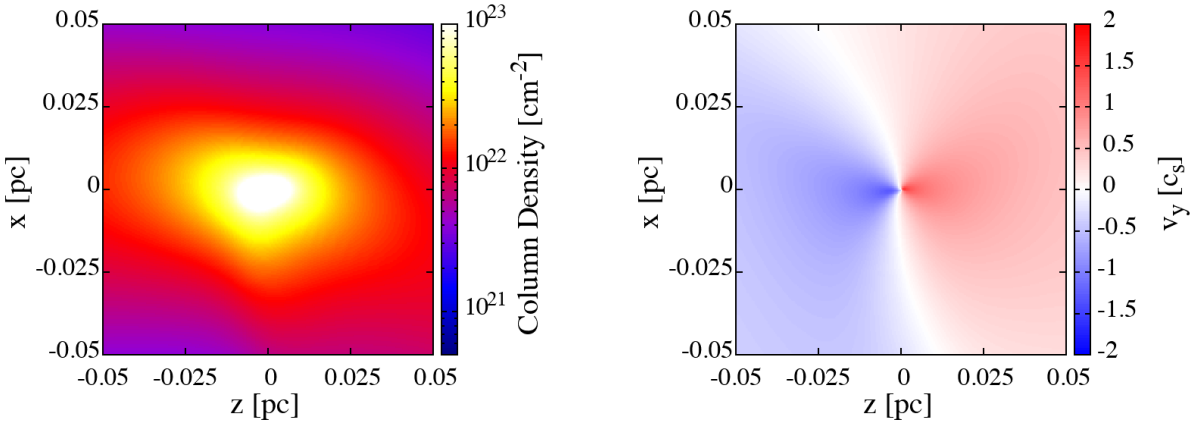

Figure 4.26: Same as Figure 4.25 for the case where the filament is inclined by 30° with respect to the plane of the sky.

be estimated quantitatively, this is out of the scope of the paper.

4.3.3 Comparison with Observations

In the previous section, we derived various properties of the three-dimensional angular momentum of the cores. However, in observations, the specific angular momentum is measured using the line-of-sight velocity in two-dimensional plane (Goodman et al., 1993; Caselli et al., 2002; Tatematsu et al., 2016; Punanova et al., 2018). To mimic a line-of-sight velocity map, we integrate the velocity along the line-of-sight direction as follows:

$$v_{\rm los}(x,z) = \frac{1}{\Sigma(x,z)} \int \rho v_{\rm y} dy, \tag{4.31}$$

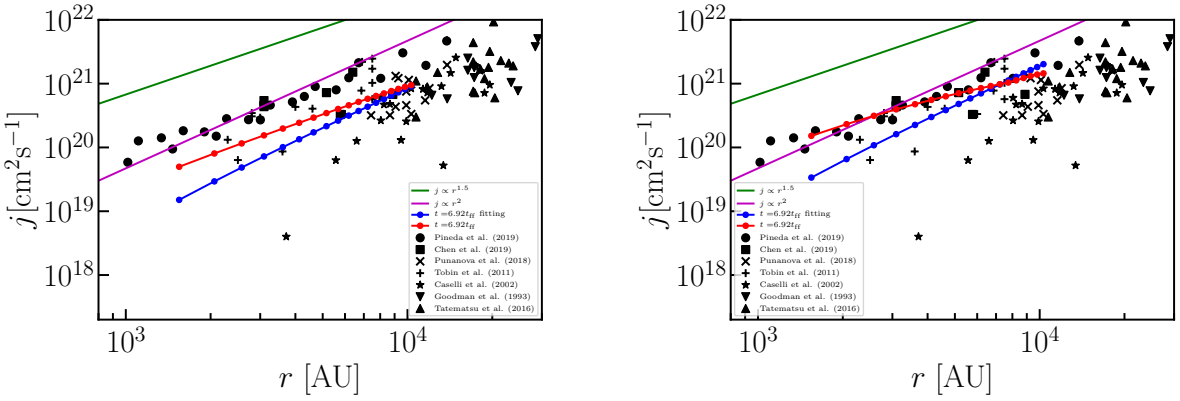

Figure 4.27: Relation between the specific angular momentum and the radius from the core center. The red solid line is the relation between specific angular momentum and radius from core center derived from the line-of-sight velocity map. The blue solid line is result from the rigid body rotation fitting using Equation 4.33. The left and right panels are for not-inclined and for inclined model, respectively. The black dots are the observation data. The circles, squares, crosses, pluses, stars, down-triangles, and up-triangles are observational data from Pineda et al. (2019), Chen et al. (2019a), Punanova et al. (2018), Tobin et al. (2011), Caselli et al. (2002), Goodman et al. (1993), and Tatematsu et al. (2016). The green and purple solid lines are $j \propto r^{1.5}$ and $j \propto r^2$ just for comparison.

where $\Sigma(x, z)$ is the column density defined as

$$\Sigma(x, z) = \int \rho dy. \tag{4.32}$$

Figure 4.25 displays the resultant column density and mean velocity maps. The left panel of Figure 4.25 is the column density map calculated using Equation 4.32, and the right panel of Figure 4.25 is the mean velocity map derived from Equation 4.31. **In these plots, the longitudinal axis of the filament is parallel to the plane of sky.** Though we mimic the observation of the core specific angular momentum below, the longitudinal axis of the filament (z-axis) is not always parallel to the plane of the sky. For this reason, we also show the column density and mean velocity maps in Figure 4.26 by rotating the filament around the x-axis by 30°. Using the mean velocity map, we derive the two-dimensional specific angular momentum **as follows**. First, we fit the mean velocity map using the following equation:

$$v_{\rm los,fit}(x, z) = v_{\rm c,fit} + \Omega_x z - \Omega_z x, \tag{4.33}$$

where $v_{\rm c,fit}$, Ω_x, and Ω_y are the free parameters of the fitting. **This fitting method is used in a lot of previous works** (Goodman et al., 1993; Caselli et al., 2002; Tatematsu et al., 2016; Punanova et al., 2018). We determine these parameters **by minimizing**

$$\sigma_{\rm error} = \int\int (v_{\rm los}(x, z) - v_{\rm los,fit}(x, z))^2 dx dz. \tag{4.34}$$

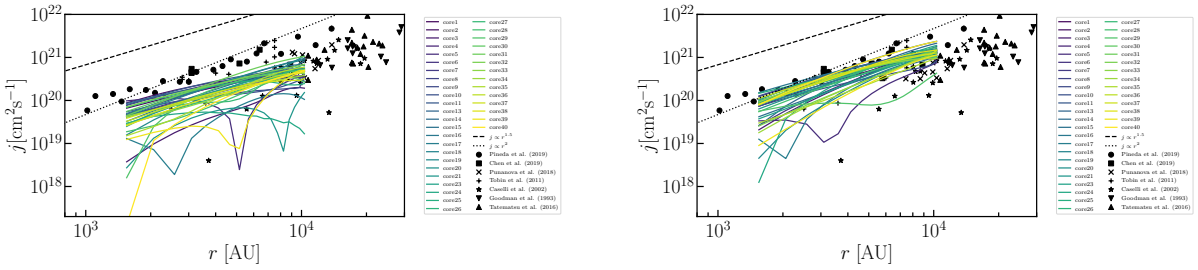

Figure 4.28: j-r relation for all cores. The different colors correspond to the different cores. The others are same as Figure 4.27.

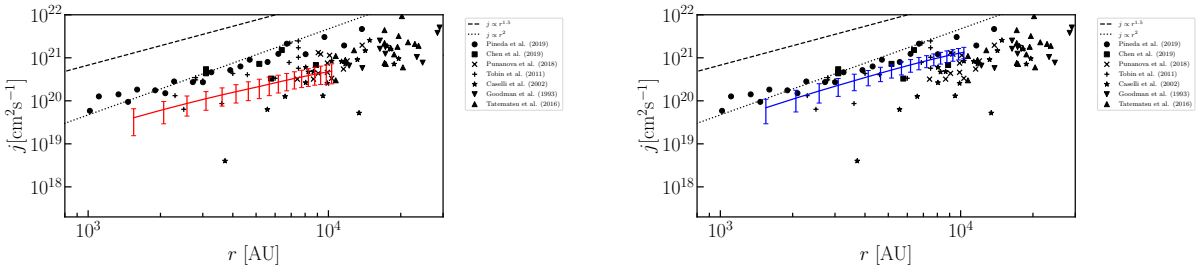

Figure 4.29: Averaged j-r relation for without the inclination (left) and with inclination(right). The error bars refer to the standard deviation. The others are same as Figure 4.27.

Next, we calculate $\theta_{\rm 2d,fit} = \arctan\left(\Omega_z/\Omega_x\right)$ and define $\theta_{\rm 2d,fit}$ as the core rotational axis. Then, we measure the distance R from the rotational axis. Finally, we calculate the average angular momentum in each dR bin. The results are shown in Figure 4.27. The red solid line is the relation between the specific angular momentum and the distance from the rotation axis derived from the line-of-sight velocity map. The blue solid line is the result from the rigid body rotation fitting using Equation 4.33. The left and right panels are for not-inclined and inclined models, respectively.

Figure 4.29 displays the averaged j-r relation for all cores shown in Figure 4.28 without inclination (left) and with inclination (right). The error bars refer to the standard deviation. We also derived the total specific angular momentum in the line-of-sight velocity map as follows:

$$j_{\rm 2d} = \frac{2}{5} r_{\rm core}^2 \Omega, \tag{4.35}$$

here we use $r_{\rm core} = 0.05$ pc for simplicity, and $\Omega = \sqrt{\Omega_x^2 + \Omega_z^2}$ derived from the fitting using Equation 4.33 and Equation 4.34. $j_{\rm 2d}$ is compared with the observational results in Figure 4.30. Figure 4.28, 4.29, and 4.30 show that the observed absolute value of the specific angular momentum and the slope index of the j-r relation in the filaments with inclination are larger than without inclination. This is due to the accretion onto the cores along the filaments. To confirm this, we

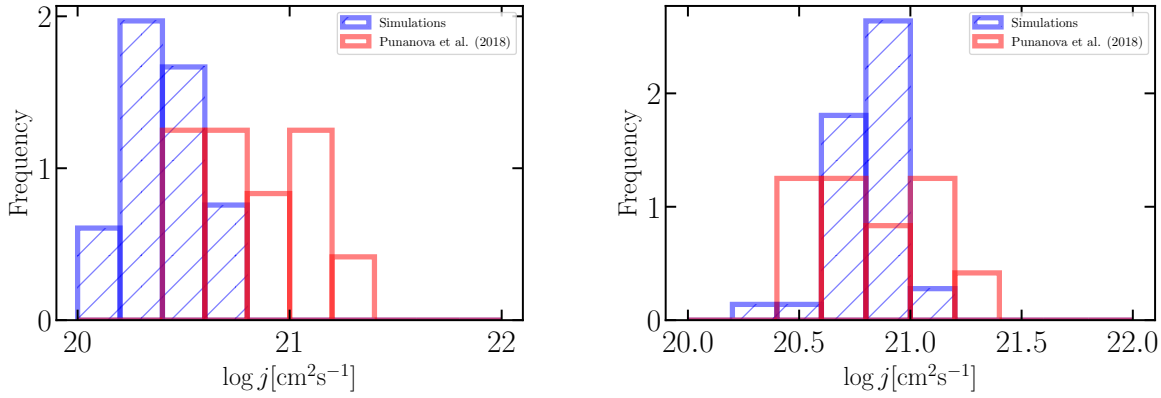

Figure 4.30: Comparison of j_{2D} to the observational data. The left and right panels are for not-inclined and for inclined models, respectively. The blue and red histograms are distributions of j_{2d} and measured specifinc angular momentum in Punanova et al. (2018).

run the simulation in which the filament has only the z-component of fluctuations, $k_z = 2\pi/(0.4\text{pc})$, at initial state. We stop the simulation just before the first core formation, and then we measure the angular momentum using the same analysis. The result with inclination by 30° is shown in Figure 4.31. The blue solid line is the averaged j-r relation with inclination of the filament. The purple solid line is the j-r relation with only fluctuations along the z-axis. Figure 4.31 shows that, with the inclination, the accretion onto the core affects the observed j-r relation. To investigate this effect in more detail, we also calculate the mean velocity map changing the minimum core density. The mean velocity map is derived from only SPH particles with density larger than the minimum core density. The dependence of the effect of accretion along the filament axis on the apparent measured rotation observed on the mean velocity map is shown in Figure 4.32. The vertical axis is the ratio of angular momentum of core measured in the mean velocity map with inclination to that without inclination. **Please note that the core definition adopted here differs from that used in Section 4.2.2.** Figure 4.32 clearly shows that the contamination from the accretion along the filament decreases with the minimum density to calculate the mean velocity map. In high density regions, the flow tends to be spherical accretion rather than accretion along the filament longitudinal axis.

Figure 4.33 shows that the time evolution of the angular momentum observed in the line-of-sight velocity map, for example Figure 4.25 and 4.26. **In this plot, we measure the 2d angular momentum in the line-of-sight velocity map whose area is 0.05pc × 0.05pc at each time step. Note that, since the size of area of the line-of-sight velocity map is fixed in this measurement, the mass contained in the region increases with time.** The horizontal axis is the maximum density of the core, and the vertical axis is the specific angular momentum measured in line-of-sight velocity maps. The solid line is the specific angular momentum evolution that is averaged over all cores. The red and blue

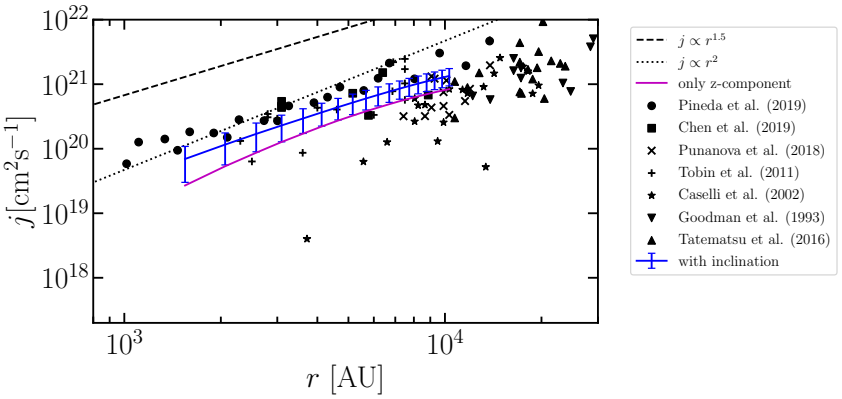

Figure 4.31: Effect of accretion onto cores on j-r diagram. The blue solid line is the averaged j-r relation with inclination of the filament. The purple solid line is j-r relation with only z-component of fluctuations. The others are same as Figure 4.27.

solid lines are the results with the inclination and without inclination, respectively. Figure 4.33 shows that the observed angular momentum of the cores increases with time. This is because the gas with larger angular momentum accretes onto the core at later stages.

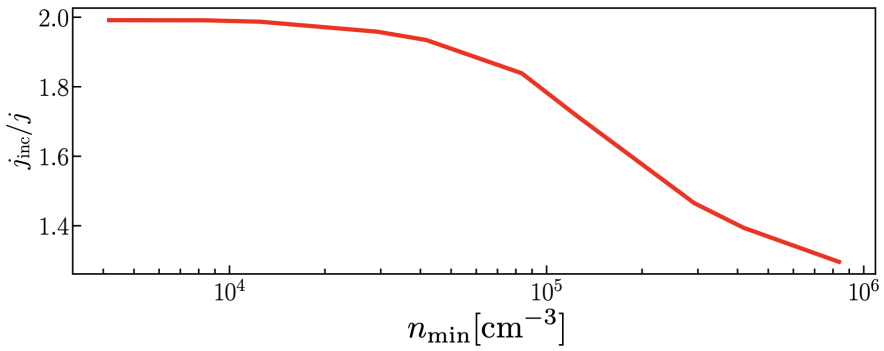

Figure 4.32: Effect of accretion along the filament axis on the apparent measured angular momentum of the core. The vertical axis is the ratio of the core angular momentum measured in the line of sight velocity map with inclination with respect to that without inclination. The horizontal axis is the **minimum** density for the definition of core. **Please note that the core definition adopted here differs from that used in Section 4.2.2.**

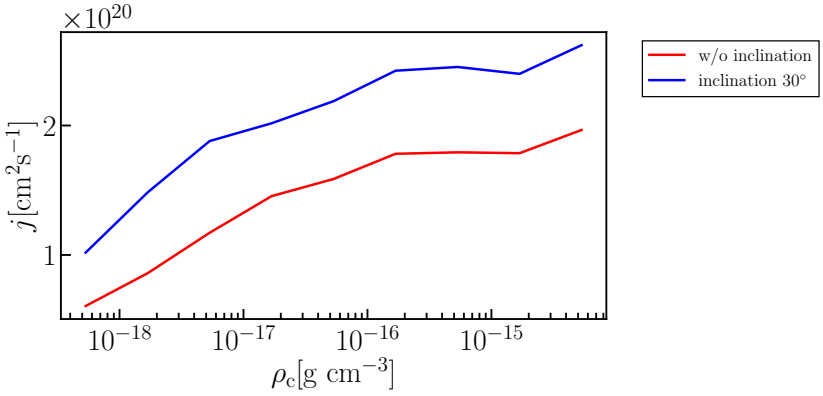

Figure 4.33: Averaged time evolution of specific angular momentum measured in line-of-sight velocity maps such as Figure 4.25 and 4.26. **In this plot, we measure the 2d angular momentum in the line-of-sight velocity map whose area is 0.05pc $\times$ 0.05pc at each time step. Note that, since the size of area of the line-of-sight velocity map is fixed in this measurement, the mass contained in the region increases with time.** The horizontal axis is the maximum density of the core, and the vertical axis is the specific angular momentum measured in line-of-sight velocity maps. The solid line is the specific angular momentum evolution that is averaged over all cores. The red solid line and blue solid line are the results with the inclination and without inclination, respectively.

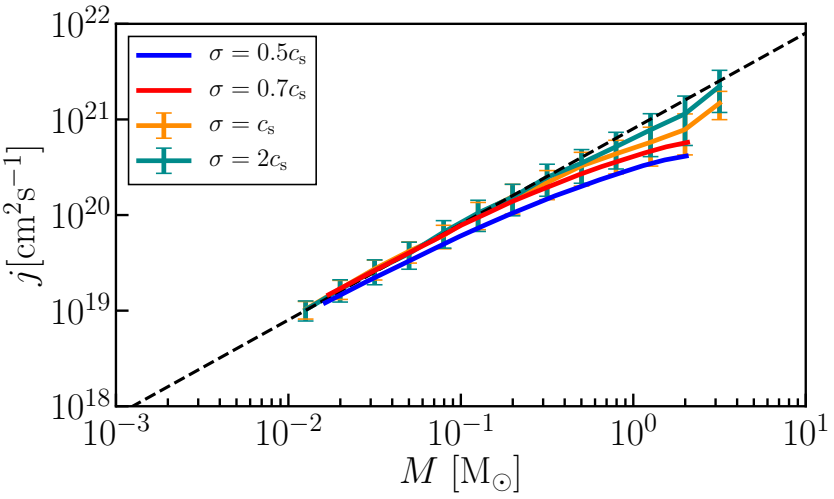

Figure 4.34: Comparison of averaged j-M profile. The blue, red, orange, and green solid lines are j-M relations with $\sigma = 0.5c_\mathrm{s}$, $\sigma = 0.7c_\mathrm{s}$, $\sigma = c_\mathrm{s}$, and $\sigma = 2c_\mathrm{s}$, respectively. The black dashed line is $j \propto M$.

4.3.4 Dependence on the Turbulence of the Velocity Field

In this subsection, we discuss the dependence of the results shown in the previous section on the initial velocity dispersion of turbulence. **First, we discuss the dependence of the j-M relation on the initial 3D turbulent velocity dispersion σ in the filament.** Figure 4.34 displays the comparison of averaged j-M profile. The blue, red, orange, and green solid lines are j-M relations with $\sigma = 0.5c_\mathrm{s}$, $\sigma = 0.7c_\mathrm{s}$, $\sigma = c_\mathrm{s}$, and $\sigma = 2c_\mathrm{s}$, respectively. Figure 4.34 shows that, with larger initial velocity dispersion, **a wider portion of the j-M profile converges to the self-similar solution.** Figure 4.35 displays the comparison of the observed j-r relation without inclination of filament (left) and with inclination of filament (right). Figure 4.35 clearly shows that larger specific angular momentum is observed in the filaments with larger initial velocity dispersion.

4.3.5 Properties of Cores Defined by Density Contours

So far, we use only one core from each filament to compare the core properties at the same evolutionary stage of the cores. However, in reality, we observe all cores formed in each filament. In this subsection, we show the properties of all cores formed in the filaments at the same evolutionary stage of the filaments using the same density contour value in all simulations. The cores shown in this subsection have different masses. **By adopting 1 ρ_c as the minimum density for the definition of core, we identify 115, 124, 101, and 52 cores at 2, 3, 4, and 5 t_ff, respectively. For the case of $2\rho_\mathrm{c}$, we identify 51, 79, 93, and 45 cores at 2, 3, 4, and 5 t_ff, respectively. When we choose much higher density threshold, 3 ρ_c, we identify 20, 44, 69, and 39 cores at 2, 3, 4,**

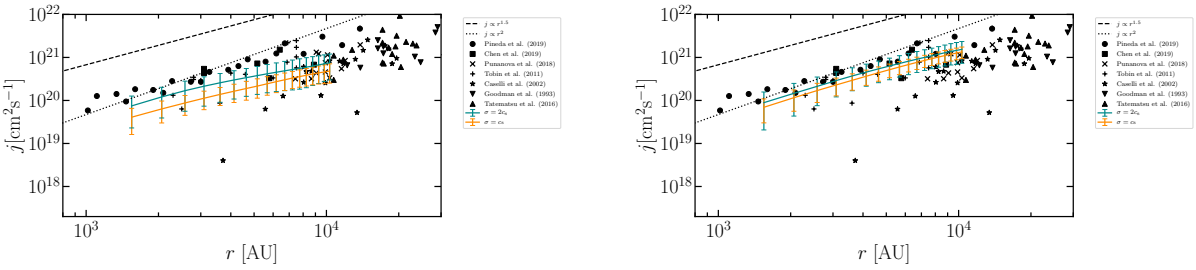

Figure 4.35: Comparison of the observed j-r relation without inclination of filament (left) and with inclination of filament (right). The orange and green solid lines are observed j-r relations with $\sigma = c_{\rm s}$ and $\sigma = 2c_{\rm s}$, respectively. The black dashed line and dotted line are $j \propto r^{1.5}$ and $j \propto r^2$ just for comparison.

and 5 $t_{\rm ff}$, respectively. The reason why the number of core is small at 5 $t_{\rm ff}$ is that we stop the simulations when the maximum density of the core reaches the first core formation density. Some of the simulations finish before 5 $t_{\rm ff}$.

Figure 4.36 displays j-M diagram for all cores in our simulations. The vertical axis and horizontal axis are the specific angular momentum and the mass of core, respectively. The red, blue, green, and magenta symbols represent the cores defined at $t = 2, 3, 4$, and 5 $t_{\rm ff}$, respectively. The plus, star, and circle symbols represent the critical density used for definition of core ($1, 2$, and $3\rho_{\rm c}$). The black dots are observational data. The black dashed line is $j \propto M$. The black solid line is fitting result for all cores in the simulations. The fitting result is $j \propto M^{0.72\pm0.02}$. Figure 4.37 is the j-R diagram for all cores in our simulations. The vertical axis and horizontal axis are the specific angular momentum and the radius of core, respectively. The black dashed line and dotted line are $j \propto R^{1.5}$ and $j \propto R^2$, respectively. The fitting result is $j \propto R^{2.02\pm0.04}$. Figure 4.38 shows β-M diagram for all cores in our simulations. $\beta = R^3\Omega^2/3GM$ **is the ratio of the rotational energy to the gravitational energy (e.g., Belloche, 2013b).** Ω **is calculated by Equation 4.33.** The fitting result is $\beta \propto M^{0.18\pm0.02}$. These slope values are different from the results obtained in Section 4.2.4, especially for j-R diagram. In Figure 4.36, 4.37, and 4.38, since we plot all cores found in our 40 filaments at the same elapsed time of the simulation ($t = 2, 3, 4$, and $5t_{\rm ff}$), we observe the cores at different evolutionary stage (different central maximum density). That is why we find the steeper slope in Figure 4.37 compared to that in Figure 4.16 which shows internal j-r profile.

Figure 4.39 is a histogram of ratio of specific angular momentum derived from line-of-sight velocity map to that measured in 3D. The horizontal axis is logarithmic. Dib et al. (2010) claims that the specific angular momentum is overestimated by an order of magnitude when measured from the line-of-sight velocity map, although Zhang et al. (2018) pointed out that the specific angular momentum is underestimated by a factor of 2 or 3 in synthetic observations. Our result shown in Figure 4.39 supports the results in Zhang et al. (2018). The average and standard deviation of the distribution shown in Figure 4.39 are 0.49 and 0.55, respectively.

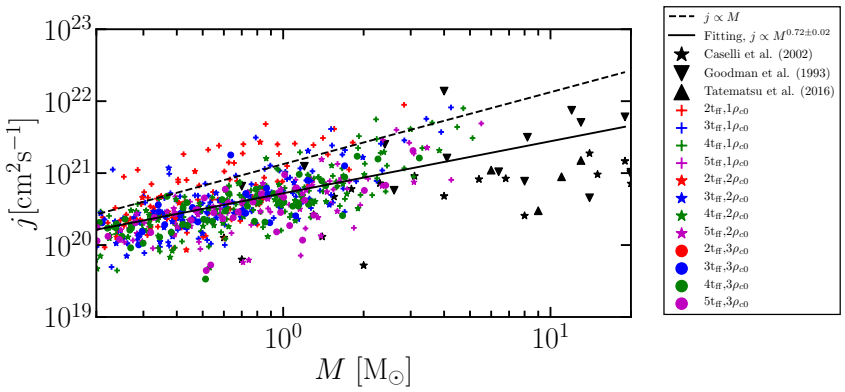

Figure 4.36: j-M diagram for all cores in our simulations. The vertical axis and horizontal axis are the specific angular momentum and the mass of core, respectively. The red, blue, green, and magenta symbols represent the cores defined at $t = 2, 3, 4$, and 5_tff, respectively. The plus, star, and circle symbols represent the critical density used for definition of core ($1, 2$, and $3\rho_{\rm c}$). The black dots are observational data. The black dashed line is $j \propto M$. The black solid line is fitting result for all cores in simulations. The fitting result is $j \propto M^{0.72\pm0.02}$.

This is because we cannot observe the component of the angular momentum parallel to the line-of-sight-direction. This effect leads to an underestimation of the angular momentum.

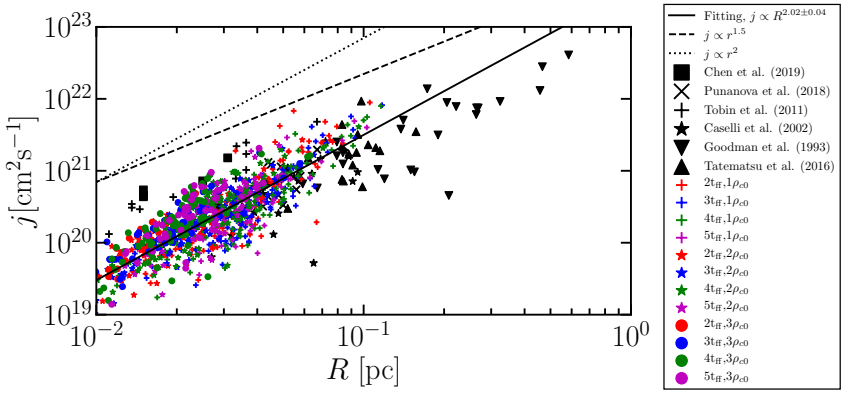

Figure 4.37: j-R diagram for all cores in our simulations. The vertical axis and horizontal axis are the specific angular momentum and the radius of core, respectively. The black dashed line and dotted line are $j \propto R^{1.5}$ and $j \propto R^2$, respectively. The fitting result is $j \propto R^{2.02\pm0.04}$.

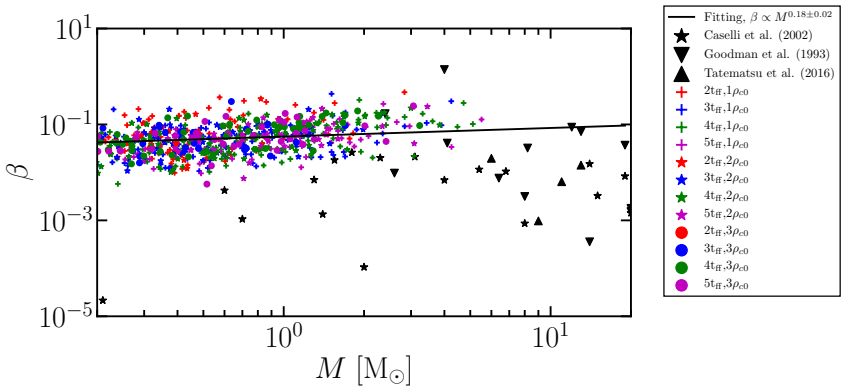

Figure 4.38: β-M diagram for all cores in our simulations. The fitting result is $\beta \propto M^{0.18\pm0.02}$.

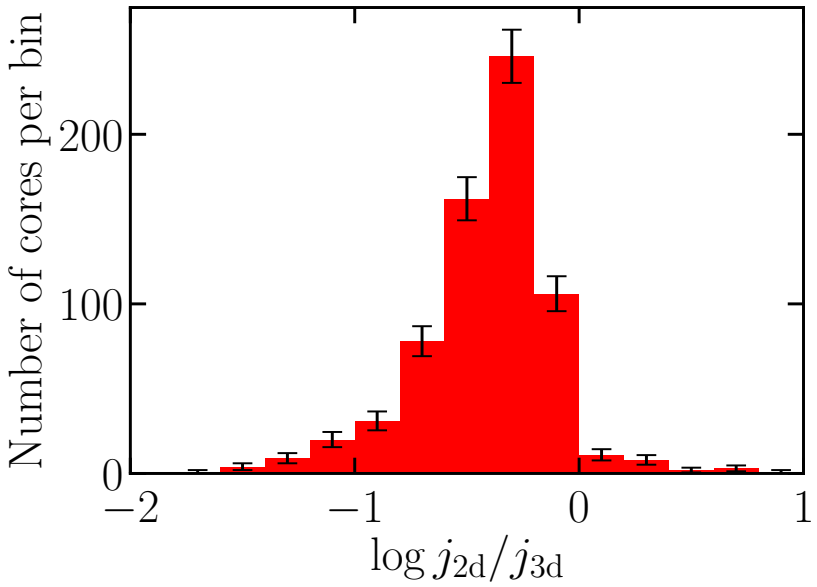

Figure 4.39: Histogram of ratio of specific angular momentum derived from line-of-sight velocity map to that measured in 3d. The horizontal axis is logarithmic.

4.4 Summary of this Chapter

In this paper we study the time evolution of core angular momentum using three-dimensional hydrodynamics SPH simulations. We find that a core tends to lose about 30% of the angular momentum initially gained from turbulent fluctuations by the time the maximum density of core reaches the density of a first hydrostatic core, $\rho_{\rm crit} = 2.8 \times 10^{-14}$g cm^{-3}. We also find that the rotation axis of most cores are nearly perpendicular to the filament axis. This is because the initial core shape is elliptical and its longer axis is along the filament axis. The analysis of the internal structure of the angular momentum of cores shows that the profile of angular momentum in the cores converges to the self-similar solution ($j \propto M$) with time. The region of the self-similar solution in the cores become wider with larger velocity dispersion in the initial filament. Moreover, the degree of complexity in the core slightly decreases with time. However, the complex velocity field survives even just before the first core formation. We also perform the observations of simulation results and find that the angular momentum properties of the cores measured in line-of-sight velocity map is compatible with the observations.

Chapter 5

Summary and Future Prospects

5.1 Summary of this Thesis

The angular momentum of molecular cloud cores plays an essential role in the star formation process, for example, driving the outflow/jet, prompt the formation of multiple formation, and formation of protoplanetary disk. Recent observation shows that the filamentary structure is ubiquitous in the molecular clouds, so the molecular cloud cores should be formed in filamentary molecular clouds (André et al., 2010). However, the origin and detailed evolution of angular momentum of molecular cloud cores are still unclear. In this thesis, we investigate the origin and detailed evolution of angular momentum of molecular cloud cores formed through the filament fragmentation process.

First, we investigate an origin of the angular momentum of molecular cloud cores formed through filament fragmentation process. To do so, we study the relation between the velocity field and the resultant angular momentum of core semi-analytically. Our results show that Kolmogorov velocity power spectrum model can reproduce the observed angular momentum of cores. The anisotropic velocity fluctuations model can also reproduce the observed angular momentum of cores. We stress that the amplitude of velocity fluctuations of our model is subsonic (transonic). This is consistent with observations of velocity fluctuations (Hacar & Tafalla, 2011; Hacar et al., 2016). Inutsuka (2001) shows that, if the line mass fluctuations along the filaments follows Kolmogorov power spectrum, Salpeter slope of core mass function can be reproduced using Press-Schechter formalism. Therefore, we can explain the mass distribution and angular momentum distribution of core if we adopt Kolmogorov turbulence as initial condition.

Next, we investigate whether our Kolmogorov turbulence model is consistent with filament formation simulations or not. Using data from Inoue et al. (2018) and Abe et al. (2021) that investigate the filament formation mechanism in inhomogeneous molecular cloud swept by shock wave, we identify the filament axis and derive the power spectra of line mass and velocity along the filament. The results of our analysis show that line mass and velocity power spectra along the filaments follow Kolmogorov power spectrum. In addition, observations support our results. Roy et al. (2015) measure the line mass power spectrum along the filements using Herschel data. Their result is also compatible with Kolmogorov

power spectrum. This indicates that the filament formation scenario can explain the mass distribution and angular momentum distribution of core.

Finally, since Misugi et al. (2019) assume the conservation of angular momentum to derive it analytically, we study the time evolution of angular momentum of molecular cloud core. To do so, we perform the three-dimensional simulations using smoothed particle hydrodynamics (SPH) method. As a result, we find that the angular momenta of cores change only by 30% in their formation process. We also find that most of the cores rotate perpendicular to the filament axis. In addition, we analyze the internal angular momentum structure of cores. Although the cores gain various angular momentum from the initial turbulent velocity fluctuations in the filament, the angular momentum profile in a core converges to the self-similar solution. We also show that the degree of complexity of the angular momentum structure in a core decreases over time. Moreover, we perform synthetic observation and show that the angular momentum profile measured from the mean velocity map is compatible with the observations. We also find the candidate of wide binary whose separation is $\sim$8000AU formed by adjacent cores in filaments.

In next section, we explain our future works.

5.2 Future Prospects

5.2.1 Effect of Magnetic field

While in reality the filaments are threaded by magnetic field (Sugitani et al., 2011; Palmeirim et al., 2013), our study have not yet included the effect of magnetic field. Although the magnetic field impact on the angular momentum transfer due to magnetic braking in the protostar formation phase, how much angular momentum is transferred by magnetic field in filament fragmentation phase is still unclear. The implementation of magnetic field in Godunov SPH has already been studied (Iwasaki & Inutsuka, 2011, 2013; Tsukamoto et al., 2013). By including the effect of magnetic field in our SPH code, we will investigate the role of magnetic field in angular momentum transfer during filament fragmentation. Moreover, while large scale magnetic field is perpendicular to the filament axis, recent observation show that the structure of core scale magnetic field is more complex and has kind of random distribution (Eswaraiah et al., 2021). Since our simulation include the effect of turbulence, this kind of complex magnetic structure is expected to be appear in core scale once we include the effect of magnetic field in our simulation. In addition, recently the angle between the filament axis and the outflow launched from protostar is often discussed in observational papers (Stephens et al., 2017; Kong et al., 2019; Feddersen et al., 2020; Baug et al., 2020). These observations show that the outflow direction is perpendicular or random with respect to filament axis, not parallel. This tendency is also investigated by our future calculations.

5.2.2 Formation of Multiple System

Statistical properties of multiple system should be also explained theoretically. For example, observations show that the mean separation of multiple system is weakly increasing function of mass (Duchêne & Kraus, 2013). There is no theory to explain the reason why this kind of statistical properties of multiple system are observed, so the theoretical explanation is not enough, especially for wide binary. Some numerical simulations reproduces the wide binary system (Li et al., 2018), but the formation mechanism is not well understood theoretically. We will tackle on the statistical properties of wide binary system in future. Actually, the candidate of wide binary has already been observed in our simulation. Using sink particle technique, we will do long term calculation to trace the evolution of this kind of wide binary system in future.

5.2.3 Application for Massive Star Formation

One of the most important study is to investigate the formation process of massive stars. Massive star plays important role in the evolution of interstellar medium and galaxy because massive stars scatter heavy elements. However, the relation between massive star formation and filamentary structure is not theoretically understood since theoretical previous works adopt the spherical symmetrical cloud as the initial condition (e.g., Krumholz et al., 2009). Recent observations show that the massive protostars are formed in hub structure which is a intersection of multiple filaments (Kumar et al., 2020), so the filament structure plays an essential role in not only the low mass star formation but also high mass star formation process. Therefore, we will extend our current research for low mass star formation process to high mass star formation process.

Appendix A

Derivation of Equations

A.1 Derivation of $\boldsymbol{R}(\boldsymbol{k}; L_{\rm core})$

In this appendix, we show the detailed derivation of the Fourier component of the position $\boldsymbol{R}(\boldsymbol{k}; L_{\rm core})$ of Equation 2.10. Using the Bessel Functions of the first kind $J_B^{(1)}$, $J_B^{(2)}$ and the spherical Bessel functions $j_B^{(0)}$, $j_B^{(1)}$, the x-component of $\boldsymbol{R}(\boldsymbol{k}; L_{\rm core})$ is

$$R_x(\boldsymbol{k}; L_{\rm core}) = -R_{\rm fil}\frac{k_x}{k_r}j_B^{(0)}(X)\frac{J_B^{(2)}(Y)}{Y}, \tag{A.1}$$

the y-component of $\boldsymbol{R}(\boldsymbol{k}; L_{\rm core})$ is

$$R_y(\boldsymbol{k}; L_{\rm core}) = -R_{\rm fil}\frac{k_y}{k_r}j_B^{(0)}(X)\frac{J_B^{(2)}(Y)}{Y}, \tag{A.2}$$

the z-component of $\boldsymbol{R}(\boldsymbol{k}; L_{\rm core})$ is

$$R_z(\boldsymbol{k}; L_{\rm core}) = -\frac{L_{\rm core}}{2}j_B^{(1)}(X)\frac{J_B^{(1)}(Y)}{Y}, \tag{A.3}$$

where $X \equiv k_z L_{\rm core}/2$, $Y \equiv k_r R_{\rm fil}$, and $k_r = \sqrt{k_x^2 + k_y^2}$. The k_x, k_y, and k_z are the wavenumber of x, y, and z directions, respectively. To derive these expressions, we have used the following equations (Abramowitz & Stegun, 1965):

$$\frac{d}{dx}[x^{-\nu}J_B^{(\nu)}(x)] = -x^{-\nu}J_B^{(\nu+1)}(x), \tag{A.4}$$

$$\frac{d}{dx}[x^{-\nu}j_B^{(\nu)}(x)] = -x^{-\nu}j_B^{(\nu+1)}(x), \tag{A.5}$$

$$j_B^{(0)}(X) = \frac{1}{L_{\rm core}}\int_{-L_{\rm core}/2}^{L_{\rm core}/2} dz\,\exp(\mathrm{ik_z z}), \tag{A.6}$$

$$J_B^{(0)}(Y) = \frac{1}{2\pi}\int_{-\pi}^{\pi} d\phi \exp(\mathrm{ik_r r}\cos\phi), \tag{A.7}$$

$$J_B^{(1)}(Y) = \frac{k_r}{R_{\mathrm{fil}}}\int_0^{R_{\mathrm{fil}}} J_B^{(0)}(k_r r) r dr, \tag{A.8}$$

where ν denotes the index of Bessel Function. In this paper we consider only integer values of ν.

A.2 Derivation of Equation 2.25

In the following we detail the derivation of Equation 2.26. Using Equation 4.4, Equation 2.24 can be written as,

$$\begin{aligned}\widetilde{\boldsymbol{v}}(k_z) &= \frac{1}{L_z}\int_{-L_z/2}^{L_z/2}\sum_{k_x'}\sum_{k_y'}\sum_{k_z'}\boldsymbol{V}(\boldsymbol{k}')\exp(\mathrm{i}\boldsymbol{k}'\cdot\boldsymbol{x})\exp(-\mathrm{ik_z z})\mathrm{dz}\\ &= \frac{1}{L_z}\sum_{k_x'}\sum_{k_y'}\sum_{k_z'}\boldsymbol{V}(\boldsymbol{k}')\exp(\mathrm{ik_x' x + ik_y' y})\\ &\quad\times\int_{-L_z/2}^{L_z/2}\exp(\mathrm{ik_z' z - ik_z z})\mathrm{dz},\end{aligned} \tag{A.9}$$

where $\widetilde{\boldsymbol{v}}(k_z)$ is the 1D Fourier component of the velocity field and $\boldsymbol{V}$ is the 3D Fourier component of the velocity field. Here, x and y are the cloud coordinates in the x-y plane perpendicular to the filament axis. Since we take the limit $R_{\mathrm{fil}} \to 0$, we do not take the integration in the x-y plane in this appendix (cf., Equation 2.23). Since $\int_{-L_z/2}^{L_z/2}\exp(\mathrm{i}k_z' z - \mathrm{i}k_z z)dz = L_z\delta_{k_z,k_z'}$, where $\delta_{k_z,k_z'}$ is the Kronecker delta, Equation A.9 can be rewritten as

$$\widetilde{\boldsymbol{v}}(k_z) = \sum_{k_x'}\sum_{k_y'}\sum_{k_z'}\boldsymbol{V}(\boldsymbol{k}')\exp(\mathrm{ik_x' x + ik_y' y})\delta_{\mathrm{k_z,k_z'}}. \tag{A.10}$$

Finally, $\widetilde{\boldsymbol{v}}$ can be written as,

$$\widetilde{\boldsymbol{v}}(k_z) = \sum_{k_x'}\sum_{k_y'}\boldsymbol{V}(k_x', k_y', k_z)\exp(\mathrm{ik_x' x + ik_y' y}). \tag{A.11}$$

Using Equation 2.3 and Equation A.11, we can derive Equation 2.26.

A.3 Derivation of Equation 4.11

In this appendix, we detail the derivation of Equation 4.11. We consider the turbulent velocity field

$$\boldsymbol{v}(\boldsymbol{x}) = \sum_{\boldsymbol{k}}\boldsymbol{V}(\boldsymbol{k})\sin(\boldsymbol{k}\cdot\boldsymbol{x} + \phi_{\boldsymbol{k}}), \tag{A.12}$$

where $\boldsymbol{V}(\boldsymbol{k})$ is the Fourier transform. Using Equation A.12, Equation 4.10 can be written as follows:

$$\boldsymbol{J} = \rho \sum_{\boldsymbol{k}} \int \boldsymbol{r} \times \boldsymbol{V}(\boldsymbol{k}) \sin(\boldsymbol{k} \cdot \boldsymbol{x} + \phi_{\boldsymbol{k}}) d^3x \tag{A.13}$$

$$= \rho \sum_{\boldsymbol{k}} \boldsymbol{V}(\boldsymbol{k}) \times \frac{\partial}{\partial \boldsymbol{k}} \int \cos(\boldsymbol{k} \cdot \boldsymbol{x} + \phi_{\boldsymbol{k}}) d^3x. \tag{A.14}$$

Using the addition theorem and change of variables $\boldsymbol{x'} = (a_1 x, a_2 y, a_3 z)$, Equation A.14 can be written as

$$\boldsymbol{J} = \rho a_1 a_2 a_3 \sum_{\boldsymbol{k}} \cos\phi_{\boldsymbol{k}} \boldsymbol{V}(\boldsymbol{k}) \times \frac{\partial}{\partial \boldsymbol{k}} \int \cos(\boldsymbol{k'} \cdot \boldsymbol{x'}) d^3x', \tag{A.15}$$

where $\boldsymbol{k'} = (k_x a_1, k_y a_2, k_z a_3)$. We can easily calculate the integration,

$$\boldsymbol{J} = 4\pi\rho a_1 a_2 a_3 \sum_{\boldsymbol{k}} \cos\phi_{\boldsymbol{k}} \boldsymbol{V}(\boldsymbol{k}) \times \frac{\partial}{\partial \boldsymbol{k}} \frac{\sin y - y\cos y}{y^3}, \tag{A.16}$$

where $y = |\boldsymbol{k'}|$. Then we can evaluate the derivative in Equation A.16,

$$\boldsymbol{J} = -12\pi\rho a_1 a_2 a_3 \sum_{\boldsymbol{k}} \cos\phi_{\boldsymbol{k}} \boldsymbol{V}(\boldsymbol{k}) \times \left(\frac{\sin y}{y^4} - \frac{\cos y}{y^3} - \frac{\sin y}{3y^2} \right) \frac{\partial k'}{\partial \boldsymbol{k}} \tag{A.17}$$

$$= -\frac{M}{5} \sum_{\boldsymbol{k}} \boldsymbol{V}(\boldsymbol{k}) \times \boldsymbol{k''} f(y) \cos\phi_{\boldsymbol{k}}. \tag{A.18}$$

This is the exactly same with Equation 4.11.

References

Abe D., Inoue T., Inutsuka S.-i., Matsumoto T., 2021, ApJ, 916, 83

Abramowitz M., Stegun I. A., 1965, Handbook of mathematical functions with formulas, graphs, and mathematical tables

André P., et al., 2010, A&A, 518, L102

André P., Di Francesco J., Ward-Thompson D., Inutsuka S.-I., Pudritz R. E., Pineda J. E., 2014, Protostars and Planets VI, pp 27–51

Armstrong J. W., Rickett B. J., Spangler S. R., 1995, ApJ, 443, 209

Arroyo-Chávez G., Vázquez-Semadeni E., 2021, arXiv e-prints, p. arXiv:2106.10381

Arzoumanian D., et al., 2011, A&A, 529, L6

Arzoumanian D., André P., Peretto N., Könyves V., 2013, A&A, 553, A119

Arzoumanian D., Shimajiri Y., Inutsuka S.-i., Inoue T., Tachihara K., 2018, PASJ, 70, 96

Arzoumanian D., et al., 2019, A&A, 621, A42

Barnes J., Hut P., 1986, Nature, 324, 446

Basu S., 1997, ApJ, 485, 240

Baug T., et al., 2020, ApJ, 890, 44

Belloche A., 2013a, in Hennebelle P., Charbonnel C., eds, EAS Publications Series Vol. 62, EAS Publications Series. pp 25–66

Belloche A., 2013b, in Hennebelle P., Charbonnel C., eds, EAS Publications Series Vol. 62, EAS Publications Series. pp 25–66

Benisty M., et al., 2017, A&A, 597, A42

Bodenheimer P., 1995, ARA&A, 33, 199

Braine J., Rosolowsky E., Gratier P., Corbelli E., Schuster K. F., 2018, A&A, 612, A51

Braine J., Hughes A., Rosolowsky E., Gratier P., Colombo D., Meidt S., Schinnerer E., 2020, A&A, 633, A17

Burkert A., Bodenheimer P., 2000, ApJ, 543, 822

Casassus S., et al., 2018, MNRAS, 477, 5104

Caselli P., Benson P. J., Myers P. C., Tafalla M., 2002, ApJ, 572, 238

Chandrasekhar S., 1961, Hydrodynamic and hydromagnetic stability

Chen C.-Y., Ostriker E. C., 2018, ApJ, 865, 34

Chen X., Launhardt R., Henning T., 2007, ApJ, 669, 1058

Chen X., et al., 2013, ApJ, 768, 110

Chen C.-Y., et al., 2019a, MNRAS, 490, 527

Chen C.-Y., et al., 2019b, MNRAS, 490, 527

Dhabal A., Mundy L. G., Rizzo M. J., Storm S., Teuben P., 2018, ApJ, 853, 169

Dib S., Hennebelle P., Pineda J. E., Csengeri T., Bontemps S., Audit E., Goodman A. A., 2010, ApJ, 723, 425

Doroshkevich A. G., 1970, Astrophysics, 6, 320

Dubinski J., Narayan R., Phillips T. G., 1995, ApJ, 448, 226

Duchêne G., Kraus A., 2013, ARA&A, 51, 269

Duquennoy A., Mayor M., 1991, A&A, 500, 337

Eswaraiah C., et al., 2021, ApJ, 912, L27

Feddersen J. R., et al., 2020, ApJ, 896, 11

Fernández-López M., et al., 2014, ApJ, 790, L19

Fleck R. C. J., Clark F. O., 1981, ApJ, 245, 898

Gaudel M., et al., 2020, A&A, 637, A92

Goldsmith P. F., Arquilla R., 1985, in Black D. C., Matthews M. S., eds, Protostars and Planets II. pp 137–149

Goodman A. A., Benson P. J., Fuller G. A., Myers P. C., 1993, ApJ, 406, 528

Hacar A., Tafalla M., 2011, A&A, 533, A34

Hacar A., Kainulainen J., Tafalla M., Beuther H., Alves J., 2016, A&A, 587, A97

Hacar A., Tafalla M., Forbrich J., Alves J., Meingast S., Grossschedl J., Teixeira P. S., 2018, A&A, 610, A77

Hanawa T., Nakayama K., 1997, ApJ, 484, 238

Hanawa T., Kudoh T., Tomisaka K., 2017, ApJ, 848, 2

Heiderman A., Evans II N. J., Allen L. E., Huard T., Heyer M., 2010, ApJ, 723, 1019

Hennebelle P., Teyssier R., 2008, A&A, 477, 25

Imara N., Blitz L., 2011, ApJ, 732, 78

Imara N., Bigiel F., Blitz L., 2011, ApJ, 732, 79

Inoue T., Fukui Y., 2013, ApJ, 774, L31

Inoue T., Inutsuka S.-i., 2008, ApJ, 687, 303

Inoue T., Inutsuka S.-i., 2009, ApJ, 704, 161

Inoue T., Inutsuka S.-i., 2012, ApJ, 759, 35

Inoue T., Hennebelle P., Fukui Y., Matsumoto T., Iwasaki K., Inutsuka S.-i., 2018, PASJ, 70, S53

Inutsuka S.-i., 2001, ApJ, 559, L149

Inutsuka S.-i., 2002, Journal of Computational Physics, 179, 238

Inutsuka S.-I., Miyama S. M., 1992, ApJ, 388, 392

Inutsuka S.-i., Miyama S. M., 1997, ApJ, 480, 681

Inutsuka S.-i., Inoue T., Iwasaki K., Hosokawa T., 2015, A&A, 580, A49

Iwasaki K., Inutsuka S.-I., 2011, MNRAS, 418, 1668

Iwasaki K., Inutsuka S. I., 2013, in Pogorelov N. V., Audit E., Zank G. P., eds, Astronomical Society of the Pacific Conference Series Vol. 474, Numerical Modeling of Space Plasma Flows (ASTRONUM2012). p. 239

Iwasawa M., Tanikawa A., Hosono N., Nitadori K., Muranushi T., Makino J., 2016, PASJ, 68, 54

Koch E. W., Rosolowsky E. W., 2015, MNRAS, 452, 3435

Kong S., Arce H. G., Maureira M. J., Caselli P., Tan J. C., Fontani F., 2019, ApJ, 874, 104

Könyves V., et al., 2015, A&A, 584, A91

Krumholz M. R., Klein R. I., McKee C. F., Offner S. S. R., Cunningham A. J., 2009, Science, 323, 754

Kuffmeier M., Calcutt H., Kristensen L. E., 2019, A&A, 628, A112

Kumar M. S. N., Palmeirim P., Arzoumanian D., Inutsuka S. I., 2020, A&A, 642, A87

Kuznetsova A., Hartmann L., Heitsch F., 2019, ApJ, 876, 33

Kuznetsova A., Hartmann L., Heitsch F., 2020, ApJ, 893, 73

Lada C. J., Lombardi M., Alves J. F., 2010, ApJ, 724, 687

Lada C. J., Forbrich J., Lombardi M., Alves J. F., 2012, ApJ, 745, 190

Larson R. B., 1969, MNRAS, 145, 271

Larson R. B., 1981, MNRAS, 194, 809

Lee Y.-N., Hennebelle P., Chabrier G., 2017, ApJ, 847, 114

Lee A. T., Offner S. S. R., Kratter K. M., Smullen R. A., Li P. S., 2019, ApJ, 887, 232

Li P. S., Klein R. I., McKee C. F., 2018, MNRAS, 473, 4220

Loomis R. A., Öberg K. I., Andrews S. M., MacGregor M. A., 2017, ApJ, 840, 23

Looney L. W., Mundy L. G., Welch W. J., 2000, ApJ, 529, 477

Machida M. N., Matsumoto T., Hanawa T., Tomisaka K., 2005, MNRAS, 362, 382

Machida M. N., Inutsuka S.-i., Matsumoto T., 2007, ApJ, 670, 1198

Machida M. N., Tomisaka K., Matsumoto T., Inutsuka S.-i., 2008, ApJ, 677, 327

Machida M. N., Hirano S., Kitta H., 2020, MNRAS, 491, 2180

Marino S., Perez S., Casassus S., 2015, ApJ, 798, L44

Masunaga H., Inutsuka S.-i., 2000, ApJ, 531, 350

Matsumoto T., 2007, PASJ, 59, 905

Matsumoto T., Hanawa T., 2003, ApJ, 595, 913

Matsumoto T., Hanawa T., 2011, ApJ, 728, 47

Matsumoto T., Nakamura F., Hanawa T., 1994, PASJ, 46, 243

Matsumoto T., Hanawa T., Nakamura F., 1997, ApJ, 478, 569

Matsumoto T., Machida M. N., Inutsuka S.-i., 2017, ApJ, 839, 69

Mayama S., et al., 2018, ApJ, 868, L3

Misugi Y., Inutsuka S.-i., Arzoumanian D., 2019, ApJ, 881, 11

Miville-Deschênes M.-A., et al., 2010, A&A, 518, L104

Moe M., Di Stefano R., 2017, ApJS, 230, 15

Moe M., Kratter K. M., Badenes C., 2019, ApJ, 875, 61

Muro-Arena G. A., et al., 2020, A&A, 635, A121

Nagasawa M., 1987, Progress of Theoretical Physics, 77, 635

Ntormousi E., Hennebelle P., 2019, A&A, 625, A82

Offner S. S. R., Klein R. I., McKee C. F., 2008, ApJ, 686, 1174

Offner S. S. R., Kratter K. M., Matzner C. D., Krumholz M. R., Klein R. I., 2010, ApJ, 725, 1485

Offner S. S. R., Dunham M. M., Lee K. I., Arce H. G., Fielding D. B., 2016, ApJ, 827, L11

Okoda Y., et al., 2021, ApJ, 910, 11

Ostriker J., 1964, ApJ, 140, 1056

Palmeirim P., et al., 2013, A&A, 550, A38

Peebles P. J. E., 1969, ApJ, 155, 393

Penston M. V., 1969, MNRAS, 144, 425

Pineda J. E., Zhao B., Schmiedeke A., Segura-Cox D. M., Caselli P., Myers P. C., Tobin J. J., Dunham M., 2019, ApJ, 882, 103

Pirogov L., Zinchenko I., Caselli P., Johansson L. E. B., Myers P. C., 2003, A&A, 405, 639

Press W. H., Schechter P., 1974, ApJ, 187, 425

Price D. J., Bate M. R., 2007, MNRAS, 377, 77

Punanova A., Caselli P., Pineda J. E., Pon A., Tafalla M., Hacar A., Bizzocchi L., 2018, A&A, 617, A27

Raghavan D., et al., 2010, ApJS, 190, 1

Roy A., et al., 2015, A&A, 584, A111

Roy A., et al., 2019, A&A, 626, A76

Saigo K., Hanawa T., 1998, ApJ, 493, 342

Sakai N., Hanawa T., Zhang Y., Higuchi A. E., Ohashi S., Oya Y., Yamamoto S., 2019, Nature, 565, 206

Sana H., et al., 2012, Science, 337, 444

Sana H., et al., 2014, ApJS, 215, 15

Sousbie T., 2011, MNRAS, 414, 350

Spitzer L., 1978, Physical processes in the interstellar medium

Stephens I. W., et al., 2017, ApJ, 846, 16

Stodólkiewicz J. S., 1963, Acta Astron., 13, 30

Stolker T., et al., 2017, ApJ, 849, 143

Sugitani K., et al., 2011, ApJ, 734, 63

Tafalla M., Hacar A., 2015, A&A, 574, A104

Takahashi S. Z., Tomida K., Machida M. N., Inutsuka S.-i., 2016, MNRAS, 463, 1390

Takaishi D., Tsukamoto Y., Suto Y., 2021, PASJ,

Tatematsu K., Ohashi S., Sanhueza P., Nguyen Luong Q., Umemoto T., Mizuno N., 2016, PASJ, 68, 24

Tobin J. J., et al., 2011, ApJ, 740, 45

Tobin J. J., et al., 2016, ApJ, 818, 73

Tomisaka K., 2000, ApJ, 528, L41

Torii K., et al., 2019, PASJ,

Tsukamoto Y., Iwasaki K., Inutsuka S.-i., 2013, MNRAS, 434, 2593

White S. D. M., 1984, ApJ, 286, 38

Winn J. N., Fabrycky D. C., 2015, ARA&A, 53, 409

Zhang S., Hartmann L., Zamora-Avilés M., Kuznetsova A., 2018, MNRAS, 480, 5495